

# Nonlinear Dynamical Systems

Student papers for  
Math 164: Scientific Computing  
Spring 2013

edited by

**Jeffrey R. Chasnov**



Harvey Mudd College  
Department of Mathematics  
301 Platt Boulevard  
Claremont, CA 91711



Copyright © 2013 by Jeffrey Robert Chasnov

This work is licensed under the Creative Commons Attribution 3.0 unported License. To view a copy of this license, visit <http://creativecommons.org/licenses/by/3.0/hk/> or send a letter to Creative Commons, 171 Second Street, Suite 300, San Francisco, California, 94105, USA.

## Assignment Instructions

Paper #1, done individually, should present a numerical study of some limited aspects of a dynamical system. Each student will be required to study his or her own equations (with no duplication among students). Problems can be taken from the compilation of equations posted on the course website, or some other equations upon approval of the instructor. The various tools discussed in lecture may be applied to the problem chosen, including phase space diagrams, basins of attraction, Poincare sections, bifurcation diagrams and the computation of fractal dimensions. I will give students the freedom to research whatever they find interesting provided that scientific computation forms the basis of their paper. You should research ideas for papers on the internet or in the library, and papers should properly reference the web sites, papers and books used.

Assessment will be made on a research paper of no more than eight pages written in LaTeX. I have posted a rubric that will be used in the grading. The paper should contain an informative title, author name and short abstract. The main section headings should include the following: Introduction, Governing equations, Results, Discussion. Students are free to label subsections as desired. The paper must contain a Bibliography, and may contain an Acknowledgments.

Submission of this paper will be in the form of a LaTeX file and associated pdf file. Any nonstandard .sty files, etc. used by LaTeX will also need to be submitted because I plan to post on the course website a pdf file containing a collection of all the student papers.

# Contents

<b>Chaos and Critical Points of the Lorenz Equations</b>	<b>4</b>
<i>Stephanie Porter</i>	
<b>Testing Approximations in the Limit Cycles of the Van der Pol Oscillator</b>	<b>11</b>
<i>Elizabeth Schofield</i>	
<b>Flip-Over Threshold for the Double Pendulum</b>	<b>16</b>
<i>Julius Elinson</i>	
<b>Dynamics of a Forced Duffing's Oscillator</b>	<b>24</b>
<i>Kyle Siegel</i>	
<b>Degree m Polynomial Fractal Sets</b>	<b>32</b>
<i>Ben Corr</i>	
<b>Chaotic Behaviors of Chua's Circuit</b>	<b>40</b>
<i>Tianyou Gu</i>	
<b>Investigating the Henon Map</b>	<b>48</b>
<i>Shreyas Kumar</i>	
<b>Quadratic Julia Sets and the Mandelbrot Set</b>	<b>56</b>
<i>Jason Wang</i>	
<b>Rendering L-Systems via Chaos Games</b>	<b>63</b>
<i>John Wentworth</i>	
<b>Investigation of the Ikeda map</b>	<b>70</b>
<i>Michael Fox</i>	
<b>Chaotic Dynamics of the Standard Map</b>	<b>75</b>
<i>Mitul Verma</i>	
<b>Dimensions of Classical Fractals</b>	<b>82</b>
<i>Neil Pearson</i>	
<b>On the Stable Dynamics of the Free Brusselator Equations</b>	<b>91</b>
<i>Matt Hin</i>	

# Chaos and Critical Points of the Lorenz Equations

*Stephanie Porter*

## Abstract

The Lorenz equations are a set of deterministic, three-dimensional, coupled, nonlinear equations that make up a deterministic system. Originally intended to describe atmospheric conditions and their chaotic behavior, the equations have proved to have applications in multiple fields. Three critical points are identified, as defined by the system's parameter values, and their stabilities are determined. Each of these critical points have physical significance in their respective applications. Additionally, the Lorenz attractor, which demonstrates the chaotic behavior of the system, is explored in depth.

## 1 Introduction

Developed in 1963 by Edward Lorenz as a simplified mathematical model for atmospheric convection, the Lorenz equations are a set of three-dimensional, coupled, nonlinear equations that comprise a deterministic system. They were originally derived as an approximation of certain equations characterizing the flow of shallow liquid subject to universal cooling and heating from above and below, respectively. In addition to atmospheric applications, the Lorenz equations also appear in applications ranging from chemical reactions to lasers [1]-[3].

Given particular parameter values, the Lorenz equations are also known to produce chaotic solutions. Here, chaos is used to define a system in which minor adjustments in initial conditions produce large variations in results, or what is commonly known as the “butterfly effect” [4]. These chaotic solutions make up the Lorenz attractor. A particle with initial conditions within the attractor will move within its orbit; however, the actual motion of the particle appears to be random. Therefore, while the Lorenz system is deterministic, it is not predictable.

This paper examines the critical points of the Lorenz system and their relative stabilities. Critical points in the Lorenz system have significance dependent on their application. For example, in the chemical reaction applications, critical points relate to conditions in which no phase boundaries exist [3]. For thorough analysis in these applications, it is important to know the exact conditions that determine these critical points. We will also investigate for what values the Lorenz equations generate the Lorenz attractor, and how dramatically the system responds to slight variations in these parameter values. This will serve to characterize the chaotic nature of the Lorenz equations.

## 2 Governing Equations

The Lorenz equations are given by

$$\dot{X} = \sigma(Y - X), \tag{1}$$

$$\dot{Y} = X(R - Z) - Y, \tag{2}$$

$$\dot{Z} = XY - bZ, \tag{3}$$

where  $X, Y$ , and  $Z$  are the state variables that define the three-dimensional phase space. The constants  $\sigma, R$ , and  $b$  are the system parameters, and are generally set to be positive. In the Lorenz

equations,  $\sigma$  represents the Prandtl number, or the ratio of momentum diffusivity to thermal diffusivity,  $R$  represents the ratio of the Rayleigh number to the critical Rayleigh number, and  $b$  represents a geometric factor. Both  $\sigma$  and  $b$  relate to the dissipation of the system [5]. All derivatives are taken with respect to time.

## 2.1 Critical Points

To calculate the critical points of the system, we set all the derivatives to 0. Then from Equation 1 we find that

$$0 = \sigma(Y - X).$$

From this we can conclude that  $X = Y$ , since  $\sigma$  is a constant. When  $X = Y = 0$ , we see that  $Z = 0$  by substitution into Equation 3, since  $b$  is also a constant. When  $X = Y \neq 0$ , we have

$$X = X(R - Z),$$

again by substitution. Since  $X \neq 0$ , we can divide through by  $X$  to find  $Z = R - 1$ . Plugging this into Equation 3 gives

$$X^2 = bZ = b(R - 1),$$

so  $X = \pm\sqrt{b(R - 1)}$ . The term within the square root must be positive for  $X$  to be a real number. Since values of  $b$  are generally taken to be positive, this forces  $R - 1 > 0$ , or  $R > 1$ . Therefore, we find one critical point at the origin for  $R < 1$ , and two critical points for  $R > 1$  at

$$\left(\sqrt{b(R - 1)}, \sqrt{b(R - 1)}, R - 1\right) \quad \text{and} \quad \left(-\sqrt{b(R - 1)}, -\sqrt{b(R - 1)}, R - 1\right),$$

respectively.

Critical points are stable when all eigenvalues have negative, real values. For the origin, our Jacobian matrix is given by

$$J = \begin{pmatrix} -\sigma & \sigma & 0 \\ R & -1 & 0 \\ 0 & 0 & -b \end{pmatrix}.$$

Then the eigenvalues correspond to the values of  $\lambda$  such that

$$(J - I\lambda) = \begin{vmatrix} -\sigma - \lambda & \sigma & 0 \\ R & -1 - \lambda & 0 \\ 0 & 0 & -b - \lambda \end{vmatrix} = 0.$$

This reduces to

$$[(-\sigma - \lambda)(-1 - \lambda) - \sigma R](-b - \lambda) = 0.$$

Then either  $\lambda = -b$  or  $(-\sigma - \lambda)(-1 - \lambda) - \sigma R = 0$ , which becomes

$$(-\sigma - \lambda)(-1 - \lambda) = \lambda^2 + \lambda(1 + \sigma) + \sigma(1 - R) = 0.$$

By the quadratic formula,

$$\lambda_{\pm} = \frac{-(1 + \sigma) \pm \sqrt{1 - (2 + 4R)\sigma + \sigma^2}}{2}.$$

For  $R < 1$ , the term inside the square root is less than  $(\sigma - 1)^2$ , which makes both  $\lambda$  terms less than 0. Therefore, as these values are both negative and real, the origin is a stable fixed point.

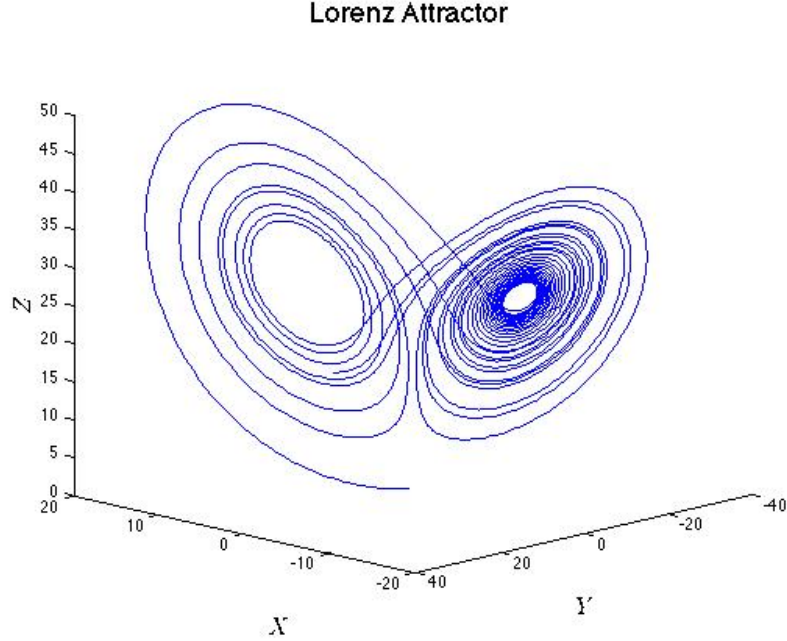


Figure 1: The Lorenz attractor. The Lorenz equations demonstrate chaotic behavior for parameter values  $\sigma = 10$ ,  $R = 28$ , and  $b = 8/3$ . The axes represent values of the state variables.

Additionally, as the origin sets all state variables to 0, the choice of parameter values has no effect on the system response. Therefore, the origin is a universal stable point, since it is stable for all possible parameter values.

Similarly, the other two critical points are stable when

$$\lambda^3 + (\sigma + b + 1)\lambda^2 + (R + \sigma)b\lambda + 2b\sigma(R - 1) = 0.$$

Then the two critical points are stable for

$$1 < R < \frac{\sigma(\sigma + b + 3)}{\sigma - b - 1}.$$

Note that this only holds for positive values of  $R$  when  $\sigma > b + 1$ .

## 2.2 Lyapunov Exponents

Chaotic systems are defined by how quickly close initial conditions diverge from one another. One way to characterize this rate of separation is through the Lyapunov exponents. Assume we have two initial conditions, given by

$$i = (x_1, y_1, z_1) \text{ and } j = (x_2, y_2, z_2).$$

Then their difference, with respect to time, is given by

$$d(t) = \sqrt{(x_1 - x_2)^2 + (y_1 - y_2)^2 + (z_1 - z_2)^2}.$$

For extremely small  $t$ , we can approximate this to  $d_0 e^{\lambda t}$ . In this case,  $\lambda$  is the Lyapunov exponent. Positive exponents correspond to chaotic behavior, and the larger the exponent, the larger the rate

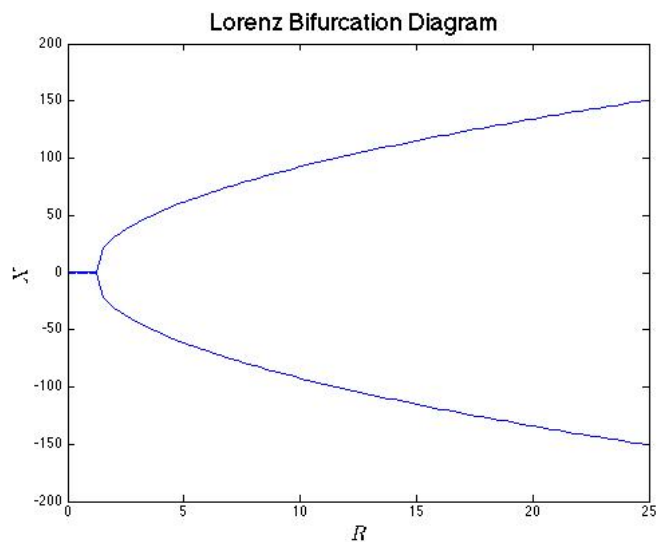


Figure 2: Bifurcation diagram of the Lorenz equations. With  $\sigma =$  and  $b =$ , we plot the steady value of  $X$  as a function of  $R$ .  $X$  represents the state variable. A pitchfork bifurcation occurs at  $R = 1$ , when the system moves from one critical point to two. Image source: <http://www.atm.ox.ac.uk/user/read/chaos/lect6.pdf>.

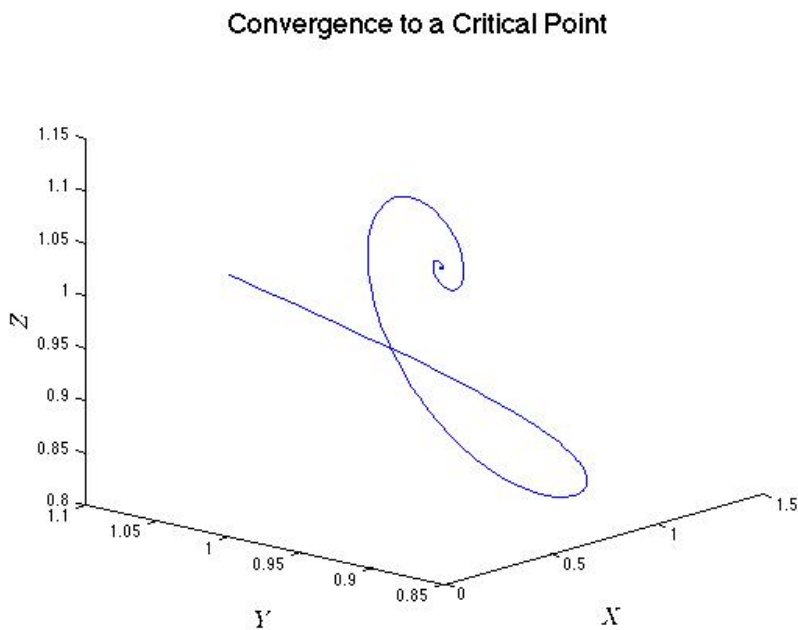


Figure 3: Solutions to the Lorenz equation for values  $\sigma = 5, R = 2$ , and  $b = 1$ . The solution converges to the critical point  $(1, 1, 1)$ , demonstrating that it is stable for these parameter values. The axes represent the state variables of the system.

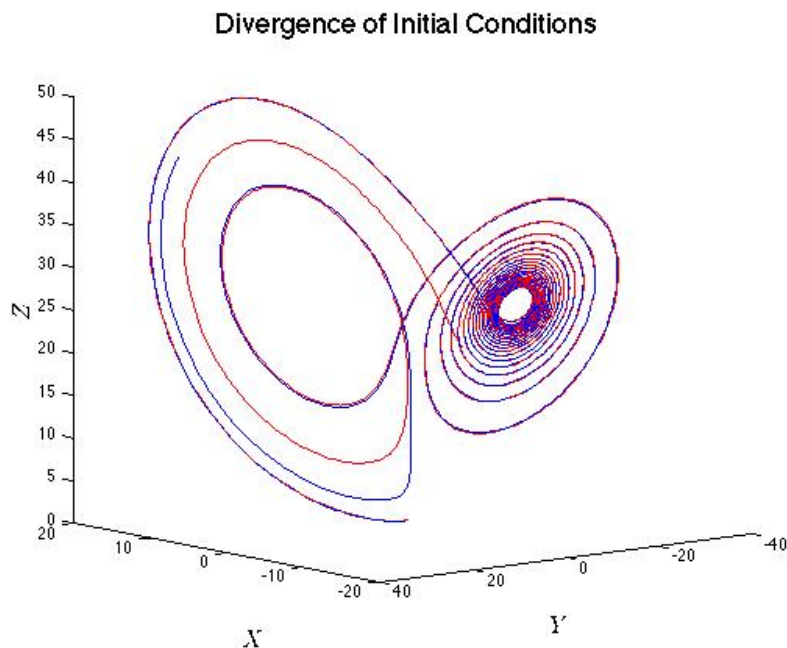


Figure 4: Two plots of the Lorenz equations given parameter values for the Lorenz attractor. Initial conditions were set to  $(0, 1, 1.05)$  for the red line, and  $(.1, 1.1, 1)$  for the blue line. Solutions were generated for  $t = 0$  to 16. The system demonstrates a large divergence for similar initial conditions, but only after a given amount of time.

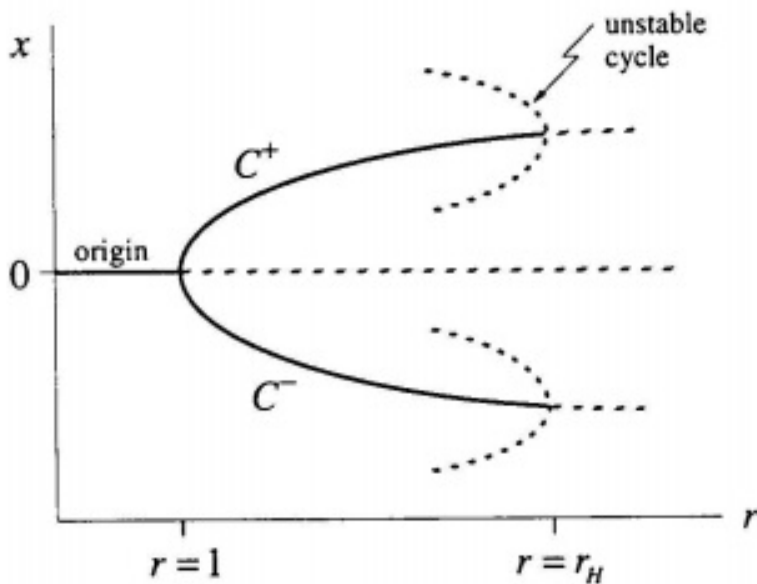


Figure 5: A bifurcation diagram of the Lorenz equations. Here,  $r = R$  and  $r_H = \frac{\sigma(\sigma+b+3)}{\sigma-b-1}$ . We can see Hopf bifurcations occurring at  $r_H$ , where the stable critical points become unstable.

of divergence for similar initial conditions [7]. Therefore, the larger the Lyapunov exponents for the Lorenz system, the greater divergence in solutions. Here, the Lyapunov exponents are dependent on both the parameter values and the initial state variable values chosen, and are very difficult to calculate. Numerical calculations using MATLAB and parameter values for the Lorenz attractor in Section 3 show graphically how solutions to the Lorenz equations diverge.

### 3 Results

We have calculated the critical points and their stabilities by mathematical analysis. To confirm these theoretical conclusions, it is necessary to calculate the values numerically. Using MATLAB code, we can generate a bifurcation diagram, as seen in Figure 2, which demonstrates a pitchfork bifurcation at  $R = 1$ . Additionally, multiple tests were conducted with varying parameter values to demonstrate the convergence of the system to both critical points with values of  $R > 1$ . An example of this convergence can be seen in Figure 3.

As Lorenz first discovered, for values of  $\sigma = 10$ ,  $R = 28$ , and  $b = \frac{8}{3}$ , the Lorenz equations demonstrate chaotic behavior, forming the Lorenz attractor (Figure 1). Because of the chaotic nature associated with these values, initial conditions that are similar in magnitude display different solutions as time passes. Numerical calculations were performed to demonstrate the divergence of solutions given different but similar initial conditions for the Lorenz attractor. As seen in Figure 4, two initial conditions given by  $(0,1,1.05)$  and  $(2,2,2)$  have solutions that diverge from one another, despite being relatively comparable at the start. The red line continues to converge on itself in a spiral, while the blue line starts to spiral out and demonstrate solutions much farther from the concentration solutions of the red line.

### 4 Discussion

Through mathematical analysis, we determined that one stable fixed point exists for the Lorenz system at the origin. This critical point exists until  $R > 1$ , when we witness a split into two critical points at

$$\left(\sqrt{b(R-1)}, \sqrt{b(R-1)}, R-1\right) \quad \text{and} \quad \left(-\sqrt{b(R-1)}, -\sqrt{b(R-1)}, R-1\right).$$

This analysis based on theory is supported numerically by the bifurcation diagram in Figure 2, which demonstrates a pitchfork bifurcation at around  $R = 1$ . After examining the exact numerical values generated by the MATLAB code however, it was evident that this split occurred closer to  $R = 1.1$  than  $R = 1.0$ . This may be the product of a variety of factors, including roundoff errors, insufficient tolerance values, or general bugs in the MATLAB code.

Convergence to the other two critical points of the system was further tested with parameter values between 1 and  $\frac{\sigma(\sigma+b+3)}{\sigma-b-1}$ . The plots of the solutions to the Lorenz equations demonstrated a clear convergence to the points

$$\left(\sqrt{b(R-1)}, \sqrt{b(R-1)}, R-1\right) \quad \text{and} \quad \left(-\sqrt{b(R-1)}, -\sqrt{b(R-1)}, R-1\right).$$

In Figure 3 for example, parameter values were set to

$$\sigma = 5, b = 1, \text{ and } R = 2 < \frac{\sigma(\sigma+b+3)}{\sigma-b-1} = 15.$$

In theory, solutions for these should converge to either (1,1,1) or (-1,-1,1). From the figure, we can see that the solutions do converge to (1,1,1), relating to the first of the two calculated critical points, and demonstrates its property of attractive stability.

While other complications limited the range of the bifurcation diagram generated for this paper, research on the topic has provided images of the bifurcation diagram which demonstrates how the system responds to values of  $R > \frac{\sigma(\sigma+b+3)}{\sigma-b-1}$  [6]. These Hopf bifurcations can be seen in Figure 5, where  $r = R$  and  $C_+$  and  $C_-$  represent the critical points that occur for  $R > 1$ . The Hopf bifurcations occur at  $R = r_H = \frac{\sigma(\sigma+b+3)}{\sigma-b-1}$ .

In addition to the critical points, data was obtained regarding the chaotic response of the Lorenz system to initial conditions that varied by a minimal degree. As seen in Figure 4, these initial conditions eventually resulted in different solutions as dictated by the behavior of the Lorenz attractor. Interestingly, these solutions remained relatively close for a longer span of time than expected. Both solutions followed a similar (albeit separate, due to the slight displacement of their initial conditions) trajectory. Only at the point when both solutions began to follow the spiral did one solution begin to noticeably diverge from the other, tending toward more positive values of  $Y$  before looping back. This demonstrates chaotic behavior that is less divergent than was originally assumed, although still significantly present.

## References

- [1] P. Mandel and T. Erneux. Laser Lorenz Equations with a Time-Dependent Parameter. *The American Physical Society*. Nov 1984. Vol 53, pp. 1818-1820.
- [2] M. Moroz. Template analysis of a Faraday disk dynamo. *EPJ Special Top.* 165 211 220
- [3] D. Poland. Cooperative catalysis and chemical chaos: a chemical model for the Lorenz equations, *Physica D: Nonlinear Phenomena*. Vol. 65, May 1993, pp. 86-99
- [4] E. Lorenz. Predicability: Does the Flap of a Butterfly's Wings in Brazil Set Off a Tornado in Texas? *American Association for the Advancement of Science, 13th Meeting*. Dec 1972.
- [5] Lorenz Attractor. *Wolfram Mathworld*. <http://mathworld.wolfram.com/LorenzAttractor.html>
- [6] Three-Dimensional Systems: The Lorenz Equations. <http://www.atm.ox.ac.uk/user/read/chaos/lect6.pdf>
- [7] Lyapunov Exponents. [http://www.cmp.caltech.edu/~mcc/Chaos\\_Course/Lesson7/Lyapunov.pdf](http://www.cmp.caltech.edu/~mcc/Chaos_Course/Lesson7/Lyapunov.pdf)
- [8] Y. Li, W. Tang, and G. Chen. Generating Hyperchaos via a Simple Periodic Forcing Signal. *Proceedings of the 26th Chinese Control Conference*. July 2007. pp. 380-384.

# Testing Approximations in the Limit Cycles of the Van der Pol Oscillator

*Elizabeth Schofield*

## Abstract

This paper tests the fourth-order approximations provided by Edward Fisher (1954) for the amplitude and period of the stable limit cycles of the unforced van der Pol equation. By computing the approximated value of the period and comparing it to a numerically computed value for varying values of the parameter  $\nu$ , one can observe the divergence of the numerical from the theoretical result that occurs when the parameter is significantly greater than 1. In particular, the accuracy of the approximation falls below 99% for  $\nu > 1.3$  and below 95% for  $\nu > 2.0$ .

## 1 Introduction

The van der Pol equation, named for telecommunications pioneer Balthazar Van der Pol (1889-1959), is a second-order nonlinear differential equation most commonly examined in the field of nonlinear oscillations [1]. The equation models the oscillating charge of the van der Pol oscillator, a simple circuit with a parallel capacitor, charge source, and inductor in series with a tunnel diode or triode. The triode, typically a vacuum tube containing a cathode, grid, and anode, is used for electronic amplification, a key development in radio and telephone technology.

The key feature of the van der Pol oscillator is that its damping may be positive or negative in relation to the current amplitude of the oscillations. Specifically, larger oscillations are positively damped to become smaller, while smaller oscillations are negatively damped to become larger, all tending toward the same range of dynamic behavior. In fact, all forms of the unforced van der Pol oscillator tend toward a single stable limit cycle for their oscillations. For the purposes of telecommunications, circuits providing this functionality are useful in their ability to make both loud and quiet signals more easily perceived by the recipient. The only other equilibrium reached by the van der Pol equation is the unstable fixed point with zero amplitude and zero velocity, since a circuit containing no charge or charge source will see no oscillation; however, even the slightest bump of the circuit will eventually create a signal following the expected limit cycle [3].

In a 1953 paper titled "The Period and Amplitude of the Van Der Pol Limit Cycle," Edward Fisher of the General Precision Laboratory proposed analytical approximations of the limit cycle of the unforced Van der Pol equation [2]. Using the Lindstedt method—a method of using power series to approximate solutions to nonlinear differential equations—Fisher developed fourth-order linear approximations for the limit cycle's amplitude and period based upon the parameter  $\nu$  used to define a particular unforced van der Pol oscillator. The aim of this paper is to numerically confirm this analytical result for the period of the limit cycle, and to test the accuracy of this analytical result.

## 2 Governing Equations

The single unforced van der Pol equation is most traditionally written in the form

$$\ddot{x} + \nu(x^2 - 1)\dot{x} + x = 0$$

where the parameter  $\nu$  represents the magnitude of damping. One can observe that when  $\nu = 0$  the van der Pol equation becomes the simple harmonic oscillator equation.

The van der Pol equation is often rewritten as a pair of first-order differential equations:

$$\dot{x} = y$$

and

$$\dot{y} = \nu(1 - x^2)y - x.$$

This two-dimensional form allows us to better visualize the patterns of the limit cycles as they depend on  $\nu$ . Behavior of the equation, or more specifically its limit cycle, may most easily be divided into the cases  $\nu < 1$ ,  $\nu = 1$ , and  $\nu > 1$ . Though all cases result in a stable limit cycle and an unstable fixed point at  $x = y = 0$ , the specific form the limit cycles take varies greatly with the parameter  $\nu$ .

### 3 Approximation of the Period

As mentioned before, Fisher provides fourth-order approximations for the period and amplitude of the limit cycles in relation to the parameter  $\nu$  via the Lindstedt method [4]. To follow his derivation, we rely on the assumption that both  $x$  and the period  $T$  are power series. Specifically,  $x$  is assumed to take the form

$$x(t) = \cos t \sum_{k=0}^{\infty} a_k \mu^{2k} + \mu \sin^3 t \sum_{k=0}^{\infty} b_k \mu^{2k}$$

where  $a_k$  and  $b_k$  are polynomials of degree  $2k$  in  $\sin^2 t$ . Given this power series for  $x$  and the form of the one-dimensional van der Pol equation, we conclude that  $T$  must be a power series with respect to  $\nu^2$ . Fisher observes that “even with this simplification, however, the method is too laborious to carry far enough for our present purpose,” so we seek additional simplifications.

We substitute  $x = Au$ , where  $A$  is the amplitude of the limit cycle, and perform a change of variables:

$$\dot{u} = \dot{u}(u),$$

$$E = \left(\frac{1}{4}\right)[\dot{u}(u) + \dot{u}(-u)]^2$$

and

$$z = 1 - x^2.$$

In this case,  $\sqrt{E}$  represents the even part of  $\dot{u}$  with respect to  $u$ . These variables allow us to compute the power series for the period by integrating:

$$(\nu/2x)(A^2u^2 - 1)\sqrt{E} = \frac{d}{dz}9E\left(1 - \frac{dz}{dE}\right)^4$$

and

$$T = 8 \int_0^1 \frac{d\sqrt{E}}{dz} du.$$

We will use this formula to compute our approximation. We assume that  $E$  is a power series in  $\nu$  of the form

$$E = f_0(z) + \nu^2 f_1(z) + \nu^4 f_2(z).$$

Fisher substitutes the series

$$\dot{u}(u) = \sum_{k=0}^{\infty} \nu^k g_k(x)$$

to evaluate the value of the  $f$ 's. The outcome is a recurrence relation with  $g_{2k} = \sqrt{1-x^2}$ . We then obtain

$$f_0 = z, \quad f_1'(z) = c_1 z(1-z),$$

and

$$f_2'(z) = (c_2 z + c_3 z^2 + c_4 z^3)(1-z), \quad f_1(0) = f_2(0) = 0$$

with constant-valued  $c$ 's. We can then compute the values for the  $c_n$ 's:

$$c_1 = 1, \quad c_2 = \frac{1}{36}, \quad c_3 = \frac{11}{36}, \quad c_4 = -\frac{1}{2}.$$

Finally, substituting these values and series into our formula for  $T$  and integrating the first few terms, we obtain our approximation:

$$T = 2\pi + \pi\nu^2/8 - (5\pi/1536)\nu^4 \dots$$

By this method, we have created an approximation of the period  $T$  of the stable limit cycle that depends exclusively on  $\nu$  [2].

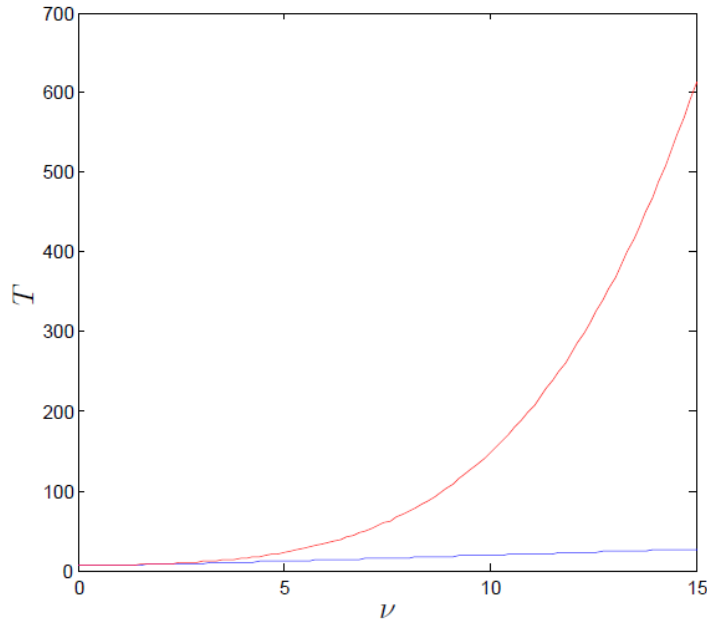


Figure 1: A plot of the approximated (red) vs. numerically computed (blue) length of the period of the limit cycle with respect to  $\nu$ . We see wide divergence at larger values of  $\nu$  and thus will focus on the range from 0 to 2.25.

## 4 Results

In order to evaluate the efficacy of our approximation of  $T$ , we use numerical methods to compute the period. Specifically, we compute solutions to the unforced van der Pol equation for a given

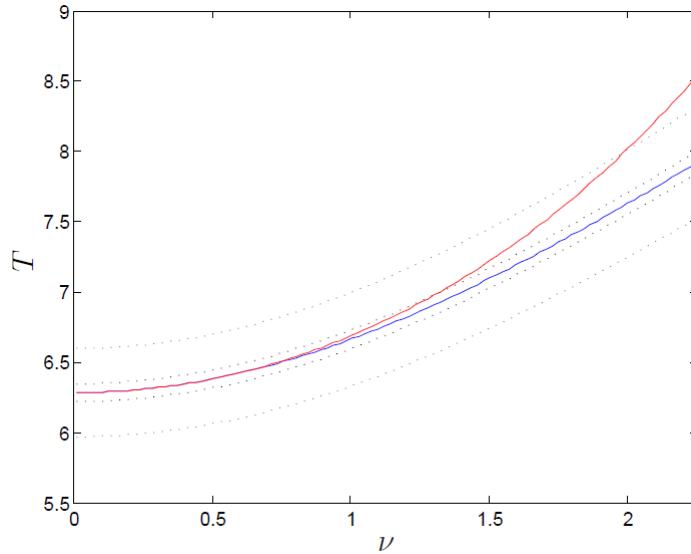


Figure 2: A plot of the approximated (red) vs. numerically computed (blue) length of the period of the limit cycle with respect to  $\nu$ . We see that these errors are both exceeded for all  $\nu > 2$ , but the approximation remains fairly accurate for values of  $\nu < 1$ .

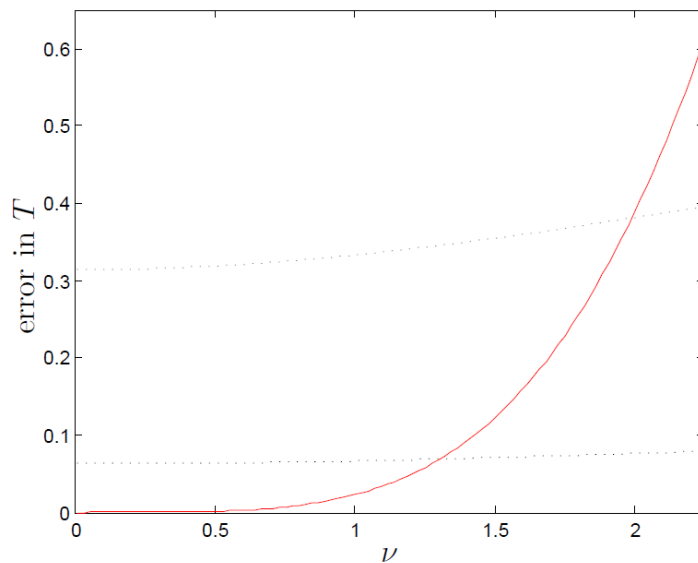


Figure 3: A plot of the error between the approximated and numerically computed length of the period of the limit cycle with respect to  $\nu$ . The black dashed line shows the range of 1% error about the computed period, which is crossed at approximately  $\nu = 1.3$ . The gray dashed line shows the range of 5% error, which is exceeded at approximately  $\nu = 2.0$ .

$\nu$  using MATLAB's stiff ODE differential equation solver `ode15s.m`, a variable-order method that uses a collection of numerical differentiation formulas. Then, using the `event` functionality, we can determine at what time  $t$  the system has converged to a limit cycle within marginal error, and then use root finding to compute the period of a full cycle from that point.

Once we have computed these numerical values of  $T$  for a sufficient range of values of  $\nu$ , the results may be compared to those of the approximation. The error of the numerical computation will be vastly smaller than that of the approximation in most cases, so we use the numerical method as a baseline for our comparison and evaluate the relative error of the approximated values of  $T$  (see Figure 1). We can quickly see that divergence of these two methods of computation occurs dramatically for  $\nu > 2$ , so we can focus specifically on the behavior of the approximation within this range.

In evaluating the error more specifically, we seek the maximum values of  $\nu$  for which the Fisher approximation is relatively accurate to the numerical computation. We will check two different values of accuracy, based upon percentage difference from the numerical value. For our purposes, within 1% error denotes a fairly accurate computation, and a difference of 5% or more suggests large inaccuracy. We can see this variation in a smaller range of  $\nu$ , with percentage error boundaries visible, in Figure 2. The divergence is more apparent in a plot of the difference between the two computations in Figure 3, in which the percent error is shown to quickly exceed 5%.

## 5 Discussion

Based on the analysis of the previous section, we see that Fisher's approximation is fairly accurate for "small damping" – that is, damping coefficients of  $0 < \nu < 1$ . Given how quick and simple it is to compute, the approximation could be a very useful tool in modeling circuits within this parameter range, dictated by the inductance and capacitance of the circuit. The process of numerically computing period, though fast, is not as efficient; numerically solving the stiff ODE, testing repeatedly for the convergence of a limit cycle, then measuring the period of this cycle are all fairly computationally intensive. Given the necessity of speed in signal analysis, especially telecommunications, technicians would benefit to be able to perform a single constant-time function to determine the period of the limit cycle rather than a collection of tests.

However, for a fairly low threshold value of  $\nu$ , we lose the benefit of this particular approximation. This could perhaps be improved with a higher-order approximation, either by the Lindstedt method or another approximation method suited to nonlinear ODEs. Yet, even with a more precise computation, the increase of  $\nu > 1$  will lead to explosion of higher-power error terms and thus cause similarly strong divergence with only a small delay. As a result, it may be in the interest of those using unforced van der Pol equations to tend toward low-damping models or circuits if quick computation is a priority.

## References

- [1] Cartwright, M. L. "Balthazar Van Der Pol," *Journal of the London Mathematical Society*, vol. 1 no. 3, pp 367-376, 1960.
- [2] Fisher, E. "The Period and Amplitude of the Van Der Pol Limit Cycle," *Journal of Applied Physics*, vol. 25 no. 3, pp 273-274, 1954.
- [3] Kanamaru, T. "Van der Pol Oscillator," *Scholarpedia*, vol. 2 no. 1, p 2202, 2007.
- [4] "Poincaré-Lindstedt Method," *Supplementary Applied Mathematics*, OCIAM Mathematical Institute, University of Oxford, 2012.

# Flip-Over Threshold for the Double Pendulum

*Julius Elinson*

**Abstract:** The double pendulum is a simple physical system that demonstrates chaotic behavior. The undamped, unforced planar system is characterized by four first-order, non-linear, autonomous differential equations. One measure of the system's sensitivity to initial conditions is the time that must elapse before either pendulum flips over. By studying the flip-over property, the fractal structure of the solution to the double pendulum is uncovered and depicted.

## 1 Introduction

The pendulum system has been widely used to study the physics of oscillatory systems. Composed of a mass at the end of a rod that is attached to a pivot, this system demonstrates a variety of different phenomena as its parameters change, especially those associated with damping or forcing.

A natural extension of the single pendulum is the double pendulum. In its general form, this system is composed of two masses, where one is connected to a fixed pivot and the other is connected to the first mass by a pivot. We will assume that both pivots are constrained to two degrees of motion, and in particular that the motion of the two masses is restricted to the plane.

Modeling the double pendulum lends itself to interesting applications. As the governing equations will demonstrate in §2, the system has no natural frequency. Consequently, this model has been applied to designing buildings for resistance to seismic activity [4]. In addition, a number of systems can be modeled as a double pendulum, such as an arm swinging a baseball bat or golf club. In such models, the arms are treated as the first pendulum and the object being swung is treated as the second pendulum, with the hands acting as a pivot between the two [3].

These modeling applications rely on setting a number of parameters of the system. The two masses, their distribution, and the lengths of the two rods may all need to be set to fit the model to an application. For simplicity, however, a further constrained system will be used in this study. In particular, we will assume that the masses are equal. Moreover, we will also assume that the rods are equal in length and have uniform mass density. Finally, we will only examine the frictionless system where there is no external forcing.

Defining  $\theta_1$  and  $\theta_2$  to be the angles from the vertical to the two rods, the system can be drawn as shown in Fig. 1.

## 2 Governing Equations

To describe the dynamics of the system, we will compute the Lagrangian. Notice that since the rods have uniform mass,  $m$ , the center of mass of each rod is in its geometric center. Moreover, since both rods have length  $\ell$ , defining the origin at the fixed pivot, the cartesian coordinates of the two centers of mass,  $(x_1, y_1)$  and  $(x_2, y_2)$ , are given by:

$$x_1 = \frac{\ell}{2} \sin \theta_1, \quad y_1 = -\frac{\ell}{2} \cos \theta_1, \quad (1)$$

$$x_2 = \ell(\sin \theta_1 + \frac{1}{2} \sin \theta_2), \quad y_2 = -\ell(\cos \theta_1 + \frac{1}{2} \cos \theta_2). \quad (2)$$

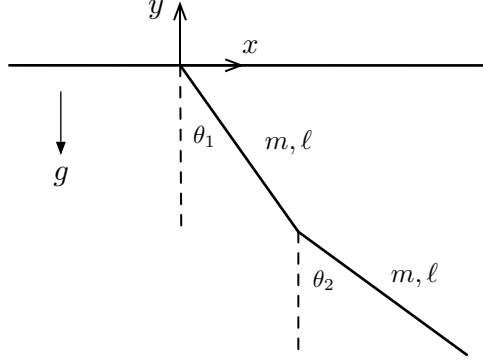


Figure 1: Diagram of the double pendulum system. Both rods are assumed to have uniform mass  $m$  and length  $\ell$ .

The Lagrangian is the difference between the kinetic and potential energies of the system. Letting  $v_1$  and  $v_2$  denote the respective velocities for the two centers of the rods, we thus have

$$L = \frac{1}{2}m(v_1^2 + v_2^2) + \frac{1}{2}I(\dot{\theta}_1^2 + \dot{\theta}_2^2) - mg(y_1 + y_2) \quad (3)$$

$$= \frac{1}{2}m(\dot{x}_1^2 + \dot{y}_1^2 + \dot{x}_2^2 + \dot{y}_2^2) + \frac{1}{2}I(\dot{\theta}_1^2 + \dot{\theta}_2^2) - mg(y_1 + y_2). \quad (4)$$

The moment of inertia,  $I$ , for each rod is given by  $m\ell^2/12$ . Using (1) and (2), the first time-derivatives of the coordinates of both centers of mass can be computed as follows:

$$\dot{x}_1 = \frac{\ell}{2}\dot{\theta}_1 \cos \theta_1, \quad \dot{y}_1 = \frac{\ell}{2}\dot{\theta}_1 \sin \theta_1, \quad (5)$$

$$\dot{x}_2 = \ell(\dot{\theta}_1 \cos \theta_1 + \frac{1}{2}\dot{\theta}_2 \cos \theta_2), \quad \dot{y}_2 = \ell(\dot{\theta}_1 \sin \theta_1 + \frac{1}{2}\dot{\theta}_2 \sin \theta_2). \quad (6)$$

Substituting (1), (2), (5), and (6), as well as the moment of inertia, into (4), yields:

$$L = \frac{1}{6}m\ell^2 \left[ \dot{\theta}_2^2 + 4\dot{\theta}_1^2 + 3\dot{\theta}_1\dot{\theta}_2 \cos(\theta_1 - \theta_2) \right] + \frac{1}{2}m\ell g(3 \cos \theta_1 + \cos \theta_2). \quad (7)$$

Notice that the Lagrangian does not explicitly depend on  $t$ , and thus the Hamiltonian, which is the sum of the potential and kinetic energies, is conserved in the system. This matches intuition since no energy is dissipated. In addition, the Lagrangian can be used to obtain the generalized momenta of the system,  $p_{\theta_1}$  and  $p_{\theta_2}$ :

$$p_{\theta_1} = \frac{\partial L}{\partial \dot{\theta}_1} = \frac{1}{6}m\ell^2 \left[ 8\dot{\theta}_1 + 3\dot{\theta}_2 \cos(\theta_1 - \theta_2) \right], \quad (8)$$

$$p_{\theta_2} = \frac{\partial L}{\partial \dot{\theta}_2} = \frac{1}{6}m\ell^2 \left[ 2\dot{\theta}_2 + 3\dot{\theta}_1 \cos(\theta_1 - \theta_2) \right]. \quad (9)$$

Equations (8) and (9) can be used to obtain expressions for  $\dot{\theta}_1$  and  $\dot{\theta}_2$ . These can then be coupled with the first time-derivatives of the generalized momenta, giving the following four equations of

motion:

$$\dot{\theta}_1 = \frac{6}{m\ell^2} \cdot \frac{2p_{\theta_1} - 3\cos(\theta_1 - \theta_2)p_{\theta_2}}{16 - 9\cos^2(\theta_1 - \theta_2)}, \quad (10)$$

$$\dot{\theta}_2 = \frac{6}{m\ell^2} \cdot \frac{8p_{\theta_2} - 3\cos(\theta_1 - \theta_2)p_{\theta_1}}{16 - 9\cos^2(\theta_1 - \theta_2)}, \quad (11)$$

$$\dot{p}_{\theta_1} = -\frac{1}{2}m\ell^2 \left[ \dot{\theta}_1\dot{\theta}_2 \sin(\theta_1 - \theta_2) + 3\frac{g}{\ell} \sin \theta_1 \right], \quad (12)$$

$$\dot{p}_{\theta_2} = -\frac{1}{2}m\ell^2 \left[ -\dot{\theta}_1\dot{\theta}_2 \sin(\theta_1 - \theta_2) + \frac{g}{\ell} \sin \theta_2 \right]. \quad (13)$$

The governing equations of the double pendulum system, (10)–(13), thus constitute an autonomous system of first-order differential equations. There is no analytical solution to this system; it must be solved numerically [4].

Observe that there are three parameters with dimensions, namely  $\ell$ ,  $m$ , and  $g$ , and three different dimensions in the problem: length, mass and time [1]. Thus we can non-dimensionalize the system by defining a dimensionless time variable,  $\hat{t}$ , as

$$\hat{t} = \sqrt{\frac{g}{\ell}} t, \quad (14)$$

and dimensionless generalized momenta,  $\hat{p}_\theta$ , as

$$\hat{p}_\theta = \sqrt{\frac{\ell}{g}} \cdot \frac{p}{m\ell^2}. \quad (15)$$

Dropping the hats, the non-dimensional system of equations that we will now study becomes

$$\dot{\theta}_1 = 6 \cdot \frac{(2p_{\theta_1} - 3\cos(\theta_1 - \theta_2)p_{\theta_2})}{16 - 9\cos^2(\theta_1 - \theta_2)}, \quad (16)$$

$$\dot{\theta}_2 = 6 \cdot \frac{(8p_{\theta_2} - 3\cos(\theta_1 - \theta_2)p_{\theta_1})}{16 - 9\cos^2(\theta_1 - \theta_2)}, \quad (17)$$

$$\dot{p}_{\theta_1} = -\frac{1}{2}(\dot{\theta}_1\dot{\theta}_2 \sin(\theta_1 - \theta_2) + 3\sin \theta_1), \quad (18)$$

$$\dot{p}_{\theta_2} = -\frac{1}{2}(-\dot{\theta}_1\dot{\theta}_2 \sin(\theta_1 - \theta_2) + \sin \theta_2). \quad (19)$$

Assuming the pendula are initially at rest, the only parameters that will vary in our study are the initial positions.

### 3 Analytical Observations

The initial positions can be characterized as to whether they cause either pendulum to flip-over. In particular, consider the initial dimensionless energy of the system, given by the Hamiltonian. Notice that because both pendula are at rest, all the energy is potential energy.

$$H_0 = -\frac{1}{2} \cos \theta_1 - \frac{1}{2}(2 \cos \theta_1 + \cos \theta_2) \quad (20)$$

$$= -\frac{1}{2}(3 \cos \theta_1 + \cos \theta_2). \quad (21)$$

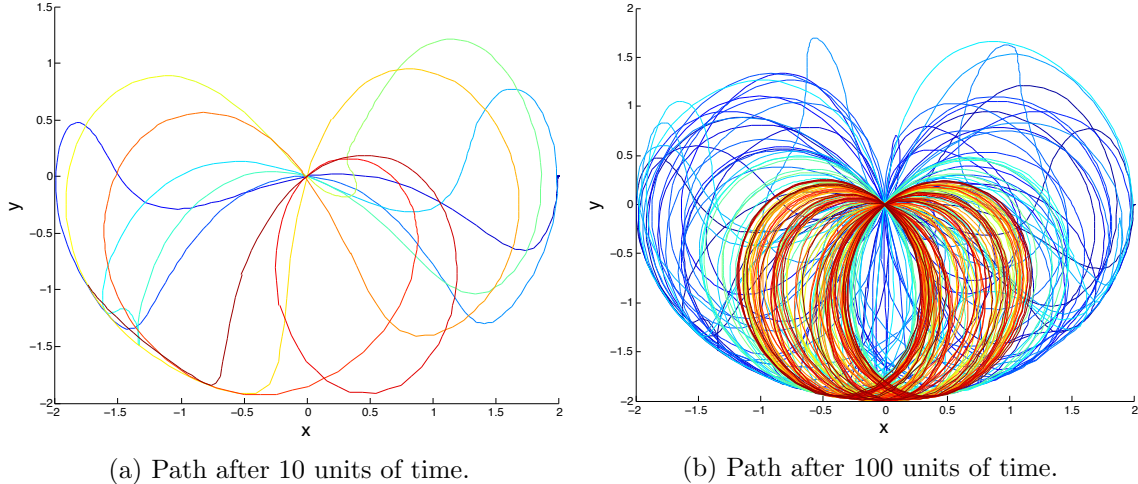


Figure 2: Path of the center of the second pendulum with initial conditions  $\theta_1 = \theta_2 = \frac{\pi}{2}$ . Notice  $3 \cos \theta_1 + \cos \theta_2 = 0 < 2$  and thus a flip-over event is possible for this initial position. As time progress, the path color becomes more red.

A flip-over event occurs when either  $\theta_1 = \pm\pi$  or  $\theta_2 = \pm\pi$ . Notice this can happen with the minimum amount of energy necessary if both pendula are at rest and  $\theta_1 = 0$  and  $\theta_2 = \pm\pi$ . The Hamiltonian at this event would be given simply by:

$$H = -1. \tag{22}$$

In order for a flip-over event to be energetically possible, it must be the case that  $H_0 \geq H$ , which using (21) and (22) implies,

$$3 \cos \theta_1 + \cos \theta_2 \leq 2. \tag{23}$$

Thus there are certain initial conditions in which a flip-over event is impossible, namely inside the region  $3 \cos \theta_1 + \cos \theta_2 > 2$  [5]. However, these analytical techniques do not provide any insight into when a flip-over event will occur for a system starting outside that region; §4 will numerically examine the dynamics of when such an event is physically possible.

## 4 Numerical Results

Analytically solving for the motion of the double pendulum demonstrates that it follows a sporadic and asymmetric path. Fig. 2 shows the path of the second pendulum with initial conditions  $\theta_1 = \theta_2 = \frac{\pi}{2}$ , after 10 and 100 units of time. The color of a point corresponds to the time at the particular position. Dark blue correspond to the earliest times and the more red a point is, the later its timing. The dark red region in Fig. 3b captures one interesting phenomenon where the second pendulum will trace a tight, oscillatory path very rapidly. However, it is not periodic, nor does this behavior persist indefinitely.

One of the interesting properties of the double pendulum is how its behavior defies methodical classification. This is best exemplified by analyzing the time the system takes for either pendulum to flip-over. In §2, it was demonstrated that initial conditions that do not satisfy (23) cannot flip-over. However, there is chaotic motion in the system: slight variations between initial conditions where flip-over is possible can lead to radically different amounts of time required for such an event to occur.

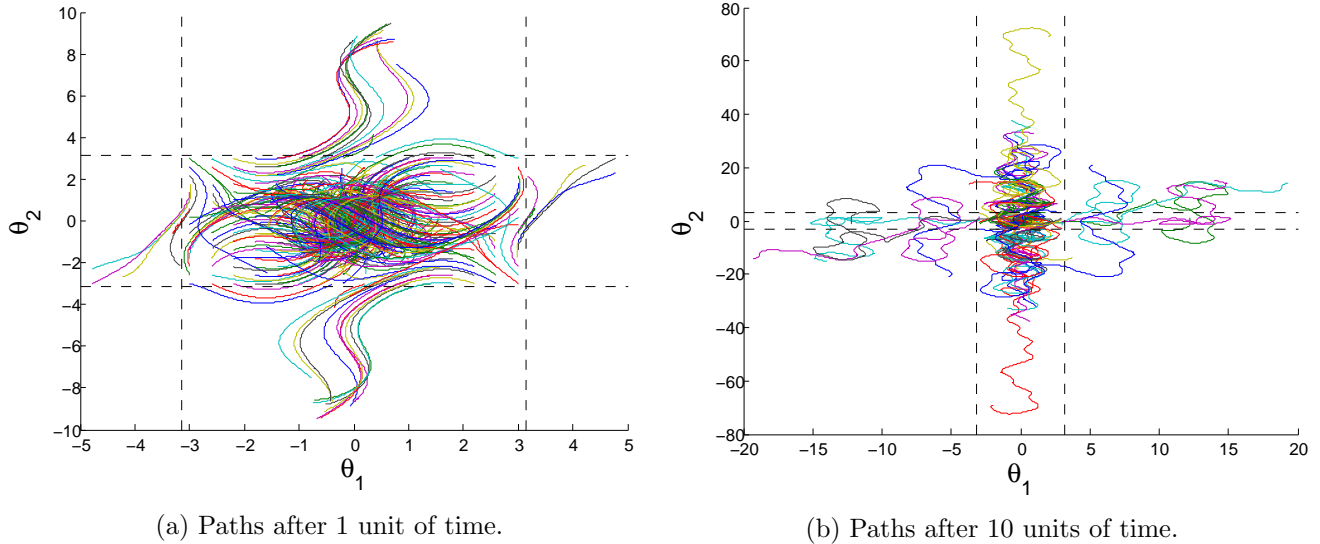


Figure 3: Phase portraits for many different initial conditions, capturing motion for (a) 1 unit of time and (b) 10 units of time. The dotted lines are  $\pm\pi$  and paths that cross them demonstrate a flip-over event. Each color represents the path from a different initial condition.

By examining phase portraits capturing the path of the two angles, as seen in Fig. 3, flip-over events can be seen for some initial conditions with large angles. Fig 3a shows the solution over one unit of time and Fig 3b shows the solution for an order of magnitude longer. The dotted lines mark where either pendulum is completely vertical and thus a path that crosses any of these experiences a flip-over event. It can be seen that some initial conditions quickly flip over, represented by paths that extend outward from the center, while others move to the center and appear to stay there. Moreover, paths emanating from similar initial conditions can be seen to diverge significantly over time. Letting the system run longer, as seen in Fig. 3b, we see it is more common for the second pendulum to flip-over, and to do so multiple times, while only a few paths cross the  $\theta_1 = \pm\pi$  lines.

To further visualize this phenomenon, Fig. 4 is a plot of the time required for a flip-over event to occur for varying initial conditions, assuming both pendula are at rest initially. Calculations were run for the first 600 time steps to check for such an event. The clearly defined oval region in the center matches exactly with the theoretical region determined in (23), where a flip-over event is impossible.

It is interesting to observe the structure at the border between where the system flips over and where it does not. Fig. 4 demonstrates that there are local maxima outside of the central region with peaks scattered throughout. The chaotic fractal structure can be observed by zooming in on a region at the border, as seen in Fig. 5. In this plot with 45,000 points, we see that the regions are not uniform in color intensity, indicating the timing varies significantly with small perturbations in initial conditions. Moreover, it suggests that there is structure at arbitrary scales. These findings are reinforced by Fig. 6, which plots 52,000 points in a small region contained in Fig. 5.

Two simple optimizations were made to run these computationally-intensive calculations. First, using the analytical findings in §2, certain initial conditions can physically never lead to flip-over events and hence no were calculations needed to be ran in this region. Second, symmetry between an initial condition and the negation of both of its angles allowed half of the data to be inferred from the other half.

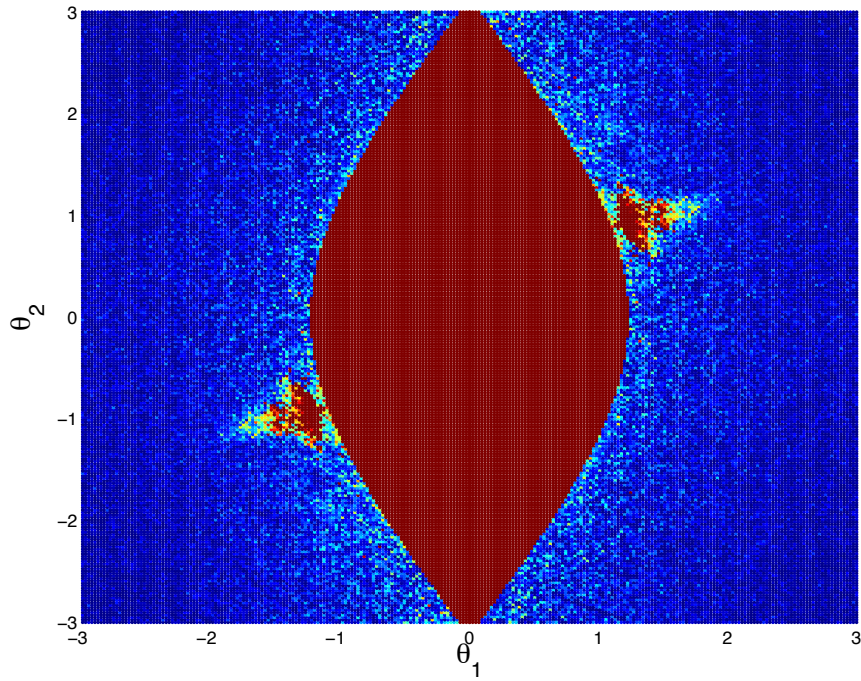


Figure 4: Timing for flip-over events for varying initial conditions. Dark blue represents the shortest time, while red indicates a longer time. Calculations were run for up to 600 time steps; all iterations that did not flip-over in that time are plotted in dark red. The clearly defined middle region depicts the analytical region determined in (23), where a flip-over event is impossible.

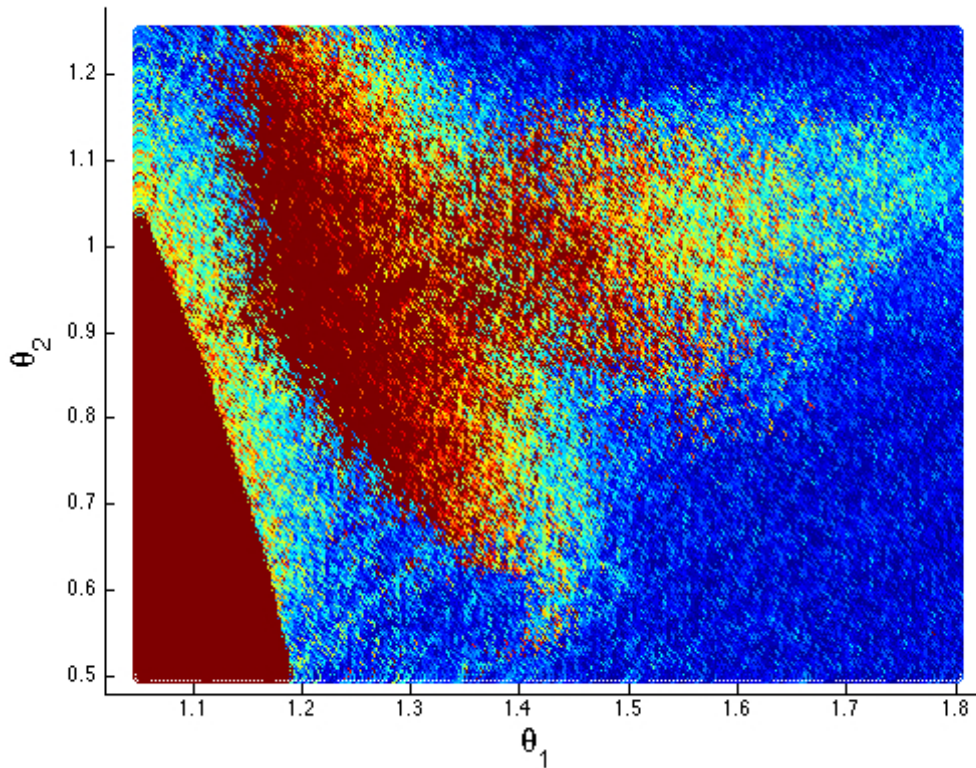


Figure 5: Close-up of Fig. 4 with 45,000 initial conditions in a chaotic region.

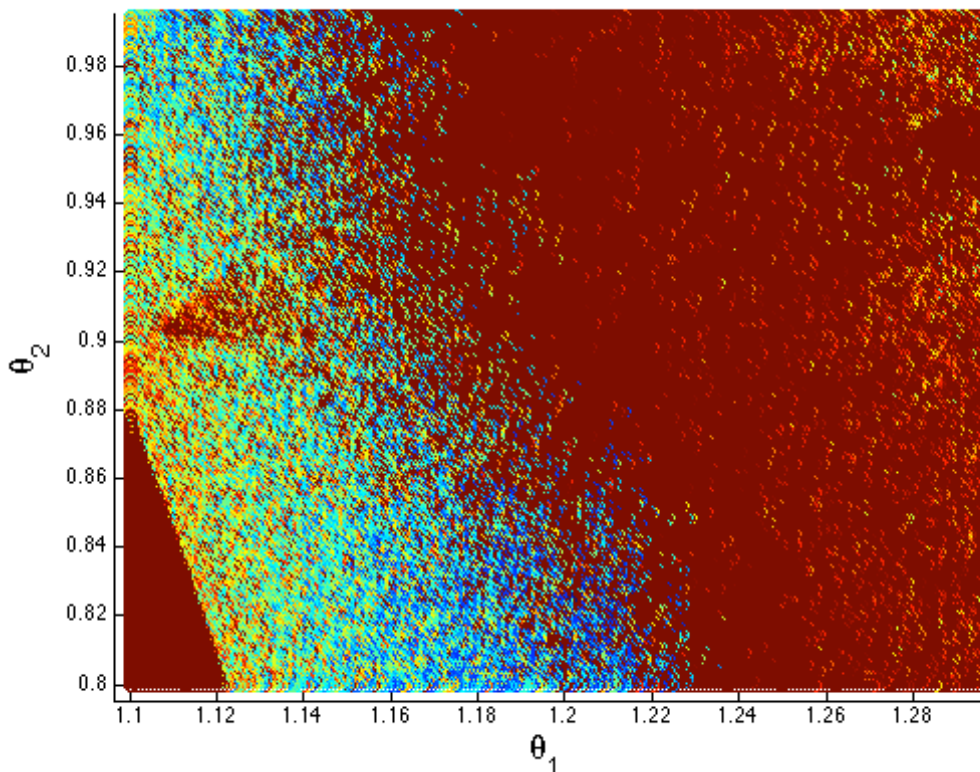


Figure 6: Close-up of Fig. 5 with 52,000 initial conditions sampled near the border of where flip-over events are impossible (seen in the lower left region).

## 5 Discussion

Studying the flip-over events in the pendulum and the dynamics that they follow yields interesting implications. Slight variations in physical properties led to chaotic structure in a temporal one, namely how long it takes for such an event to occur. This is an interesting way that chaos manifests itself in the system dynamics. Moreover, if flipping over is regarded as a measure of instability, then the region that is physically guaranteed to not flip over is of particular interest. With such initial conditions, the stability of the system can be assured, even though the paths that the pendula take are still chaotic. In others words, the angles can be bounded. Moreover, the fractal structure governing the time it takes for the system to become unstable means that it is very difficult to accurately predict when this will happen. Slight variations in the conditions, or simply error in numerical calculations, can alter results dramatically.

This work naturally lends itself to further studies by either relaxing some of the constraints imposed on the problem or by analyzing a pendulum system with  $n$  masses and pivots.

## References

- [1] M. Z. Rafat and M. S. Wheatland and T. R. Bedding, “Dynamics of a double pendulum with distributed mass,” *American Journal of Physics*, Volume 77, Issue 3, pp. 216-223, 2009.

- [2] Gonsalves, Richard, Chaotic Motion in Nonlinear Systems, 2011.
- [3] Tutelman, Dave, The Double-Pendulum Model and the Right Arm, 2010.
- [4] Wikipedia, Double Pendulum — Wikipedia, The Free Encyclopedia, 2013.
- [5] Heyl, Jeremy, The Double Pendulum Fractal, 2008.

# Dynamics of a Forced Duffing's Oscillator

*Kyle Siegel*

**Abstract:** Through a numerical investigation of the Duffing's equation in the time domain and frequency domain interesting phenomena are revealed. Using the amplitude of the periodic forcing function as the control parameter the system response cascades through several bifurcations as the amplitude increases. The system response undergoes a symmetry breaking bifurcation at  $F = 0.1008$ , then cascades through four period doubling bifurcations before reaching chaos at  $F = 0.3408$ . In the chaotic regime the system can be classified as a strange attractor with fractal dimension  $D = 1.51$ . In the frequency domain the amplitude response exhibits hysteresis due to bistability for  $\omega$  in between  $\omega = 1.4$  and  $\omega = 2.2$ .

## 1 Introduction

In this paper the dynamics of a damped, forced Duffing's Oscillator are characterized. At first this system appears to be very similar to a linear, damped pendulum, however it bears much more physical significance, which leads to different dynamics. The governing equations for the linear pendulum, along with many other systems, are derived assuming the small angle approximation, or a linear spring. In the case of the linear pendulum, the governing equation is linearized by applying the small angle approximation. This approximation can be made more accurate using a third order Taylor expansion about the origin of  $\sin x$  yielding  $\sin x \approx x - x^3/6$ . For the assumption of a linear spring there are usually physical constraints that cause a nonlinear restoring force for the spring. When either of these better approximations are made the governing equations that follow can be classified as Duffing's equations.

## 2 Background

The Duffing's Oscillator equation is derived from the movement of a mass subjected to a nonlinear spring force, linear viscous damping, and periodic forcing. A spring becomes nonlinear due to physical constraints in material and setup. For example, when bending a steel beam the material constrains the displacement of the beam within a finite range, and it becomes harder to bend the beam as the displacement is closer to the boundary of this range. This relationship is shown in Figure 1 and is mathematically described by adding a cubic term to Hooke's Law. Note that because of the cubic term this relationship only holds true for small displacement, but is valid for a larger range than the linear approximation.

The linear viscous damping is most commonly the result of air resistance. Using the nonlinear spring relationship and the relationship for linear viscous damping the Duffing's Oscillator equation can be derived by summing the forces on the oscillating mass. This yields

$$\ddot{x} + 2\zeta\dot{x} + \alpha x + \beta x^3 = F \cos(\omega t), \quad (1)$$

where  $\zeta$  controls the damping,  $\beta$  controls the nonlinearity in the restoring force, and  $F$  is the amplitude of the periodic forcing with frequency  $\omega$ .

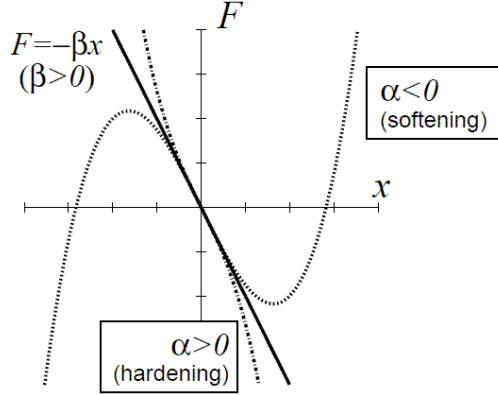


Figure 1: Force versus displacement for nonlinear spring with equation  $F(x) = -\beta x - \alpha x^3$ . The sign of alpha indicates if the spring hardens or softens [1].

### 3 Periodic Analysis

Using  $F$  as the control parameter, with  $\zeta = 0.05$ ,  $\alpha = 1$ ,  $\omega = 1.4$ , and  $\beta = 1$ , the solution transitions through several forms after passing through several bifurcations. Phase portraits and Poincare sections offer an effective view of the dynamics of the system at different places in this parameter space.

#### 3.1 Bifurcations

As  $F$  increases slowly the system goes through a supercritical pitchfork bifurcation at  $F = 0.101$ . In this bifurcation the system goes from having one stable limit cycle to having two stable limit cycles. This is a symmetry breaking bifurcation and the phase portrait before and after this bifurcation can be seen in Figure 2.

As  $F$  continues to increase the system goes through a cascade of period doubling bifurcations, the first occurring at  $F = 0.309$ . The bifurcations are also supercritical pitchfork bifurcations [2]. The phase portrait can be used to view dynamics of the system before and after this bifurcation. As seen below in Figure 3 before period doubling the limit cycle loops once before closing, where after period doubling the limit cycle loops twice before closing.

From  $F = 0.309$  to  $F = 0.3408$  the system undergoes four period doubling bifurcations and then transitions to chaos at  $F = 0.3408$ . This can be observed from the bifurcation diagram seen in Figure 4.

Chaos is represented in the bifurcation diagram with the region of points beyond  $F = 0.3408$  [4]. This shows the system is not converging to a limit cycle, as  $x$  has a different value at each multiple of the period. This can be confirmed by looking at the phase space, in which no closed limit cycle is reached.

#### 3.2 Strange Attractor

As seen in the bifurcation diagram as  $F$  increases past  $F = 0.3408$  the system reaches chaos. A helpful tool to visualize a dynamical system in chaos is a Poincare section. When looking at the phase portrait of the Duffing's oscillator in chaos it is hard to determine that there is no convergence.

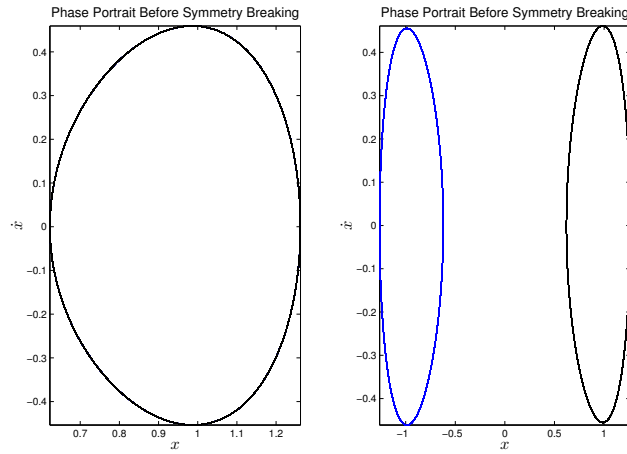


Figure 2: Left graph: phase portrait for  $F = 0.1008$  with initial conditions  $x(0) = 0$  and  $\dot{x}(0) = 0$  and  $x(0) = 0.5$  and  $\dot{x}(0) = 0.2$ , which as seen yield the same phase portrait. Right graph: Phase portrait using the same initial conditions as the left graph with  $F = .0102$ , this time yielding two separate limit cycles.

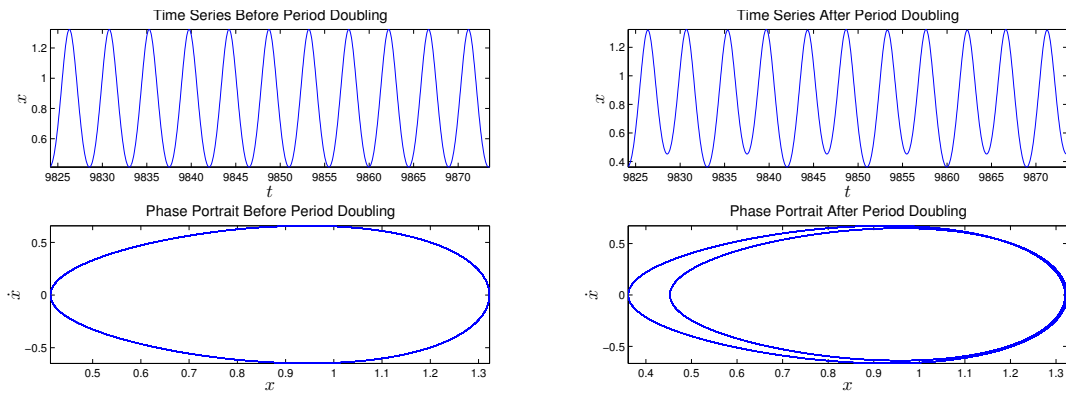


Figure 3: Time series and phase portraits for system response before period doubling for  $F = 0.3$  (left) and after period doubling for  $F = 0.31$  (right).

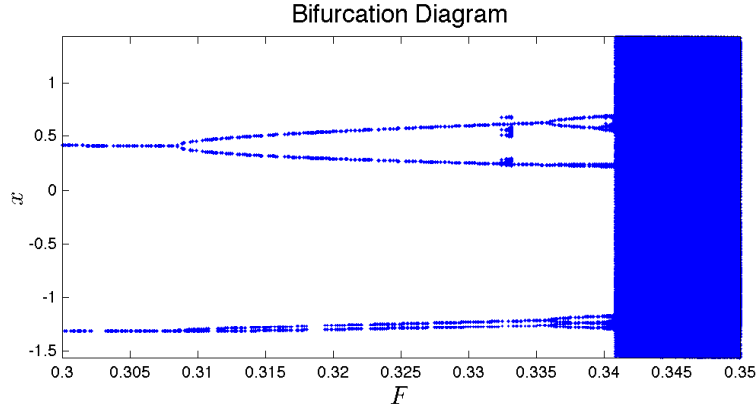


Figure 4: Bifurcation diagram for initial conditions  $x(0) = 0$  and  $\dot{x}(0) = 0$ , with  $\zeta = 0.05$ ,  $\alpha = 1$ ,  $\omega = 1.4$ , and  $\beta = 1$ . Notice the four period doubling cascades, and the two separate branches for the two stable limit cycles.

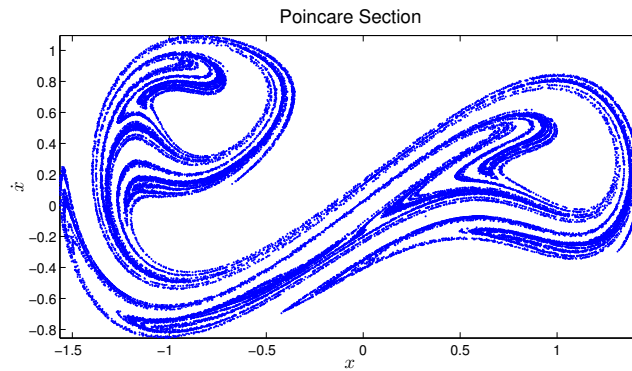


Figure 5: Poincaré section for initial conditions  $x(0) = 0$  and  $\dot{x}(0) = 0$ , with  $\zeta = .05$ ,  $\alpha = 1$ ,  $F = 0.35$ ,  $\omega = 1.4$ , and  $\beta = 1$ .

The Poincaré sections show a point in the phase space for each period of the forcing function. This can be seen in Figure 5.

Upon looking at the Poincaré section above, it appears it is not space filling, yet there appears to be structure on all scales. This is similar to classic fractals, giving this region of the solution the name a strange attractor. However, the strange attractor is not completely self similar, and to classify the degree of self similarity the correlation dimension can be found [2].

The calculated correlation dimension of  $D = 1.51$  indicated the strange attractor is somewhere between a line and an area. The dimension is close to a classic fractal, the Sierpinski triangle.

## 4 System Response

The system does not only display interesting phenomena in the time domain, it also has interesting phenomena in the frequency domain because of the nonlinearity.

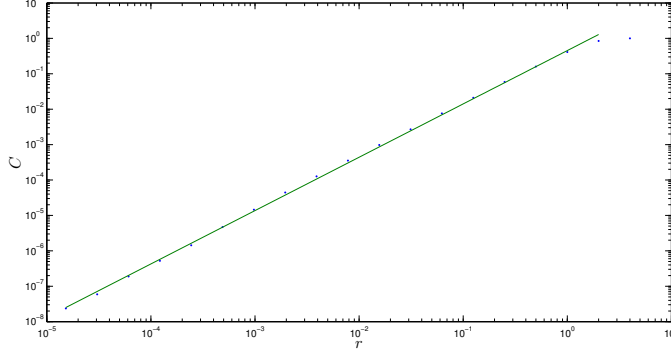


Figure 6: The correlation integral  $C(r)$  versus  $r$  for the strange attractor shown in Figure 5, using a 13,000 point sample. The least-squares line on the log-log plot yields a correlation dimension of the Poincare section of approximately  $D = 1.51$ .

#### 4.1 Harmonics

To determine the harmonics of the system an approximation of the solution to the Duffing's oscillator can be determined. This solution can be found using the Principle of Harmonic Balance. First assume the solution to a first order harmonic approximation taking the form  $x_0(\tau) = A \cos \tau + B \sin \tau$  where  $\tau$  is dimensionless time [5]. Substituting this into Equation 1 yields

$$\begin{aligned} & \left( -(1 - \alpha - \frac{3}{4}\beta(A^2 + B^2))A + 2\zeta B \right) \sin \tau \\ & + \left( -(1 - \alpha - \frac{3}{4}\beta(A^2 + B^2))B + 2\zeta A \right) \sin \tau + \frac{1}{4}\beta(A^2 - 3B^2)A \cos 3\tau \\ & + \frac{1}{4}\beta(3A^2 - B^2)B \sin(3\tau) = F \cos \tau \end{aligned} \quad (2)$$

The first approximation is only concerned with the first harmonic, therefore the third harmonic terms can be ignored, and coefficients can be equated. This yields

$$A = -(1 - \alpha - \frac{3}{4}\beta \frac{(A^2 + B^2)}{F}), \quad B = 2\zeta \frac{(A^2 + B^2)}{F}, \quad (3)$$

where  $F^2 = [(1 - \alpha - \frac{3}{4}\beta(A^2 + B^2))]^2 + (2\zeta)^2(A^2 + B^2)$ . From this it can be seen that the first harmonic of the system is  $\Omega = 1$ . To approximate the second harmonic a second approximation is assumed in the form

$$x(\tau) = (A + \epsilon A_1) \cos(\tau) + (B + \epsilon B_1) \sin(\tau) + \epsilon A_3 \cos(3\tau) + \epsilon B_3 \sin(3\tau) \quad (4)$$

where  $\epsilon$  is a small correction parameter that indicated the order of magnitude among coefficients. Substituting this approximation into Equation 1 and equating coefficients yields a system of linear equations that can easily be solved, but whose solution is outside the scope of this paper. From the second approximation, two new harmonics,  $\Omega = \frac{1}{3}$  and  $\Omega = 3$ , are determined [5].

These harmonics can be numerically found by finding the Fourier series coefficients of the time series after the system has converged to a limit cycle. The harmonics can be seen in Figure 7.

Notice that in the top plot and middle plot in Figure 7 there are harmonics at the first three multiples of  $\omega = 1.4$ . Also because the middle plot is for  $F$  after the first period doubling bifurcation

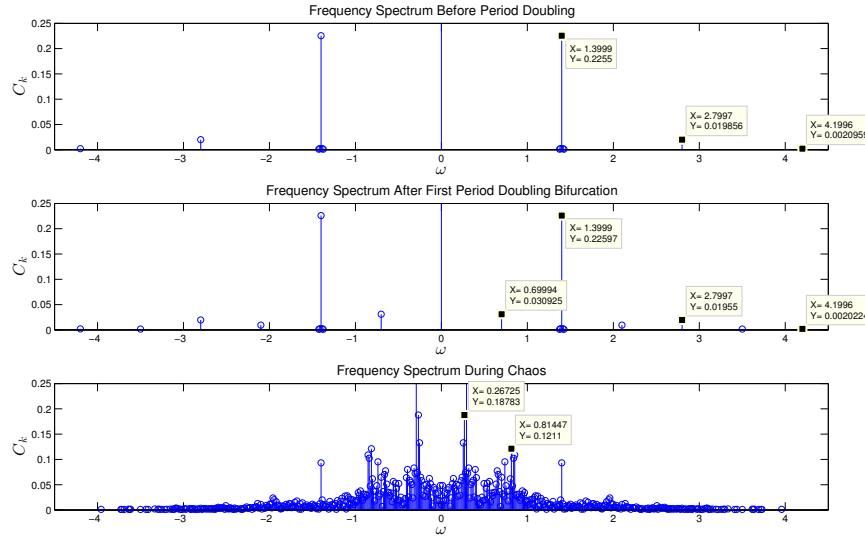


Figure 7: The Fourier series coefficients for  $x(t)$  once it has converged to the limit cycle for  $F = 0.3$  (top), and period doubled limit cycle for  $F = 0.31$  (middle). The coefficients were also found for  $F = 0.35$  (bottom), in which  $x(t)$  is chaotic.

a harmonic at  $\omega = \frac{1.4}{2} = .7$  can be seen, as well as its first 3 multiples. So far this agrees with the results from using the principle of harmonic balance with the exception that no harmonic at  $\Omega = \frac{1}{3}$  is seen. However, it can be observed that in the bottom graph when  $x(t)$  is chaotic, harmonics are found at  $\omega = 0.814$  and  $\omega = 0.267$ , which is exactly one-third of the  $\omega = 0.814$  harmonic. Because the principle of harmonic balance yields an approximation it should not be surprising these harmonics are slightly off of the predicted harmonics [5]. From these harmonics the resonances of the system can be estimated. It is known that resonances are close to the natural frequencies of the system, especially with small damping. Therefore secondary resonances are observed due to nonlinearity.

## 4.2 Amplitude Response

To determine the amplitude response the principle of harmonic balance can be used again, but this time using a first approximation of the form  $x_0(t) = A \cos \omega t + B \sin \omega t$ . Substituting this into Equation 1, equating coefficients, and solving for the magnification factor  $M = \frac{R}{F}$  yields

$$M = \frac{R}{F} = \frac{1}{\sqrt{(\omega^2 - \alpha - \frac{3}{4}\beta R^2)^2 + (2\zeta\omega)^2}} \quad (5)$$

where  $R^2 = A^2 + B^2$ , which is the square of the amplitude of the response. Solving Equation 5 for  $R$  at different values of  $\omega$  gives the amplitude response of the system in the frequency domain, shown in Figure 8.

The peak bending in the amplitude response is the hallmark of hardening response. As the excitation amplitude is increase the peak bends further to the right [3]. If the nonlinear terms was negative, spring softening would occur and the peaks would bend to the left [3].

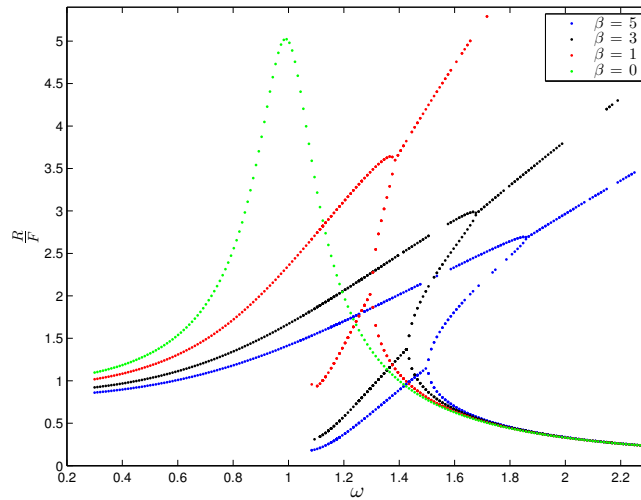


Figure 8: The magnification factor for different values of  $\beta$ . Note that for  $\beta = 0$  the expected result showing resonance at  $\omega = 1$ . For non-zero  $\beta$  the resonance is a function of amplitude, which results in the peak bending. Parameter values were  $\zeta = 0.1$ ,  $\alpha = 1$ ,  $F = 0.3$ .

### 4.3 Stability and Hysteresis

In practice Figure 8 can never be experimentally determined. This is because the system exhibits hysteresis, due to ranges in the solution being unstable. The instability regions can be found numerically. By solving the Duffing equation until it converges then finding the amplitude of the response an experiment is essentially simulated because the solution will not converge to an unstable limit cycle. This was done over a range of frequencies and compared to amplitude response found above (see Figure 9).

It can be seen that the experimentally determined amplitude response has a discontinuity at  $\omega = 1/4$ . This is because the multiple solutions for each  $\omega$  as seen in Figure 8 are unstable. This jump is known as hysteresis, and is a result of the direction  $\omega$  is moving. It is a result of a subcritical bifurcation in the frequency domain. The forward path is displayed in Figure 9, but the path as a result of decreasing  $\omega$  can only be determined experimentally. For further analysis the fixed points in the amplitude- $\omega$  plane can be found and the eigenvalues of the system can be found at these points to determine stability.

## 5 Summary

Based upon computations and discussion several conclusions can be made. First, the presence of the cubic nonlinearity does not allow for a closed form solution to be obtained. Second, the system shows multiple harmonics beyond its natural frequency, and thus has secondary resonances. Third, the oscillator exhibits hardening, or softening behavior based on the sign of the cubic term. Lastly, the nonlinearity results in non unique solutions for the same parameter values.

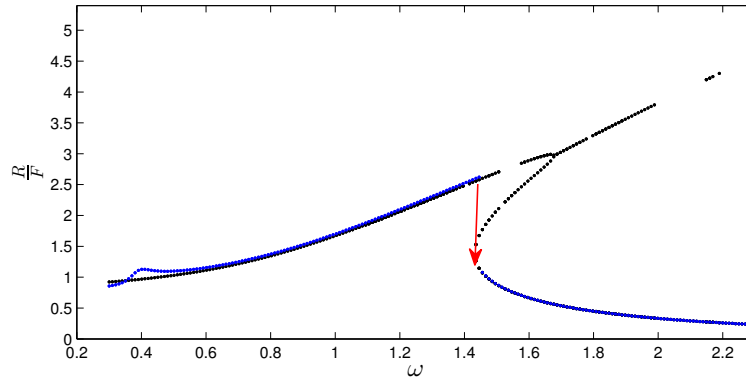


Figure 9: The amplitude response determined with the approximate solution for the magnification factor (black) and the amplitude response found numerically by solving the differential equation and determine the amplitude in the time domain (blue). Parameter values were  $\zeta = .1$ ,  $\alpha = 1$ ,  $F = .3$ , and  $\beta = 3$ .

## References

- [1] Takashi Kanamaru, *Duffing oscillator*. Scholarpedia, 3(3):6327.
- [2] Jeffrey R. Chasnov, *Scientific Computing*. San Francisco, California, 2013.
- [3] Tamas Kalmar-Nagy and Balakumar Balachandran, *Forced harmonic vibration of a Duffing oscillator with linear viscous damping*. Texas A and M University, USA.
- [4] *The Duffing Equation*. physics.ucsc.edu/ peter/242/duffing.pdf.
- [5] Chihiro Hayashi, *Nonlinear Oscillations in Physical Systems*. Princeton, New Jersey, 1985.

# Degree m Polynomial Fractal Sets

*Ben Corr*

**Abstract:** Fractal sets can be generated by applying Newton's method to a polynomial with complex roots. We can graph these sets by shading regions of the complex plane according to the root found from using Newton's Method with that point as an initial condition. Various properties of the generating polynomial function were altered, to investigate the effects on the corresponding fractal pattern and graph. Altering the degree of the polynomial or the constant term changed the graph in predictable ways, whereas adding additional terms increased the complexity of the graphs in a more nuanced manner.

## 1 Introduction

A polynomial fractal set is found by applying Newton's method to a polynomial with complex roots. Most values for initial conditions will converge to one of the roots of the polynomial, but a boundary set can be found where the iterations do not converge, and this boundary often forms an intricate fractal pattern when plotted on the complex plane. This paper will investigate the patterns found when searching for polynomial fractal sets on equations of varying degree  $m$ , and will highlight interesting consequences of performing Newton's Method on such equations.

Before we begin the analysis, we quickly review the procedure of using Newton's Method to approximate roots of an equation. Newton's Method is an iterative procedure that uses a function and its derivative to generate more and more precise approximations of a root of the function. We repeatedly apply the relation

$$z_{n+1} = z_n - \frac{f(z_n)}{f'(z_n)}$$

until we converge at a value of  $z_n$  that satisfies  $f(z_n) = 0$ . Newton's Method is sensitive to the initial  $z_0$  value provided - different initial conditions will converge to different roots, or may not converge at all, depending on the function.

We can create interesting graphs by shading the complex plane according to the root found by using those coordinates as the initial condition for Newton's Method. Fractal Sets are the fractal patterns that appear as the boundary between colored regions after the iterative process. We use Matlab to generate graphs of Fractal Sets so we can interpret their behavior, and look for a potential relationship between the polynomial function and the corresponding Fractal Set. We are able to do this by modifying `newton_fractal_3.m`, code for solving the fractal set generated by  $z^3 - 1 = 0$ , that was written and distributed by Professor Chasnov.

An example of a simple fractal set is one generated by the function  $x^3 - 1 = 0$ , which has roots of 1 and  $-1/2 \pm i\sqrt{3}/2$ . In Figure 1, red corresponds to regions that converge to 1, blue to regions that converge to  $-1/2 + i\sqrt{3}/2$ , and green to regions that converge to  $-1/2 - i\sqrt{3}/2$ .

## 2 Governing equations

The equations used in this paper are a group of different polynomials with complex-valued roots. The initial investigation is a study of the degree of the polynomial, so we apply Newton's Method to equations of the form  $z^m - 1 = 0$ , where  $m \in 3, 4, 5, 6$ .

Figure 1: The fractal set generated by  $z^3 - 1 = 0$

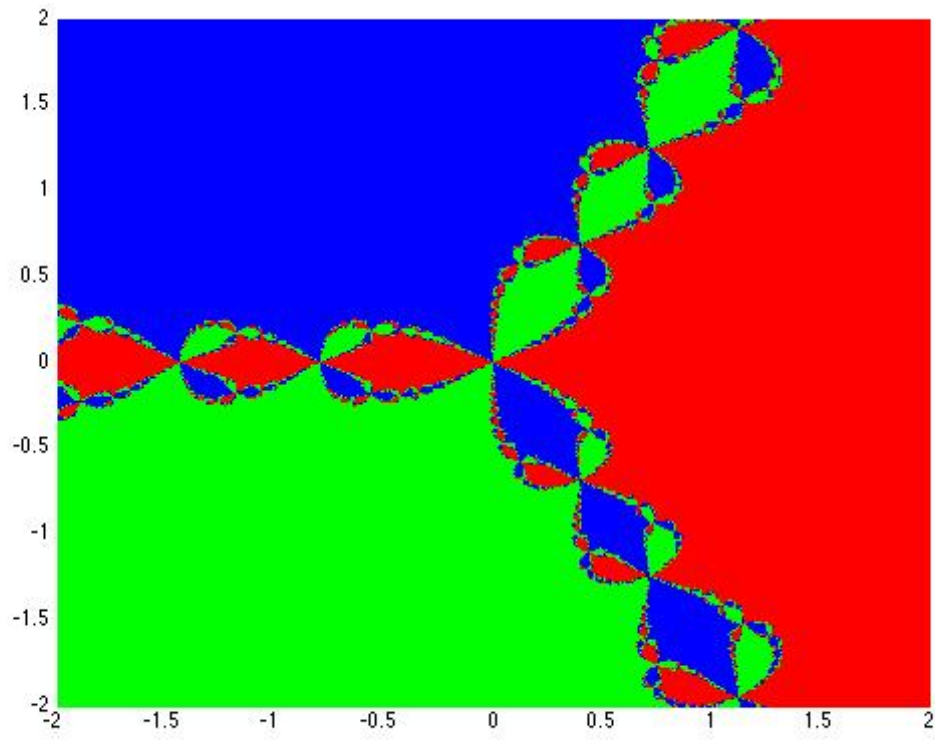
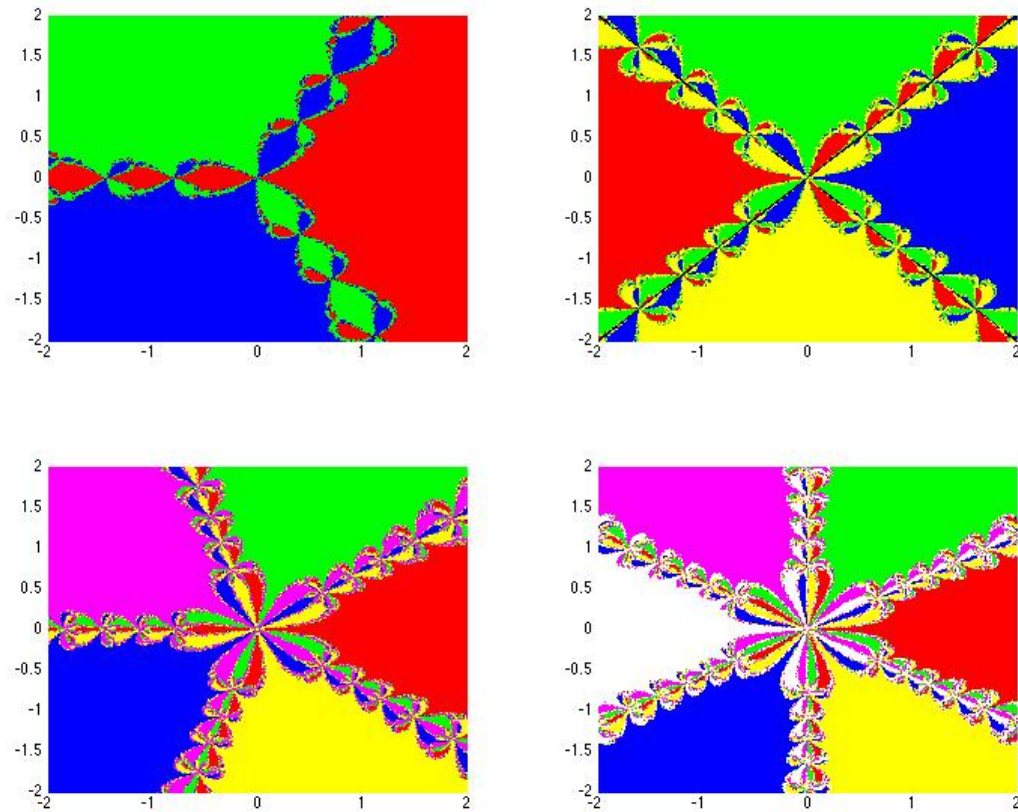


Figure 2: The fractal sets generated by changing the degree  $m$ . Top left is  $z^3 - 1 = 0$ , Top right is  $z^4 - 1 = 0$ , Bottom left is  $z^5 - 1 = 0$ , Bottom right is  $z^6 - 1 = 0$



Another set of equations to consider are those with multiple  $z$  terms, along the lines of  $z^a + z^b - 1 = 0$ , with  $a \neq b$ . We explore the effect of varying these exponents.

### 3 Results

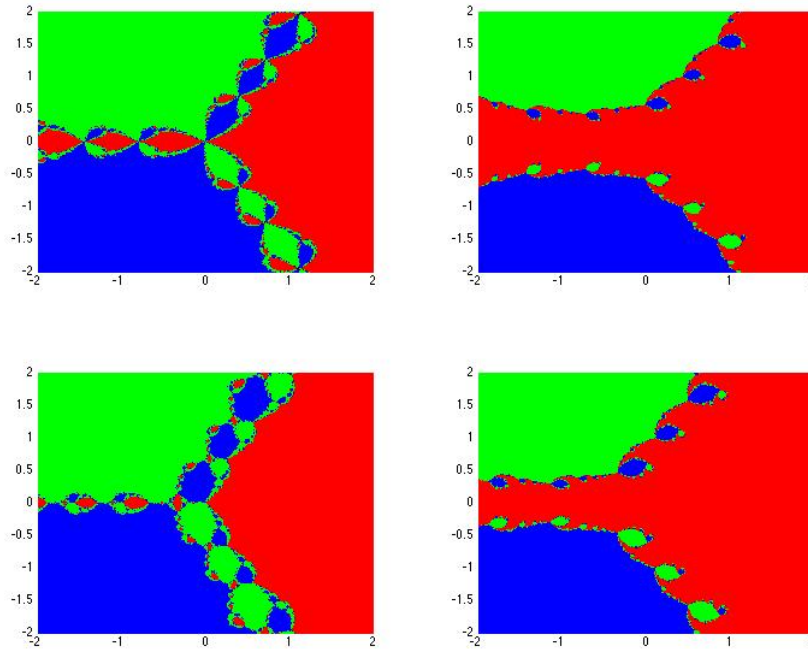
#### 3.1 Changing the Degree of $m$

Figure 2 shows the effect of increasing  $m$  in the polynomial function  $z^m - 1 = 0$ . Note the increasing complexity of each branch of fractal patterns as  $m$  increases, and that the number of branches is exactly equal to  $m$ .

#### 3.2 Adding Additional Terms

We also explore the effects of setting  $\alpha = 1$  and  $\beta = 1$  in the equation  $z^3 + \alpha z^2 + \beta z - 1 = 0$ , these can be seen in Figure 3. We then explore the effects of setting  $\alpha = 1$ ,  $\beta = 1$ , and  $\gamma = 1$  in the equation  $z^4 + \alpha z^3 + \beta z^2 + \gamma z - 1 = 0$ , these can be seen in Figure 4 and Figure 5.

Figure 3: From top left clockwise:  $z^3 - 1 = 0$ ,  $z^3 + z - 1 = 0$ ,  $z^3 + z^2 - 1 = 0$ , and  $z^3 + z^2 + z - 1 = 0$



## 4 Discussion

Changing different properties of our polynomial function allows us to manipulate the corresponding fractal set in predictable ways. As seen in Figure 2, varying the degree of  $m$  in the equation  $z^m - 1 = 0$  will cause several changes in the graph of the fractal set. Primarily, we see  $m$  lines with fractal patterns branching out from the origin of the coordinate plane, so we know that varying  $m$  will vary the number of fractal branches that we observe. We also see that inside the base of each branch is  $m - 2$  different regions, and the associated roots of these regions change as you cycle around the  $m$  branches - this creates the ‘flower’ that we see centered around the origin.

Figure 6 shows us a larger view of the center of the degree 5 fractal, where we can clearly see that each of the 5 regions has large chunks of 3 colors, surrounded by intricate fractal boundaries.

Similarly, Figure 7 shows us a larger view of the center of the degree 6 fractal, where we can see that each of the 6 regions has large chunks of 4 colors.

One final nuance tied to the value of  $m$  is the number of self-repeating ‘regions’ of each branch. As  $m$  increases, so does the amount of times that the fractal pattern repeats before escaping the axis we defined (from  $x = -2, y = -2$  to  $x = 2, y = 2$ ). We thus create more and more intricate fractal patterns on the branches as we increase  $m$ .

Adding additional polynomial terms was not as consistently predictable, but did allow for far more interesting graphs. Portions of the branches become distorted and asymmetrical as the function becomes asymmetrical. For example, we see in Figure 8 that a symmetric function, such as  $f(z) = z^4 + z^2 - 1$  where  $f(z) = f(-z)$ , retains symmetry across the  $y$  axis in the associated fractal set, whereas an asymmetric function such as  $f(z) = z^4 + z^3 - 1$  does not.

Figure 4: From top left clockwise:  $z^4 - 1 = 0$ ,  $z^4 + z - 1 = 0$ ,  $z^4 + z^2 - 1 = 0$ , and  $z^4 + z^3 - 1 = 0$

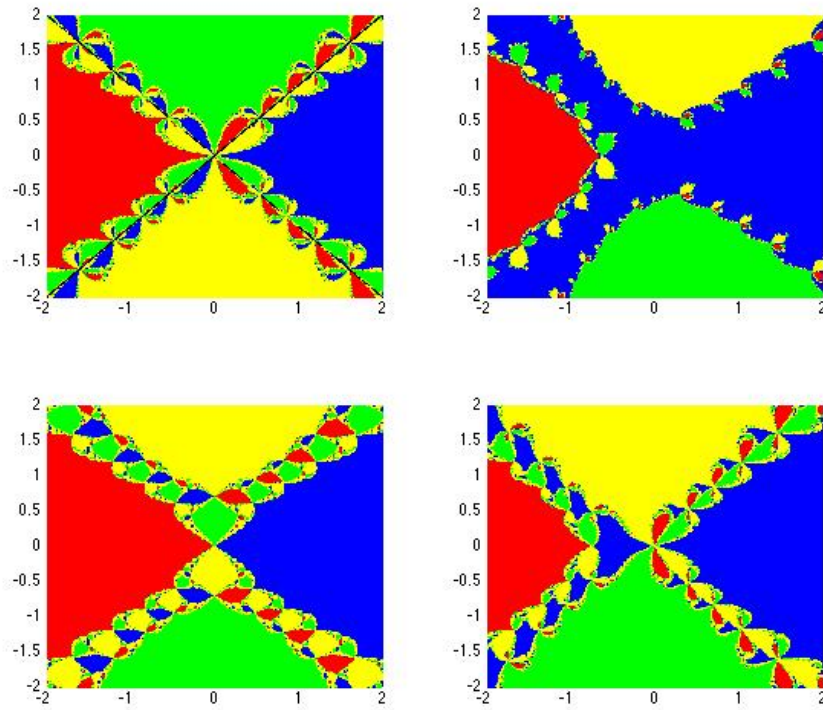


Figure 5: From top left clockwise:  $z^4 + z^2 + z - 1 = 0$ ,  $z^4 + z^3 + z - 1 = 0$ ,  $z^4 + z^3 + z^2 - 1 = 0$ , and  $z^4 + z^3 + z^2 + z - 1 = 0$

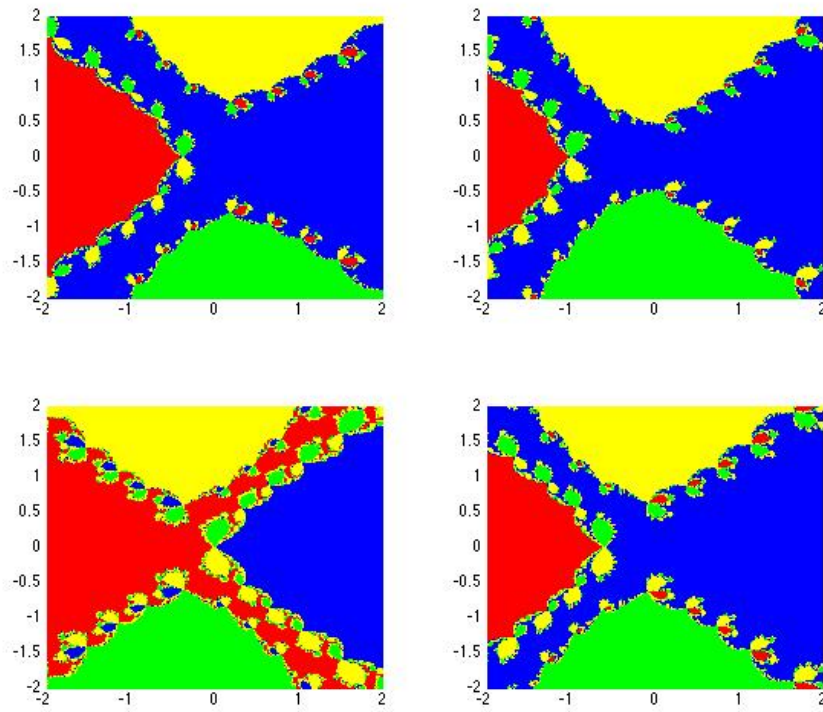


Figure 6: A blown-up version of the center of the  $z^5 - 1$  fractal set

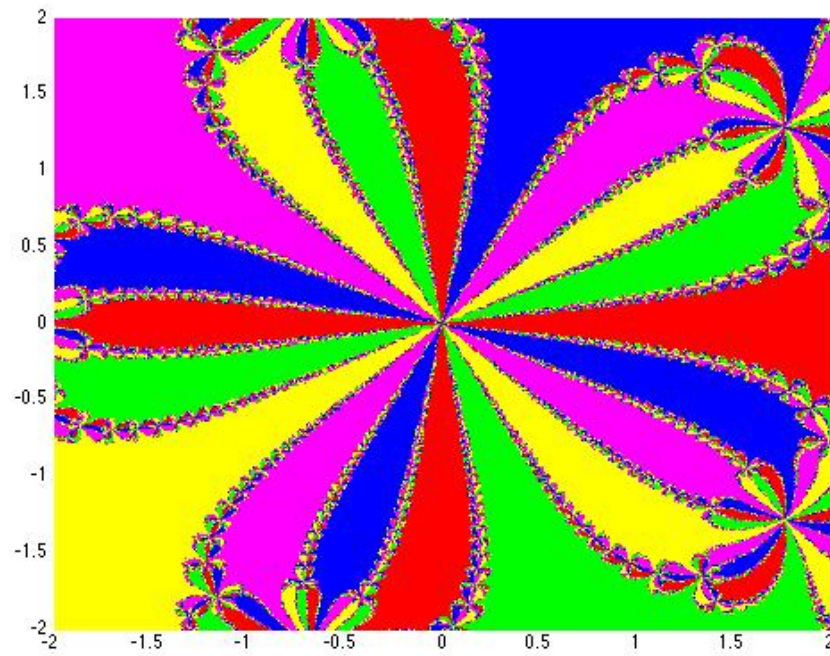


Figure 7: A blown-up version of the center of the  $z^6 - 1$  fractal set

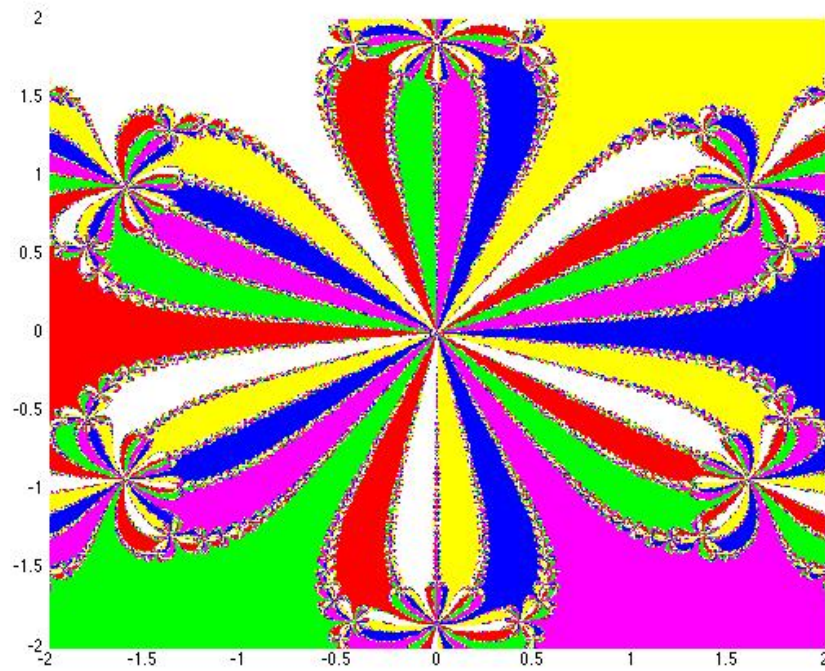
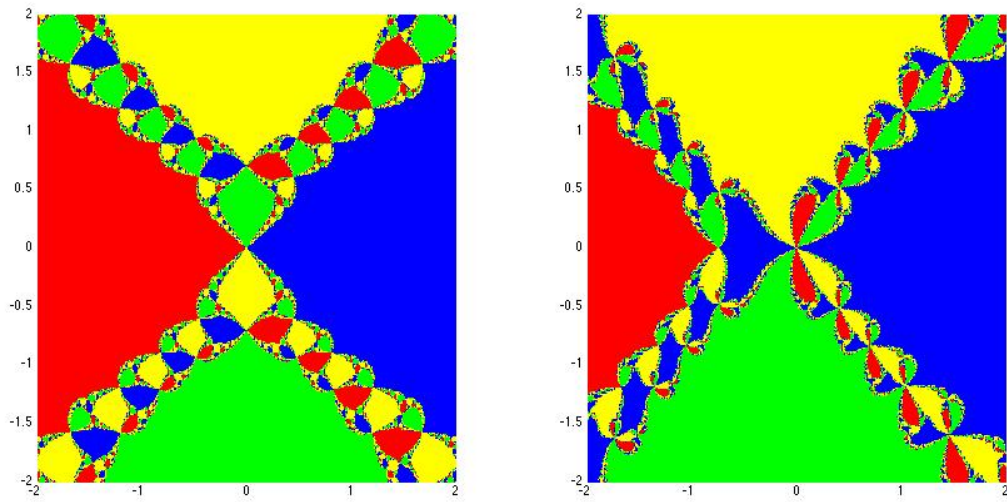


Figure 8: Comparing a symmetric fractal set with an asymmetric one



**Acknowledgments:**

I would like to thank Professor Chasnov for his feedback on this paper, as well as his excellent sample code which was used to generate my own code to solve these equations.

**References:**

1. newton\_fractal\_3.m, taken from the course website at <http://www.math.hmc.edu/math164-01/>.

# Chaotic Behaviors of Chua's Circuit

Tianyou Gu  
Pomona College, CA.

## Abstract

This paper explores the chaotic behaviors of Chua's circuit, one of the simplest non-linear circuits that exhibit complex dynamical behaviors. Various basins of attraction of Chua's circuit including the classic double-scroll attractor are plotted and a bifurcation analysis is performed to study the period-doubling route to chaos. Moreover, the recently-discovered Chua's hidden attractor is exhibited.

## 1 Introduction

The Chua's circuit, introduced in 1983 by Leon O. Chua, is a simple autonomous electronic circuit that exhibits classic and complex dynamical behaviors, including chaos which shows a variety of attractors and bifurcation phenomena. Apart from being the "Paradigm for Chaos", Chua's circuit is also widely applied in secure communications systems, visual sensing, neural networks and music thanks to its supreme simplicity and robustness.

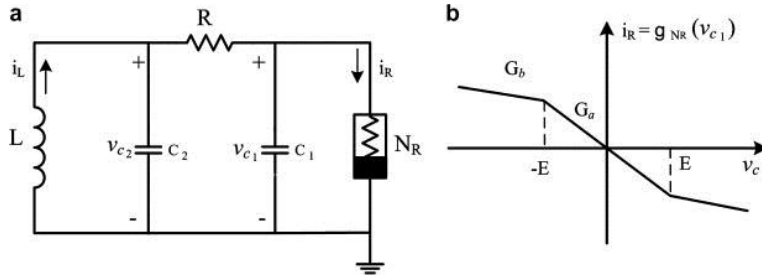


Figure 1: *Chua's Circuit Components: (a) Chua's circuit, and (b) v-i characteristics of the piecewise linear resistor (from [1] [L. Gmez-Guzmn et al, 2009]).*

Chua's circuit (Fig. 1) is a piecewise-linear third-order circuit. It is the simplest circuit possible that meets all the criteria for displaying chaotic behavior. As shown in the figure, the energy storage elements are two capacitors  $C_1$  and  $C_2$  and an inductor  $L$ . The active resistor  $R$  is in series between the two capacitors. And there is a nonlinear resistor  $N_R$ , also known as Chua's diode, connected in parallel with the energy storage elements. Chua's diode is a type of two-terminal, nonlinear resistor which can be described with piecewise-linear equations.

The paper is organized as follows. In Section 2 we derive the dimensionless governing equations. In Section 3, we use the fifth-order Runge-Kutta method to numerically solve the system of dimensionless functions(4)-(6) and study the chaotic patterns of Chua's circuit. Then we apply the analytical-numerical method in [2] to find the "hidden attractor" discovered by Kuznetsov N. *et al* in 2010. In Section 4 we delve into the bifurcation phenomenon of Chua's circuit by plotting

the period-doubling bifurcation diagram using the parameter values of [3] and validate with the calculated bifurcation points values in [3], which uses the local stability analysis to determine the points where the trajectory loses stability and double in period.

## 2 Governing Equations

The dynamics of the circuit is described by:

$$C_1 \frac{dv_{C1}}{dt} = R^{-1} (v_{C2} - v_{C1}) - g(v_{C1}), \quad (1)$$

$$C_2 \frac{dv_{C2}}{dt} = -R^{-1} (v_{C2} - v_{C1}) + i_L, \quad (2)$$

$$L \frac{di_L}{dt} = -v_{C2}, \quad (3)$$

where

$$g(v_{C1}) = G_b v_{C1} + \frac{1}{2} (G_a - G_b) (|v_{C1} + B_p| - |v_{C2} - B_p|)$$

for Chua's diode with  $v_{C1}$ ,  $v_{C2}$  and  $i_L$  denoting the voltage across  $C_1$ , voltage across  $C_2$  and current through  $L$ , respectively. By scaling the variables, we obtain the system of state equations in dimensionless form:

$$\dot{x} = \alpha((y - x) - h(x)) \quad (4)$$

$$\dot{y} = x - y + z \quad (5)$$

$$\dot{z} = -\beta y \quad (6)$$

where

$$x = v_{C1}/B_p, y = v_{C2}/B_p, z = i_L R/B_p, m_0 = G_a R, m_1 = G_b R, \alpha = C_2/C_1, \beta = C_2 R^2/L,$$

and

$$h(x) = m_1 x + \frac{1}{2} (m_0 - m_1) (|x + 1| - |x - 1|),$$

is the characteristic function of the piecewise linear resistor, with  $m_0$  and  $m_1$  representing the slopes of the outer and the inner regions.

## 3 Chaotic Attractors

Portraits ranging from limit cycles, period doubling, single-scroll strange attractor, to the famous double-scroll attractor can be obtained from Chua's circuit. By fixing the parameters of the equations (4)-(6) at  $\alpha = 15.6$ ,  $m_0 = -8/7$  and  $m_1 = -5/7$ , and varying the parameter  $\beta$  from the critical values  $\beta = 60.81$  to  $\beta = 25$ , one can observe a classic period-doubling bifurcation route to chaos.

Fig. 2 shows that at  $\beta = 45$ , we have a pair of limit cycles corresponding to different initial values. The single-loop limit cycle represents a periodic pattern spawned by a Hopf bifurcation process, which would occur when a pair of complex conjugate eigenvalues at the equilibrium point of this circuit crosses the imaginary axis.

Fig. 3 exhibits the period doubling observed at  $\beta = 35$ . Then to understand how the limit cycles evolve into strange attractors, we only graph the  $x - y(v_{C1} - v_{C2})$  section for simplicity. As

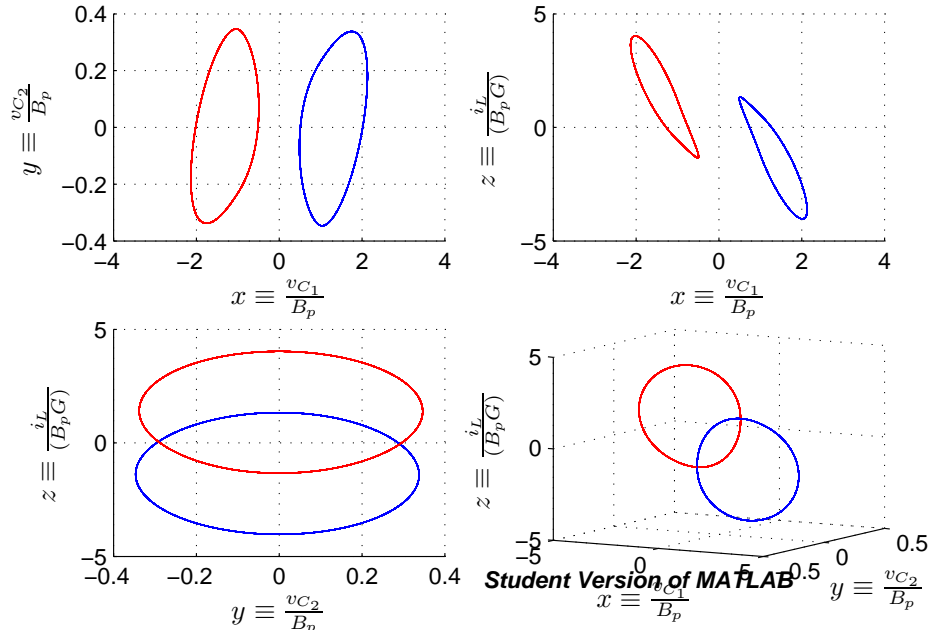


Figure 2: *Limit Cycle*,  $\alpha = 15.6, m_0 = -8/7, m_1 = -5/7, \beta = 45$ , with the blue cycle corresponding to initial value of  $[x_0, y_0, z_0] = [0.7, 0, 0]$  and the red cycle corresponding to initial value of  $[x_0, y_0, z_0] = [0.7, 0, 0]$

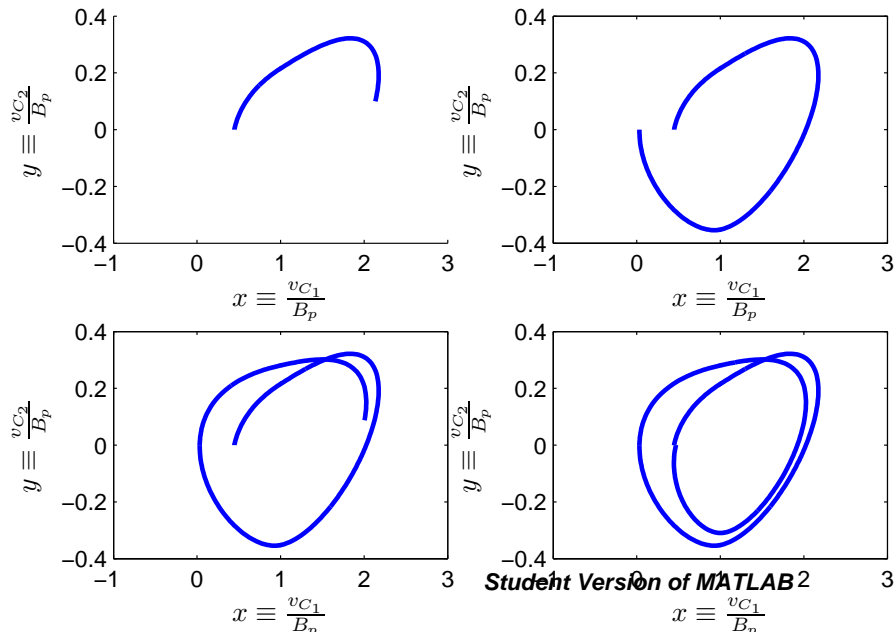


Figure 3: *Period Doubling Process*. The graph shows trajectory in  $v_{C1} - v_{C2}$  section with each subgraph represent  $\frac{1}{4}$  period integration forward. Here,  $\alpha = 15.6, m_0 = -8/7, m_1 = -5/7$  and  $\beta = 35$ .

illustrated by Fig. 4, while  $\beta$  is slightly reduced from  $\beta = 35$ , we can observe successive period-doublings giving rise to period 2, 4, and 8 ... limit cycles. At  $\beta = 32$ , Fig. 5 shows two strange attractors; more specifically, we actually observe the bifurcation of a pair of co-existing one-scroll attractors with separate basins of attraction.

Again slightly reducing  $\beta$ , we observe in Fig. 6 the two attractors moving toward one another until they touch at  $\beta = 31$ , where the twin attractors merge into a single double scroll attractor. Finally Fig. 7 shows the classic Chua's circuit's double-scroll attractor observed at  $\beta = 28$ .

So far the attractors we have plotted are self-excited from unstable equilibria, which allow one to numerically identify and locate them by starting from a point of unstable manifold in the neighborhood of the equilibrium and follow a transient converging trajectory. A hidden attractor, however, has a basin of attraction which does not intersect with any small neighborhoods of equilibria, and therefore cannot be localized through this standard procedure. In 2010, for the first time, Kuznetsov N. discovered a chaotic hidden attractor in Chua's circuit [2]. The dimensionless functions in this paper is more simplified in that  $\dot{z} = -\beta z$  rather than  $\dot{z} = -(\beta y + \gamma z)$  as used in [2]. However, this paper found that by setting  $\gamma = 0$ , there still exists a set of parameters  $\{\alpha, \beta, m_0, m_1\}$  and initial value  $[x(0), y(0), z(0)]$  such that the hidden attractor can be located and identified.

See [2] for the algorithm that uses harmonic linearization and small parameter method to locate initial data in the basin of attraction and then computes the hidden attractors. Let  $u = [x, y, z]$ . For chosen parameters  $\alpha = 8.4568, \beta = 12.0732, m_0 = -0.1768, m_1 = -1.1468$  and coefficient of harmonic linearization  $k = 0.2908$ , the initial data identified is  $u(0) = [9.4287, 0.5945, -13.4705]$ . And for each value of parameter  $\epsilon$ , after the standard transient process governed by the equations below, the computational procedure would reach the starting oscillation  $u(t)$ . Here, the trajectory (with oscillation) associated with the three-dimensional dynamical system satisfies:

$$\frac{dx}{dt} = -\alpha[(m_1 + 1 + k)x + y - \epsilon\phi(x)] \quad (7)$$

$$\frac{dy}{dt} = x - y + z \quad (8)$$

$$\frac{dz}{dt} = -\beta y \quad (9)$$

Sequentially increasing  $\epsilon$  from  $\epsilon_1 = 0.1$  to  $\epsilon_{10} = 1$  with the step size 0.1, the hidden attractor set can be computed. As shown in Fig. 8, with varying  $\epsilon$  values, we are able to obtain the scenario of transition from periodic orbits to hidden chaotic attractors. The final subplot gives the identified hidden attractor. It's interesting to note that the hidden attractor is around the equilibrium zero point. In fact, Fig. 9 supports the claim that this system in the neighborhood of equilibria has three stationary points: the stable zero points and the two symmetric saddles.

## 4 Bifurcation Diagram

The period-doubling bifurcation phenomenon associated with Chua's circuit is also worth noting. We plot  $x$  against  $\alpha$  in the Poincare section where  $y = 0$  and  $\dot{y} < 0$   $\alpha$  with the parameter values  $\beta = 16, m_0 = -8/7$ , and  $m_1 = -5/7$ . According to the graph, the bifurcation points  $\alpha_2$  (where onset of period 2 happens) is indeed around 8.85 and  $\alpha_4$  (where onset of period 4 happens) is around 9.10 as computed in [3] using standard locational stability analysis. Due to the high resolution required, we're not able to clearly plot the bifurcation at onset of period 8; still, we can clearly see the bifurcation route in the diagram Fig. 10.

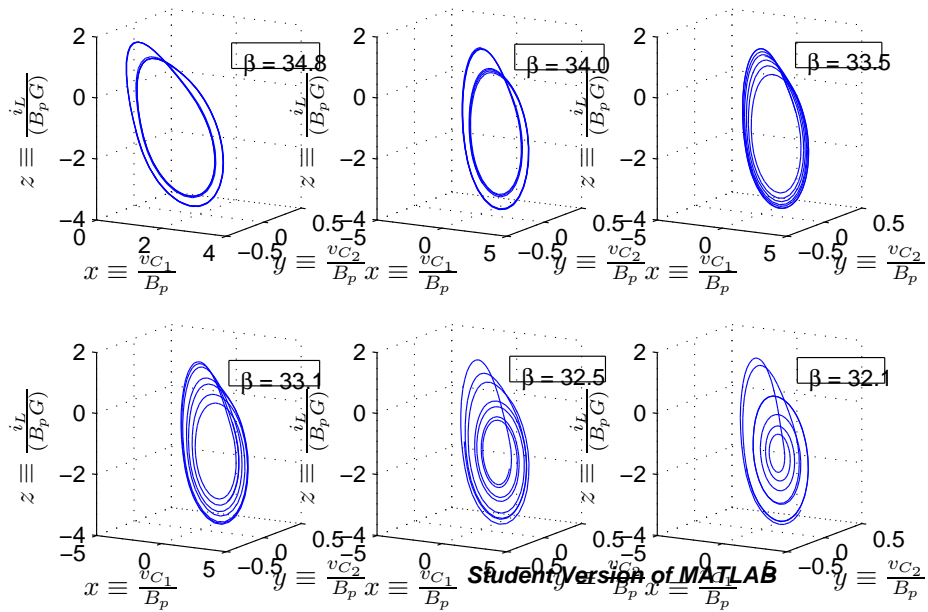


Figure 4: From Period Doubling to Strange Attractors. We fix  $\alpha = 15.6, m_0 = -8/7, m_1 = -5/7$  and vary  $\beta$  from  $35^-$  to  $32^+$ .

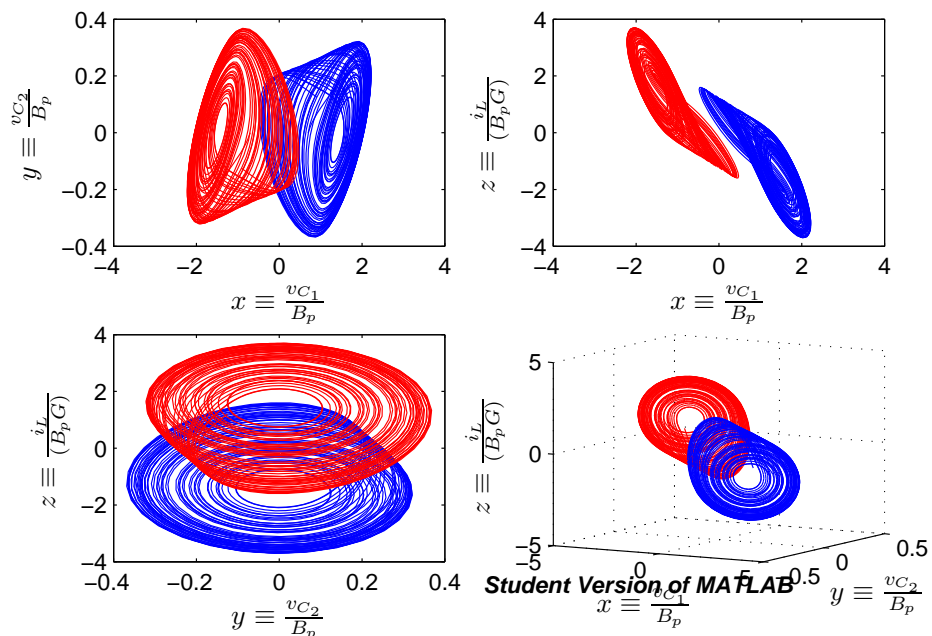


Figure 5: Strange Attractors - One Scroll. Here,  $\alpha = 15.6, m_0 = -8/7, m_1 = -5/7$  and  $\beta = 32$ .

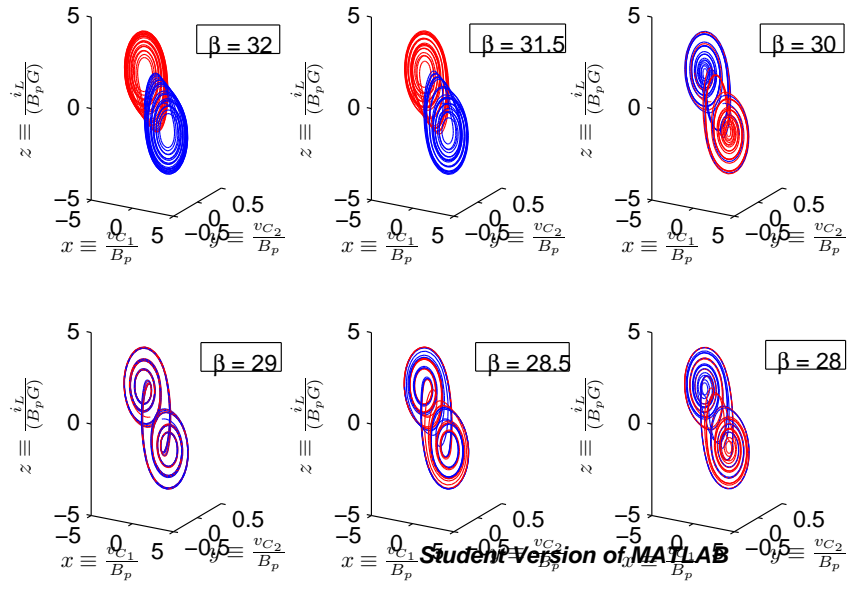


Figure 6: *From Strange Attractors to Double Scroll.* We fix  $\alpha = 15.6, m_0 = -8/7, m_1 = -5/7$  and vary  $\beta$  from  $32^-$  to  $28^+$ .

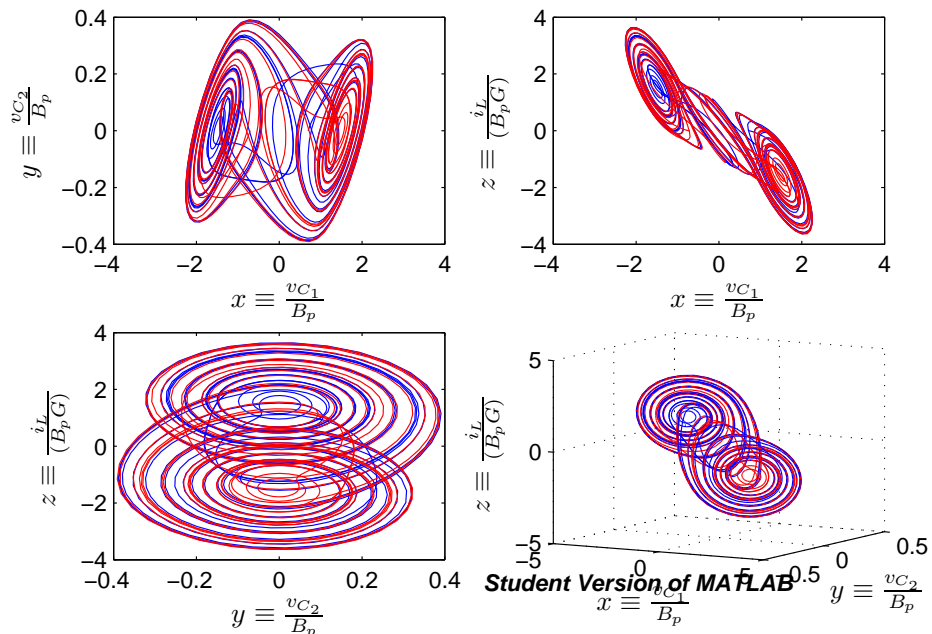


Figure 7: *Double Scroll Attractor.* Here,  $\alpha = 15.6, m_0 = -8/7, m_1 = -5/7$  and  $\beta = 28$ .

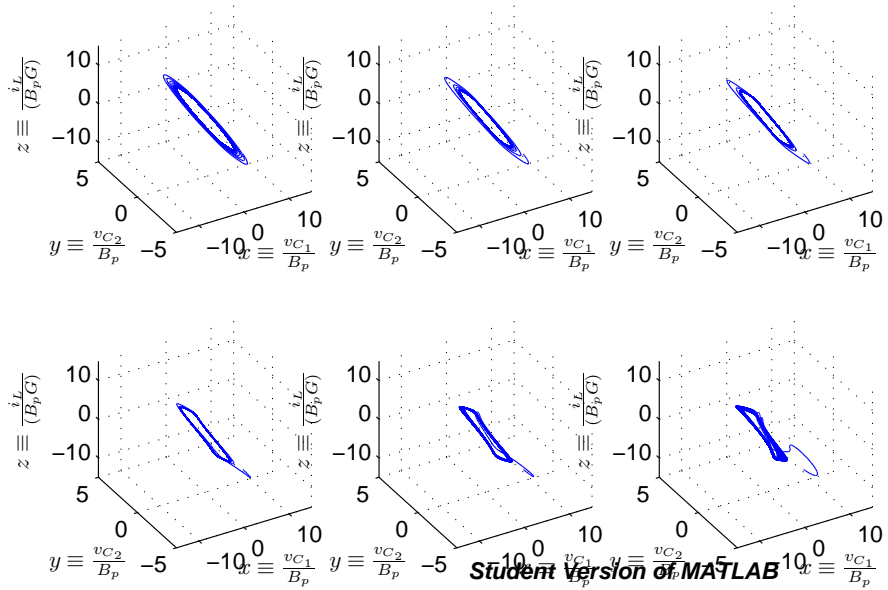


Figure 8: *From Periodic Orbit to Hidden Chaotic Attractor*, with  $\alpha = 8.4568, \beta = 12.0732, m_0 = -0.1768, m_1 = -1.1468, k = 0.2908$  and the initial data  $u(0) = [9.4287, 0.5945, -13.4705]$ .  $\epsilon$  is varied from 0.1 to 1.0 with step size 0.1.

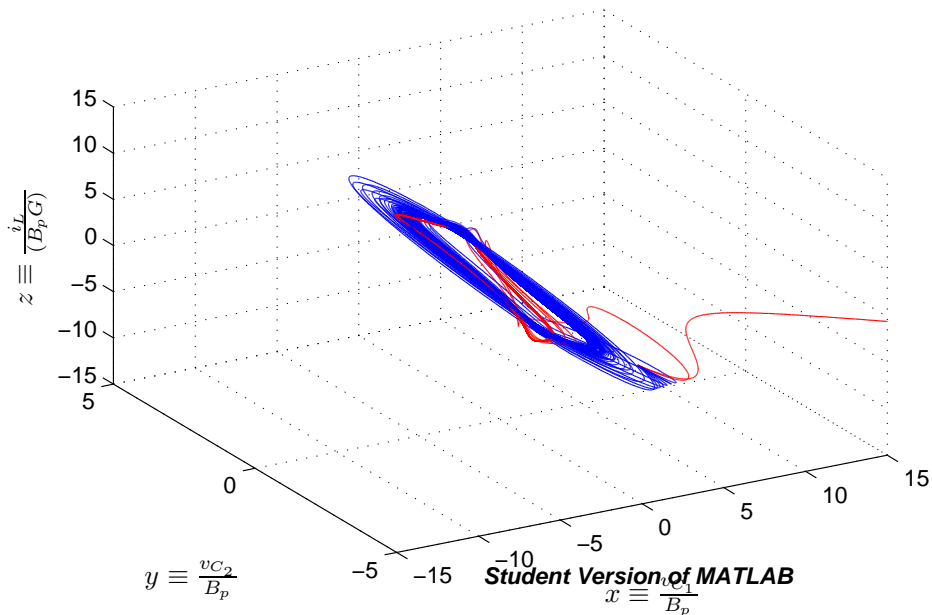


Figure 9: *Hidden Attractor*, with  $\alpha = 8.4568, \beta = 12.0732, m_0 = -0.1768, m_1 = -1.1468, k = 0.2908$  and the initial data  $u(0) = [9.4287, 0.5945, -13.4705]$ . The blue region represents the hidden attractor, and the red manifolds represent other parts of the trajectories of system.

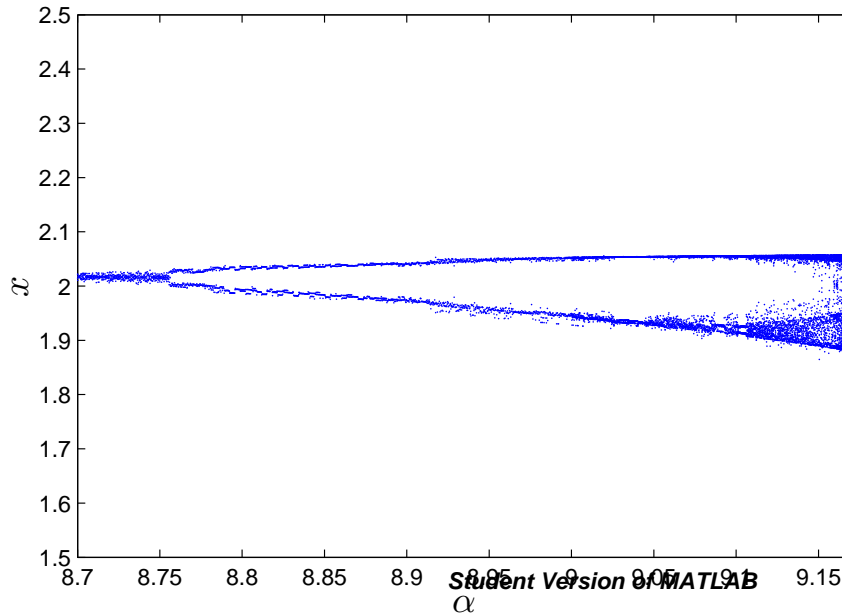


Figure 10: *Bifurcation Diagram for Period Doubling in Chua's Circuit.* A *poincare section* plots  $x$  when  $y = 0$  and  $\dot{y} < 0$ , with  $\beta = 16$ ,  $m_0 = -8/7$ , and  $m_1 = -5/7$

## 5 Conclusion and Discussion

This paper has studied Chua's circuit's classic chaotic behaviors by plotting the chaotic attractors, which include the one-scroll, double-scroll and hidden attractors, and the period-doubling bifurcation diagram.

Through trying out alternative Poincare sections or parameter sets, the bifurcation diagram might be improved to clearly plot more bifurcation points. There are many interesting properties of Chua's circuit to explore; for example, the 3-scroll attractor (and even n-scroll ones) generated from generalized Chua's circuit, and the possible hidden basins of attractions for these generalized forms.

## References

- [1] L. Gmez-Guzmn *et al*, "Synchronization of Chuas circuits with multi-scroll attractors," *Communications in Nonlinear Science and Numerical Simulation*, Volume 14, Issue 6, pp. 2765–2775, 2009.
- [2] Kuznetsov N., Kuznetsova O., Leonov G., Vagaitsev V, "Analytical-numerical method for attractor localization of generalized Chua's system," *Periodic Control System*, Volume 4, pp. 29–33, 2010.
- [3] L. O. Chua and L. T. Huynh, "Bifurcation analysis of Chua's circuit," *Circuits and Systems*, pp. 746–751, 1992.

# Investigating the Henon Map

*Shreyas Kumar*

**Abstract:** Through a numerical investigation of the Henon map, we discover many interesting chaotic phenomena. We analytically identify two fixed points, which determine the range of investigation of one of the parameters. We then use bifurcation diagrams to explore the period doubling nature of the map; one interesting feature that arises is the presence of spontaneous, unconnected, satellite branches that are very similar to the bifurcation diagram of the logistic map. We then compute the strange attractor of the Henon map with the classical parameter values of  $a = 1.4$  and  $b = 0.3$ . The correlation dimension of this attractor is computed to be 1.214.

## 1 History

The Henon map is a discrete time dynamical system that was first introduced by Michel Henon, a French mathematician and astronomer, in his 1976 paper 'A Two Dimensional Map with a Strange attractor' [1]. The Henon map is a model of the Poincare section of the Lorenz equations. The Lorenz equations are of interest because they describe flow in three dimensions [6]. However, this is a very complex system which requires substantial computational time; the Henon map simplifies this system while retaining some interesting chaotic properties. Performing a Poincare section on the Lorenz system simplifies it considerably but the new system still requires you to solve differential equations. Henon simplified this further by defining a two dimensional map that was inspired by Poincaré's results [1]. While the Henon map is not related physically to the flow model that the Lorenz equations describe, it still retains the important mathematical properties that can be studied [2].

## 2 Definition of the Map

The Henon map belongs to the class of dissipative quadratic maps. It maps the plane back to itself. There are two free parameters -  $a$  and  $b$ . The map  $\mathcal{T} : \mathbb{R}^2 \rightarrow \mathbb{R}^2$  is defined as follows [4]:

$$\begin{aligned}x_{n+1} &= y_n + 1 - ax_n^2, \\y_{n+1} &= bx_n.\end{aligned}\tag{1}$$

With an appropriate choice of  $a$  and  $b$ , this map becomes chaotic. Henon established reasonable values for  $a$  and  $b$ . When creating the map, he stipulated that  $b$  should be less than 1 in absolute value [1]. This map is sensitive to the parameter values. This is demonstrated by the evolution of the origin for two different choices of  $a$  and  $b$  in Figure 1.

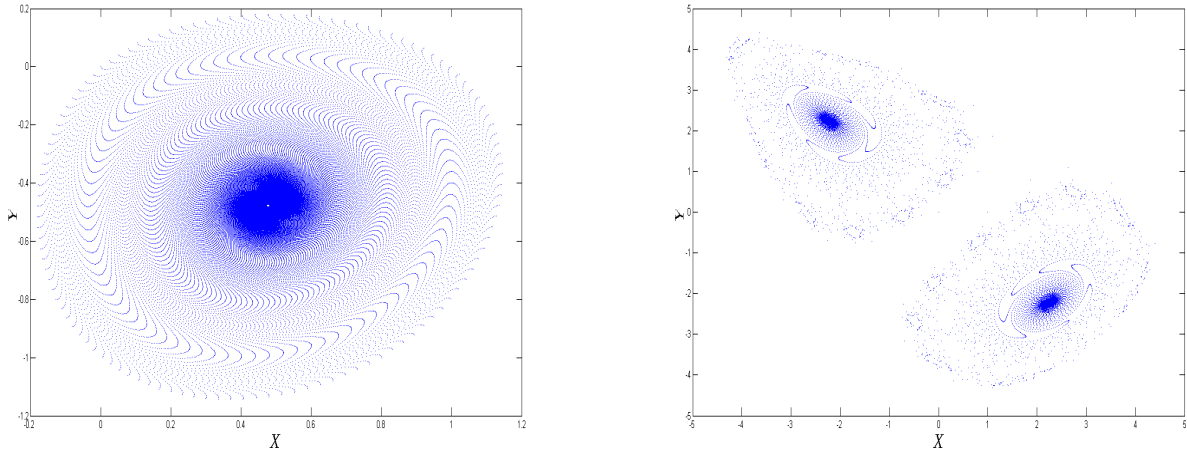


Figure 1: Evolution of the origin for two different values of  $a$  and  $b$ . (a)  $a = 0.2$ ,  $b = -0.9999$ ; (b)  $a = 0.2$ ,  $b = 0.9991$ .

### 3 Analytical work

#### 3.1 Fixed Points

First we identify the fixed points in our map. A fixed point  $(x^*, y^*)$  satisfies

$$\begin{aligned} x^* &= 1 + y^* - ax^{*2}, \\ y^* &= bx^*. \end{aligned} \quad (2)$$

We substitute for  $y^*$  in the equation for  $x^*$  to get

$$x^* = 1 + bx^* - ax^{*2}. \quad (3)$$

We can solve this using the quadratic formula to find the two fixed points

$$\begin{aligned} x^* &= \frac{(b-1) \pm \sqrt{(b-1)^2 + 4a}}{2a}, \\ y^* &= bx^*. \end{aligned} \quad (4)$$

Since the range for the Henon map is  $\mathbb{R}^2$ , the fixed points exist only when  $x^*$  and  $y^*$  are real. This condition is satisfied when

$$(b-1)^2 + 4a > 0,$$

or

$$a > \frac{(1-b)^2}{4}. \quad (5)$$

#### 3.2 The Jacobian

The Jacobian of the system is of interest because its determinant tells us the rate at which the map expands or contracts per iteration. The Jacobian matrix is defined by

$$J = \begin{bmatrix} \partial x_{n+1}/\partial x_n & \partial y_{n+1}/\partial x_n \\ \partial x_{n+1}/\partial y_n & \partial y_{n+1}/\partial y_n \end{bmatrix}.$$

Calculating the partial derivatives,

$$J = \begin{bmatrix} 2x & b \\ 1 & 0 \end{bmatrix}.$$

Hence  $\det(J) = -b$ . As  $|-b| < 1$ , the map is a contracting map [5]. This was why Henon stipulated that  $|b| < 1$  when he defined the map.

## 4 Results and Discussion

### 4.1 Bifurcations

A standard method of investigating a chaotic system is to compute a bifurcation diagram. A bifurcation diagram essentially helps identify stable cycles that are present in the map. Hence a single line in a bifurcation diagram implies a fixed point. When it splits for the first time, the system is in a period 2 regime. This implies that  $\mathcal{T}(x) = x'$  and  $\mathcal{T}(x') = x$ . When a system displays chaos, a bifurcation diagram will be 'coloured in' for the chaotic region. In other words, there is no stable cycle; in other words for all  $i \in \mathbb{N}$  there exists a  $j \in \mathbb{N}$  such that  $x_{j+i} \neq x_j$ . In this paper I will use bifurcation diagrams to study the behavior of the system for a range of values of the parameter  $a$ . Henon analytically showed that if  $a < (1 - b)^2/4 = 0.1225$  (for  $b = 0.3$ ) the fixed points do not exist (see equation 5) and if  $a > 1.55$  (for  $b = 0.3$ ) the iterates diverge to infinity [1]. The bifurcation diagram for the range  $0 < a < 1.5$  is presented in Figure 2. The initial conditions were chosen arbitrarily to be the point  $(0.5, 0)$ . The first 10,000 iterates were not used; this was to ensure that the points had converged to a periodic solution if one existed.

Clearly the most interesting region is where  $1 < a < 1.45$  as this is where the chaos lies (see Figure 3). We see a very interesting phenomenon, namely the satellite regions that emerge around  $a = 1.075$ . These are branches of the bifurcation diagram that are spontaneously emerging; i.e. they are not connected to the regions for greater or smaller values of  $a$ . So at around  $a = 1.06$  we see that the system moves from a chaotic regime to period 6 cycle. Note that this is a distinctly different transition than at  $a = 1.225$  where a 7-cycle emerges from the chaotic region. Figure 4 shows one of these satellite regions in greater detail. Surprisingly this part resembles the bifurcation diagram of the logistic map. The 6-cycle for  $a = 1.067$  is presented in Table 1; in this region the map jumps from satellite to satellite (in the same order), visiting each one every 6 iterations. The satellites are numbered from 1-6 going from the top to bottom.

$x$	$y$	satellite
1.0591	0.1027	2
-0.0942	0.3177	5
1.3083	-0.0283	1
-0.8545	-0.3925	6
-0.2563	0.6134	3
0.3422	0.1840	4
1.0591	0.1027	2

Table 1: 6-cycle for  $a = 1.067$  with the satellites numbered from top to bottom

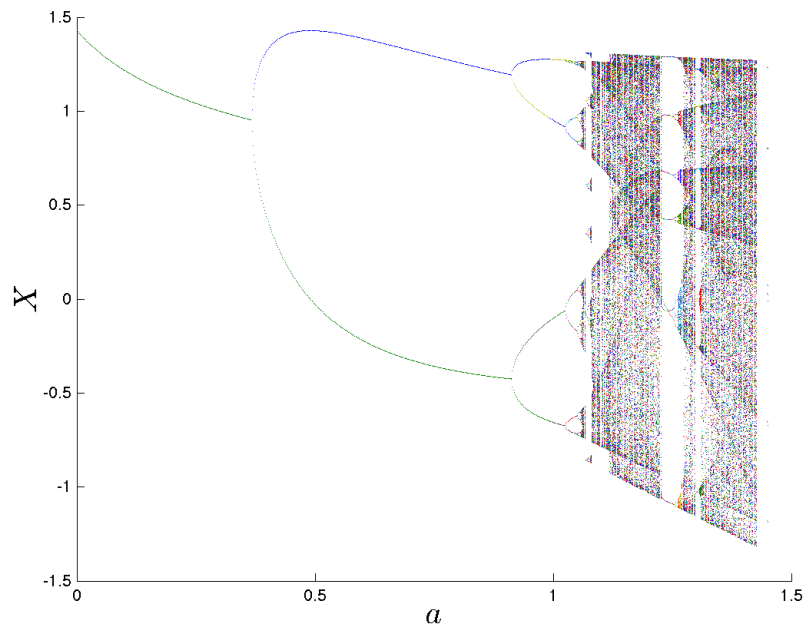


Figure 2: Bifurcation diagram for  $0 < a < 1.5$

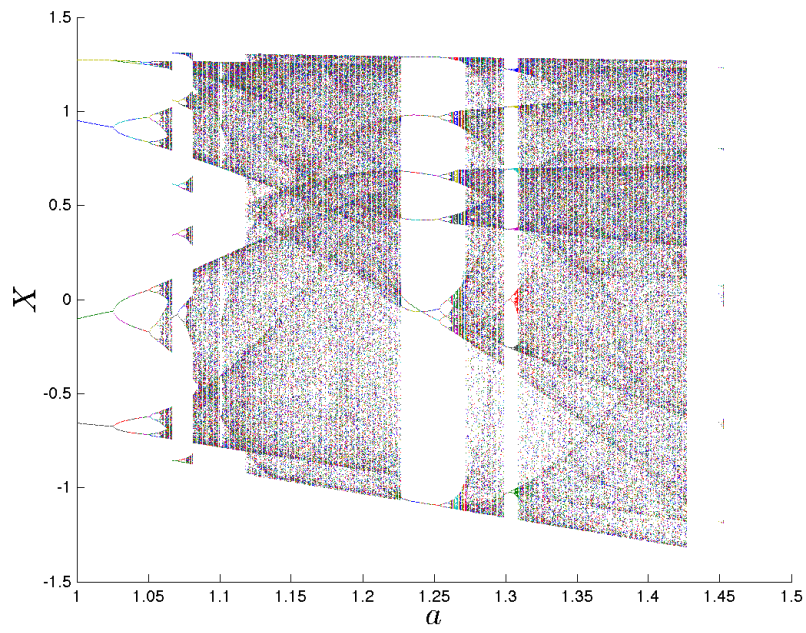


Figure 3: Bifurcation diagram for  $1 < a < 1.5$

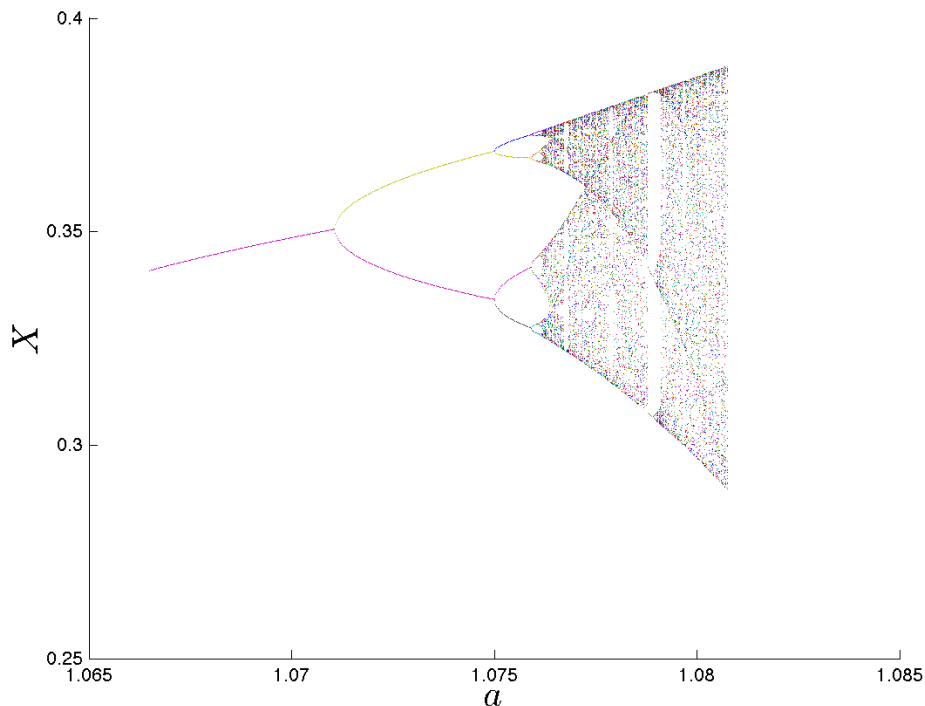


Figure 4: Spontaneous satellite that is similar to the logistic bifurcation diagram. This is satellite 6; it is visited every 6 iterations

## 4.2 Strange attractor

The Henon map is known to have a strange attractor for the values  $a = 1.4$  and  $b = 0.3$ . These are the values initially studied by Henon in 1976 [1]. This attractor has a rich structure as it has a non-integer correlation dimension. One end of the attractor is smooth while the other end is a Cantor set, which is one of the classical fractals [4]. Thus, this attractor aptly demonstrated the chaotic nature of this map. It is important to note that the attractor has the most complex structure when  $a = 1.4$ . At other values, the attractor is either not present (points diverge to infinity) or is partially formed as seen in Figure 5. In order to emphasize the finer structure of the attractor, a zoomed in plot which corresponds to the rectangle on the entire attractor (see Figure 6) is presented in Figure 7. The Cantor set nature of the attractor is visible as the attractor is not continuous there. Note that the two fixed points as determined in Section 3.1 are  $(0.631, 0.189)$  and  $(-1.13, -0.339)$ . The first of these fixed points lies in the region of the attractor.

## 4.3 Fractal dimensions

Since the strange attractor of the Henon map is fractal in nature, the logical next step is to calculate the fractal dimension. The fractal dimension or correlation dimension of a set is defined using a correlation integral  $C(r)$  [3].

$$C(r) = \lim_{N \rightarrow \infty} \frac{2}{N(N-1)} \cdot (\text{number of distinct distances } r_{i,j} \text{ which are less than } r.) \quad (6)$$

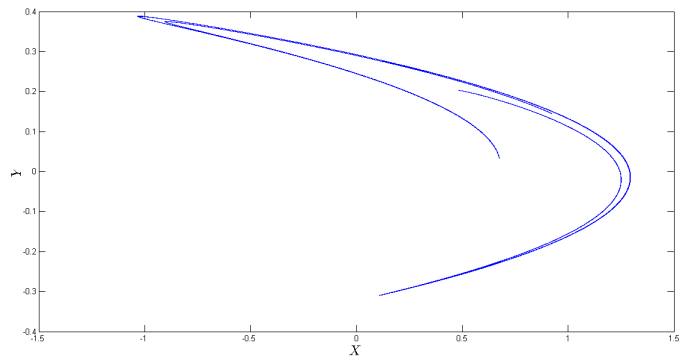


Figure 5: Half formed attractor for  $a = 1.2$ ,  $b = 0.3$

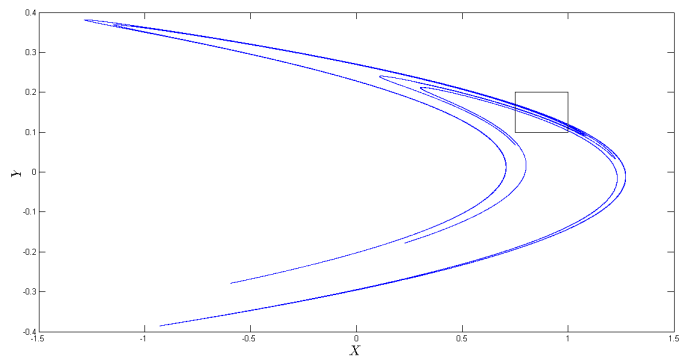


Figure 6: Classical Henon attractor for  $a = 1.4$ ,  $b = 0.3$

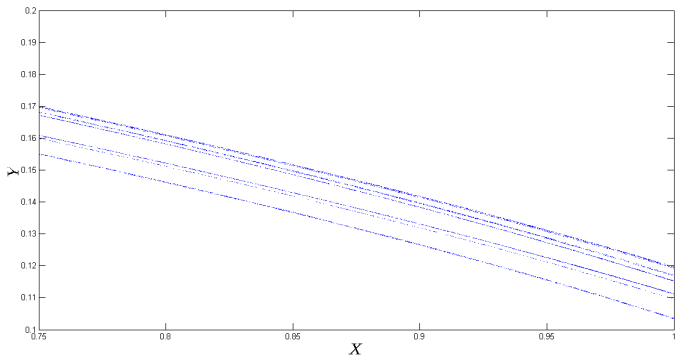


Figure 7: Fractal structure of the attractor

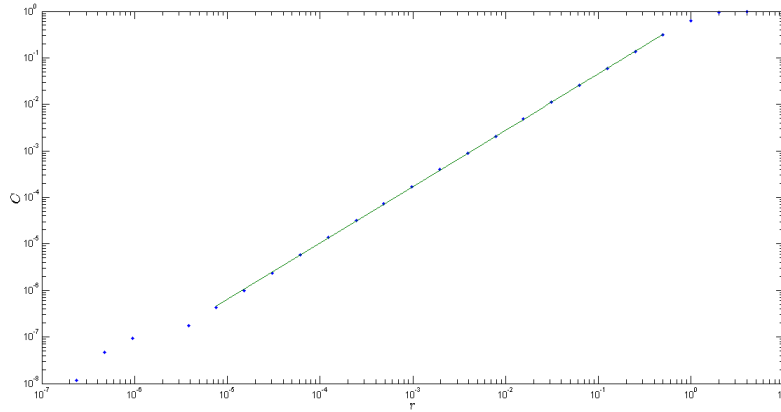


Figure 8: Identifying the Correlation Dimension

Note that in the above definition  $r_{i,j}$  refers to a pairwise distance between two elements of the given set. If  $C(r) \propto r^D$  for a wide range of  $r$  and large  $N$  then  $D$  is considered to be the fractal dimension of the set.

In our case  $N$  is the number of points we used to generate the attractor. In this computation,  $N$  was 13,000; this value was chosen to ensure a feasible computation of the distances. Hence, we plot  $C(r)$  against  $r$  in a log-log plot. In the region where the points lie on a line we perform a regression fit. The slope of this line is then the fractal dimension of the attractor. I determined that the fractal dimension was 1.214; this just outside the range quoted in literature of  $1.25 \pm 0.02$  [4]. This discrepancy is probably because only 13,000 points were used.

## 5 Further Work

The computations we performed illustrate the chaotic nature of the Henon map. However, a more accurate calculation of the fractal dimension of the attractor is possible. Another computation that would provide insight is a basin of attraction. This would tell us which initial conditions converge to the attractor. We could also consider extensions of the Henon map, and consider how the attractor and the fractal dimension change. More analytical work could also be done; specifically, we can calculate the Lyapunov exponent.

### Acknowledgments:

I would like to thank Professor Jeffrey Chasnov for advice on the paper as well as for the code to calculate the correlation dimension.

### References:

1. Henon, Michel. *A Two Dimensional Mapping with a Strange Attractor*. Communications in Mathematical Physics. Vol. 50 (1976), pp. 69-77.
2. Benedicks, Michael and Carleson, Lennart. *The Dynamics of the Henon Map*. Annals of Mathematics. Second Series, Vol. 133, No. 1 (Jan., 1991), pp. 73-169.

3. Grassberger, Peter and Procaccia, Itamar. *Characterization of Strange Attractors*. Phys. Rev. Lett. 50 (1983), pp 346-349. [/math164/scientific-computing.pdf](#). pp. 87-94, 103-110
4. Wolfram Research. <http://mathworld.wolfram.com/HenonMap.html>.
5. Demidov, Evgeny. *E-Notes*. <http://www.ibiblio.org/e-notes/Chaos/henon.htm>
6. McGehee. <http://www.math.umn.edu/mcgehee/Seminars/ClimateChange/presentations/20081007.pdf>
7. Chasnov, Jeffrey. *Scientific Computing*. (2013). <http://www.math.hmc.edu>

# Quadratic Julia Sets and the Mandelbrot Set

Jason Wang

**Abstract:** When creating mathematical models, it is important to note where they are safe to use and when they behave unpredictably. In this paper, we will define both Julia Sets and the Mandelbrot Set, explain how they relate to the stability of a quadratic polynomial, and describe the techniques used to visualize them via plots. We will also explore the relationship between the Mandelbrot Set and quadratic Julia Sets.

## 1 Introduction

Gaston Julia (1893-1978) was a French mathematician best known for his research of iterated functions. His article *Mmoire sur l'iteration des fonctions rationnelles*, or “On the Iteration of Rational Functions,” explored how functions behaved when iterated, or composed with itself multiple times. Specifically, he studied the orbits of a complex number  $z_0$  under a function  $R(z)$ , which is the set  $\{z_0, R(z_0), R^2(z_0), \dots\}$ , and when orbits would converge to a certain value or become trapped in a cycle that does not converge. He determined that when an orbit of some point converges to a certain value (or infinity), the function behaves predictably at that point. Nonconvergence would then suggest chaotic behavior. Julia Sets are the points that have nonconverging orbits.[4]

While Julia provided the mathematical framework for Julia Sets, the absence of computing power in his time meant that visualizing the sets required calculating and plotting by hand. This process was tedious and impractical, so his work had very few numerical and visual results. Julia’s work was largely forgotten until the emergence of powerful computers in the latter 1900s. Computers made it possible to perform iterations quickly and plot millions of data points in a reasonable time, and the world was finally able to view the often beautiful graphical representations of Julia Sets.[2]

Around the same time when Julia was most active, his contemporary, Pierre Fatou, provided a different perspective on iterated functions. Specifically, he explored the iterative properties of the function  $R(z) = z^2 + c$ , a class of functions that Julia had also analyzed. Instead of varying the initial value  $z_0$ , Fatou used points on the complex plane as values of  $c$  and iterated from  $z_0 = 0$ . He focused on how quickly (the number of iterations) it took for the iterative sequence to tend toward infinity (if at all). The set of  $c$  values whose orbits do not tend to infinity suggest chaotic behavior. Again, the lack of computing resources meant that Fatou was never able to view a complete graphical representation of his work. In the 1970s, Benoit Mandelbrot, a researcher at IBM, used computers to calculate and represent Fatou’s work with a plot. The set of  $c$  such that orbits of 0 do not tend to infinity is now called the Mandelbrot Set.[6]

## 2 Theoretical Background

### 2.1 Julia Sets

First, we define a *rational function* as any function from the complex space  $\mathbb{C}$  to itself that can be represented as a ratio of two polynomial functions in lowest terms. Let  $R(z)$  be a rational function.

Let

$$R(z) = P(z)/Q(z) = \frac{a_0z^d + \dots + a_d}{b_0z^{d'} + \dots + b_{d'}}, Q(z) \neq 0$$

and let

$$R^n(z) = R \circ R \circ \dots \circ R(z) \quad (n \text{ times})$$

We call this the  $n$ -th iteration of  $R(z)$ .

For  $k = 1, 2, \dots$  consider  $R^k$  and its fixed points. Recall that a fixed point of a function  $f(x)$  is a point  $p$  such that  $f(p) = p$ . The fixed points of  $R^k$  are called periodic points of period  $k$ .

Next, consider a periodic point  $z$  of period  $k$ . A fixed point can be stable or unstable. If  $z$  is stable, then nearby points will converge to  $z$  as we iterate  $R$  on them. If  $z$  is unstable, then nearby points will not converge to  $z$  as we iterate  $R$ . This instability indicates chaotic behavior of  $R$ .

A Julia set is the set of all unstable, or “repelling,” periodic points.

## 2.2 The Mandelbrot Set

The Mandelbrot Set is formally defined as

$$M = \{p \in \mathbb{C} \mid p, p^2 + p, (p^2 + p)^2, \dots \not\rightarrow \infty\}$$

We can view  $M$  as the set of all complex numbers  $z = x + iy$  for which the orbit of  $z_0 = 0$  converges when  $R(z) = z^2 + p$ . [1]

## 2.3 Relationship Between the Mandelbrot and Julia Sets

Consider the Julia Sets of quadratic functions of form  $R(z) = z^2 + c$ . We see that the Mandelbrot Set and quadratic Julia Sets are all created using same type of function. While we vary  $z_0$  and keep  $c$  constant for a Julia Set, we vary  $c$  when making the Mandelbrot Set. The Mandelbrot Set can be used to predict the shapes of certain Julia Sets if we let each point  $c$  in the complex plane can be mapped to the Julia Set for the function  $R(z) = z^2 + c$ . [5]

# 3 Numerical Methods

## 3.1 Julia Sets

To visualize the Julia Set of a function  $R(z)$ , we can color each point  $z = x + iy$  in the complex plane according to the magnitude of its convergence point. Since there are infinitely many convergence points, we limit the number of colors to 15.

In our plotting algorithm, we set an iteration limit (**it**) and a divergence threshold (**thresh**). For each point  $p = x + iy$  in the complex plane, we iterate  $R$  with  $z_0 = p$  until it either passes the threshold or the iteration limit is up. Iterating  $R$  with  $z_0$  refers to sequentially calculating  $R(z_0), R(R(z_0)), \dots$ . Once the output passes **thresh**, we can assume that the orbit tends to infinity and can color the point with a background color. [3] If we reach the iteration limit, we color according to **floor(mod(val\*15,15))+1**, where **val** is the magnitude of the **it**-th iteration.

### 3.2 The Mandelbrot Set

To plot the Mandelbrot Set, we set an iteration limit **it** and threshold **thresh** for the magnitude of the output. For each point on the complex plane, we start at  $z = 0$  and find the number of iterations it takes until **thresh** is reached (with maximum of **it**). We then color each point based on its respective number of iterations.[3] To plot Figure 5, we use **thresh** = 120 and **it** = 128. For number of iterations **n**, we color the point with an rgb value of  $(255-n, 255-n, 255-n)$  to achieve a nice gradient with various shades of gray. Remember that  $(0,0,0)$  gives us black, and  $(255,255,255)$  gives us white.

## 4 Results

A popular class of functions that has interesting Julia Sets is of the form  $R(z) = z^2 + c$ , where  $c \in \mathbb{C}$ . Different values of  $c$  will give us Julia Sets that look quite differently. Figures 1, 2, and 3 show Julia Sets for three different values of  $c$ . We use **it** = 28 and **thresh** = 2.

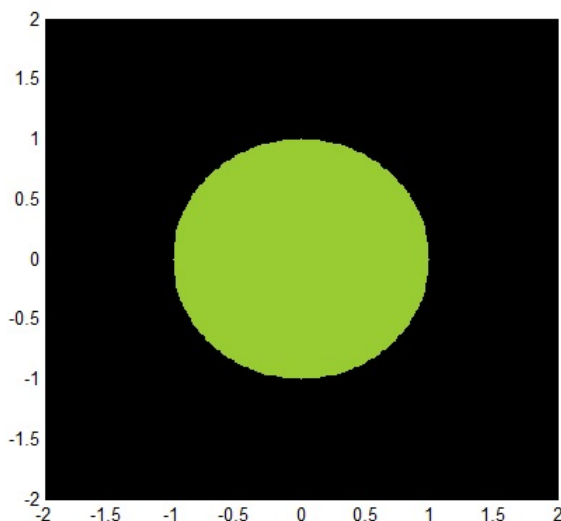


Figure 1:  $c = 0$

In Figure 1, the Julia Set is the unit circle. It is straightforward to show this analytically. Let  $R(z) = z^2$ , which has the same magnitude as  $|z|^2$ . We see that  $R^k(z) = z^{2^k}$ . Suppose  $|z| < 1$ . Then  $\lim_{k \rightarrow \infty} z^{2^k} = 0$ . Now, suppose  $|z| > 1$ . Then  $\left| \lim_{k \rightarrow \infty} z^{2^k} \right| = \infty$ . If  $|z| = 1$ , then  $z$  is a point on the unit circle, and  $\left| \lim_{k \rightarrow \infty} z^{2^k} \right| = 1$ . If  $z$  is an  $n$ -th root of unity, then iterating  $R$  will cycle among  $n$  different values.

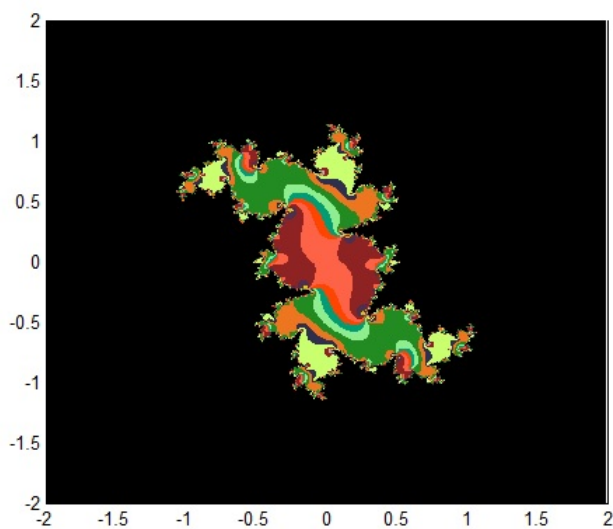


Figure 2:  $c = 0.238498 + i0.519198$

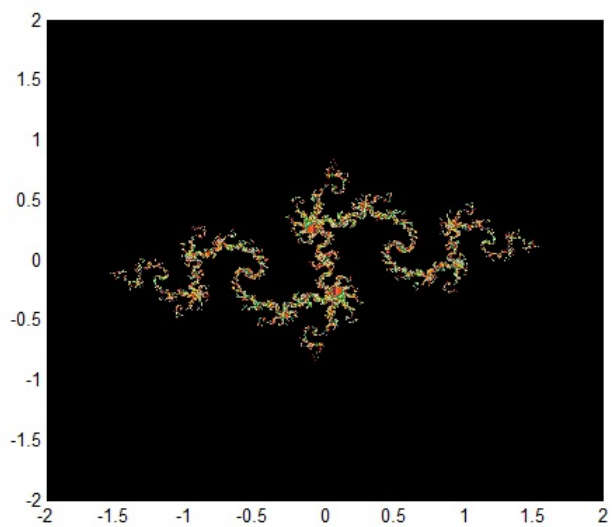


Figure 3:  $c = -0.835 - i0.2321$

While Figure 1 looks uninteresting, Figures 2 and 3 look like fractals. The Julia Set in each plot is roughly all points at which the color changes. We zoom into Figure 2 to see some self-similarity.

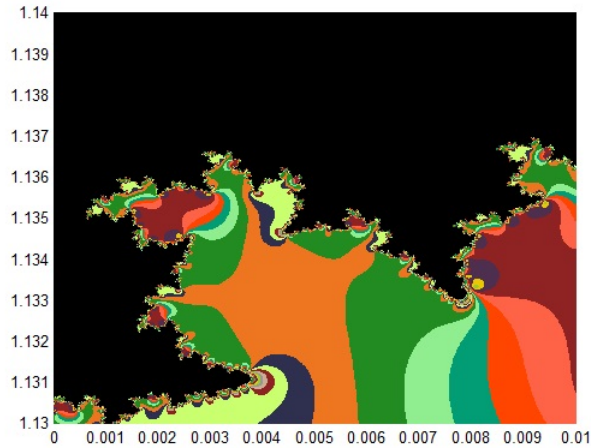


Figure 4: Zoomed-in portion of Figure 2

The Mandelbrot Set also uses quadratic functions of the form  $R(z) = z^2 + c$ . This suggests that the Mandelbrot Set is related to the quadratic Julia Sets in a nontrivial way.

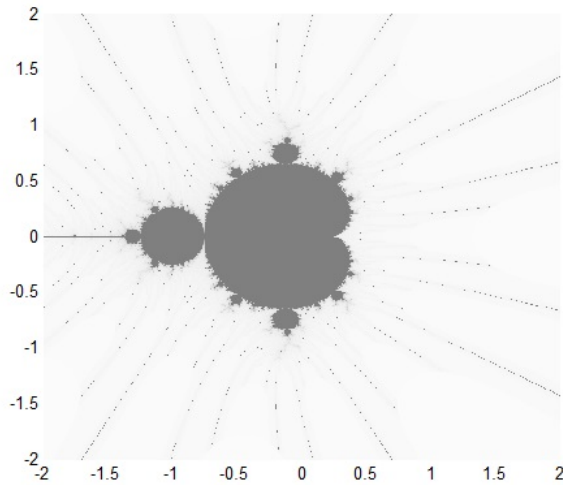


Figure 5: The Mandelbrot Set

We see that the Mandelbrot Set  $M$  is roughly the set of all gray points. It turns out that to find an interesting value of  $c$  to use for a quadratic Julia Set, we just need to pick a point along the boundaries of  $M$ . Below, we see a zoomed-in portion of the Mandelbrot Set. We see that the  $c$  values for Figure 1 and Figure 2 are near the border.

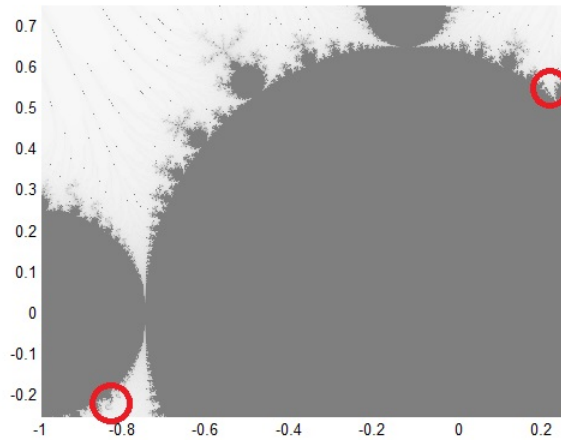


Figure 6:  $c = 0.238498 + i0.519198$  and  $c = -0.835 - i0.2321$  are circled in red.

Now, let us compare the Julia Set fractal in Figure 2 to the following zoomed-in portion of the Mandelbrot Set (around  $c = 0.238498 + i0.519198$ ).

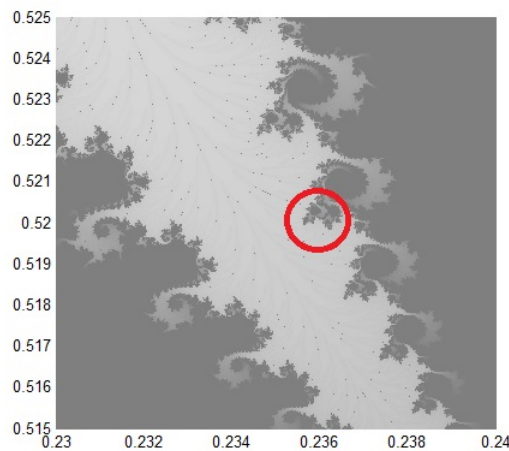


Figure 7: The circled shape resembles the shape of the Julia Set in Figure 2.

## 5 Discussion

Using iterative methods, we are able to compute and plot the Mandelbrot Set, as well as Julia Sets of quadratic polynomials  $R(z) = z^2 + c$ . Using coloring schemes, we can visualize the behavior of the functions as they are iterated. With Julia sets, we see a function's iterative behavior with respect to different starting points  $z_0$ . The Mandelbrot Set, which uses the same class of functions, lets us see how varying the constant  $c$  changes the behavior of the Julia Set for its respective quadratic polynomial. When comparing the shape of a Julia Set with parameter  $c$  and the zoomed-in portion of the Mandelbrot Set around  $c$ , we can see that they are similar, and the latter can often be easily used predict the shape of the former.

Future work on the relationship between Julia Sets and the Mandelbrot Set should include more examples comparing the shape of the Julia Set of  $R(z) = z^2 + c$  and the Mandelbrot Set zoomed-in around the complex number  $c$ . We can also find the relationship between Julia Sets of higher degree polynomials and Multibrot Sets, which are a generalization of Mandelbrot Set for higher degree polynomials. The plotting algorithm and coloring strategies can also be improved to allow for better precision.

## References

- [1] L. Keen, *Julia Sets of Rational Maps*, Proceedings of Symposia in Applied Mathematics **49** (1994), 71–77.
- [2] C.R. Spitznagel, *Vignette 15: Julia Sets*, accessed Apr. 14, 2013, [www.jcu.edu/math/Vignettes/Julia.htm](http://www.jcu.edu/math/Vignettes/Julia.htm)
- [3] R.T. Stevens, *Creating Fractals*, Charles River Media, Inc., Hingham, MA, 2005, pp. 183–199.
- [4] *Julia sets*, Wikipedia: The Free Encyclopedia, accessed Apr. 14, 2013, [en.wikipedia.org/wiki/Julia\\_set](http://en.wikipedia.org/wiki/Julia_set)
- [5] *Mandelbrot set*, Wikipedia: The Free Encyclopedia, accessed Apr. 14, 2013, [en.wikipedia.org/wiki/Mandelbrot\\_set](http://en.wikipedia.org/wiki/Mandelbrot_set)
- [6] *Mandelbrot set*, accessed Apr. 14, 2013, [www.wordiq.com/definition/Mandelbrot\\_set](http://www.wordiq.com/definition/Mandelbrot_set)

# Rendering L-Systems via Chaos Games

*John Wentworth*

## Abstract

We present equations to convert an L-system to a classical fractal. These equations are then used to render the L-system using a chaos game. A sample walkthrough of the algorithm is supplied, followed by sample renderings. The method is able to generate realistic images of trees.

## 1 Introduction

L-systems are a class of classical fractals widely used for modelling the geometry of plants. Formally, an L-system is a geometric rewriting system, a type of formal grammar. Colloquially, L-system usually refers to a grammar which begins with a single line. The rewriting rules then add new lines, or “branches,” connected to the original line, or “trunk.” Figure 1 shows a simple example of an L-system.

More complicated and even randomized L-systems can generate highly realistic images of plants, especially trees. They are widely used for generating plants for graphics applications, such as CGI for movies and video games.

Though L-systems can produce highly realistic trees, they can be slow. Like most fractals, the speed of rendering an L-system is limited by the large number of very small components. For L-systems, the number of terminal branches in the tree grows exponentially in the number of iterations used. L-system rendering thus requires drawing large numbers of very small branches.

L-systems are generally rendered using a turtle graphics system. Turtle graphics emulate a pencil or pen using a “turtle.” The turtle is able to turn and move forward. Whenever the turtle moves forward, it draws a line as it moves. L-systems are typically represented as a grammar which generates instructions for the turtle graphics system. Unlike typical grammars, a L-system applies all applicable replacement rules in parallel at every step. This allows them to simulate plants, which grow many branches simultaneously.

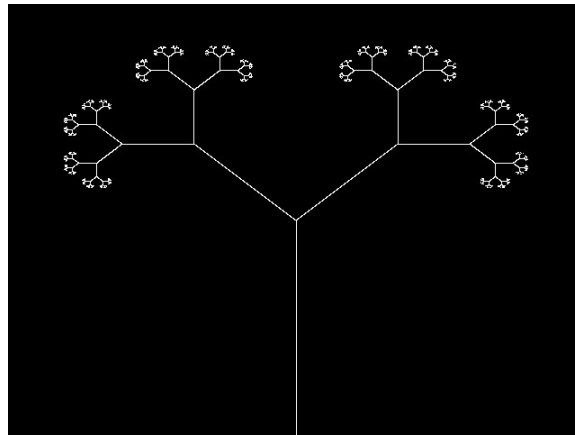


Figure 1: A simple L-system.

A more efficient method often used for rendering classical fractals is the chaos game method. Chaos games are an iterative method which perform a randomly chosen transformation on a point at each iteration. At each iteration, the point is plotted before the next transformation. The result is a discrete time stochastic dynamical system. As long as the state of the chaos game is bounded, the attractor will be a classical fractal. Because the method is randomized, the attractor is often sampled more uniformly with a smaller number of points than deterministic methods, allowing fast rendering. By using the right set of possible transformations, any classical fractal can be rendered.

This paper explores the possibility of using chaos games to render L-systems, providing a potentially fast method for generating images of plants.

## 2 Governing Equations

A classical fractal is defined by a domain  $\Omega$ , often chosen to be the unit square, and a set of transformations  $\{T_i : \Omega \rightarrow \Omega | i = 1, \dots, N\}$ , usually chosen to be affine. The fractal is the set  $U \subset \Omega$  which satisfies

$$U = \cup_i T_i U \quad (1)$$

For generic classical fractals, the set  $U$  is typically found iteratively. One begins with a set  $V_0 = \Omega$  and iteratively calculates the union of images of  $V_n$  under the transformations, or  $V_{n+1} = \cup_i T_i V_n$ . The fractal  $U$  is then the limiting set  $U = \lim_{n \rightarrow \infty} V_n$ .

L-systems are typically defined by a grammar which generates input for a turtle graphics system. We assume that each replacement rule adds a single “branch” to the main “trunk” of the tree. Without loss of generality, we assume the trunk is vertical. A branch of length  $c$  relative to the trunk can be added to the trunk at height  $h$  and angle  $\theta$  relative to the trunk, as shown in Figure 2. Each branch then becomes the trunk of a scaled-down, translated and rotated copy of the tree.

At this point, most authors derive a series of instructions for the turtle graphics system to produce the desired branch. In our case, we wish to use a chaos game rather than a turtle graphics system, so we will instead give a set of transformations which represent the L-system as a classical fractal.

The first of these transformations is simply a projection  $(x, y) \rightarrow (0, (\frac{L}{h})y)$  where  $h$  is the maximum vertical height of the rendered fractal and  $L$  is the length of the trunk. This transformation will map any point in the fractal to a point in the trunk. However, calculating the maximum height of the tree is difficult, so our implementation instead uses a randomized transformation

$$T_0(\vec{x}) = Y \begin{pmatrix} 0 \\ L \end{pmatrix} \quad (2)$$

where  $Y$  is a random variable uniformly distributed on  $[0, 1]$ .

The remaining transformations each map the trunk to one branch. For an L-system with  $N$  branches, each branch will correspond to one transformation. Branch  $i$  will correspond to transformation  $T_i(c_i, \theta_i, h_i)$ , where  $(c_i, \theta_i, h_i)$  are respectively the scale factor, rotation angle, and translation distance of the branch, as shown in Figure 2. For branch  $i$  of length  $c_i$  and angle  $\theta_i$  relative to the trunk at height  $h_i$  along the trunk, the transformation is

$$T_i(\vec{x}) = c_i \begin{pmatrix} \cos \theta_i & -\sin \theta_i \\ \sin \theta_i & \cos \theta_i \end{pmatrix} \vec{x} + \begin{pmatrix} 0 \\ h_i \end{pmatrix} \quad (3)$$

which is just a rotation, a scaling, and a translation.

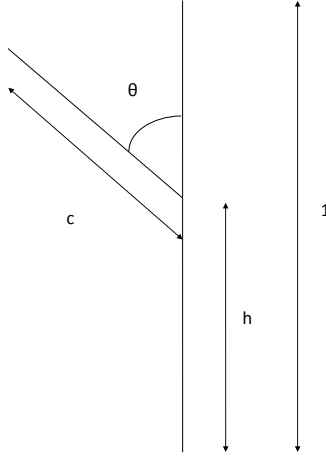


Figure 2: Parameters of a branch in an L-system. The branch (angled line) sprouts from the trunk (vertical line) at height  $h$  and angle  $\theta$  and has length  $c$ . Lengths are relative to the trunk length of 1. The constant  $c$  becomes a scale factor,  $\theta$  a rotation angle, and  $h$  a translation distance in the transformations which define the L-system.

Altogether, the L-system is specified by the transformation  $T_0$  given by Equation 2 and one transformation  $T_i$  for each branch given by Equation 3.

When the fractal is given as the attractor of an iterated function system as above, it can easily be expressed as a chaos game. The chaos game begins with any point  $\vec{x}_0$  in  $\Omega$ . At each iteration  $n$ , the chaos game computes

$$\vec{x}_n = T_K \vec{x}_{n-1} \quad (4)$$

where  $K$  is a randomly chosen branch index.

By randomly selecting a transformation at each iteration, the chaos game samples points which rapidly converge to the attractor. Furthermore, the chaos game randomly samples points throughout the attractor, rather than systematically drawing only some points (as a turtle graphics system would).

### 3 Algorithm Walkthrough

In order to build intuition for the equations given above, this section will walk through the construction of a simple L-system. We will use the simple L-system from Figure 1.

The first step is to find the parameters for each branch. In this case, there are two branches. Both sprout from the top of the trunk, so  $h_1 = h_2 = 1$  (assuming a trunk height of 1). The branches are at an angle of  $\frac{\pi}{4}$  in either direction from trunk, so  $\theta_1 = -\frac{\pi}{4}$  and  $\theta_2 = \frac{\pi}{4}$ . Finally, each branch is a factor of 2 smaller than the trunk, so  $c_1 = c_2 = \frac{1}{2}$ . These parameters are illustrated in Figure 3.

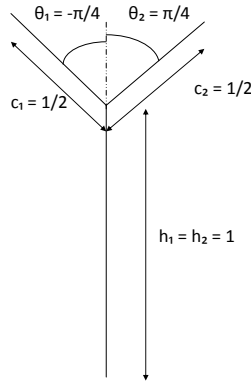


Figure 3: Parameters for the two branches of an L-system. These parameters yield the L-system in Figure 1.

Figure 4 illustrates how this L-system produces the figure shown in Figure 1. At each iteration, the outermost branches each act as a trunk and sprout two new branches. Each branch is at an angle of  $\frac{\pi}{4}$  relative to its parent and scaled down by a factor of 2.

In order to render the same fractal using a chaos game, we first select a random point. After some small number of iterations, transformation  $T_0$  will be selected. Transformation  $T_0$  maps any point to a random point on the trunk. This is illustrated in the first panel of Figure 5. With each iteration, one of the three transformations  $T_0, T_1, T_2$  is selected. Any time  $T_0$  is selected, the current point is mapped to a random point on the trunk. If  $T_1$  or  $T_2$  is selected, then the current point is mapped to the corresponding point on branch 1 or 2, respectively, off the current branch. At each iteration, the point is plotted. This continues indefinitely.

## 4 Results

Finally, we present a few examples of L-systems rendered using a chaos method which resemble real trees. All of the examples shown use randomized parameters for four branches. Two of the branches start at the top of the trunk, as in the previous example, but have a random angle. The other two branches start at a random location on the trunk and a random angle. All branches have a scale factor  $\frac{1}{2}$ , since a constant scale factor tends to produce realistic images. Several sample renderings are shown in Figure 6. All figures were rendered in 3 seconds by a chaos game written in Python.

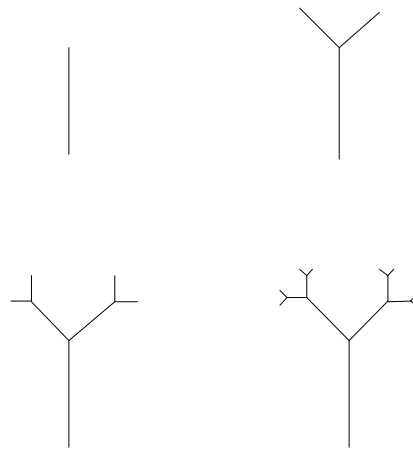


Figure 4: L-system as a turtle graphics method would render using a maximum number of iterations of 1, 2, 3, and 4 (from top left). As the number of iterations increases, the L-system approaches its true fractal, but the number of small components drawn increases exponentially.

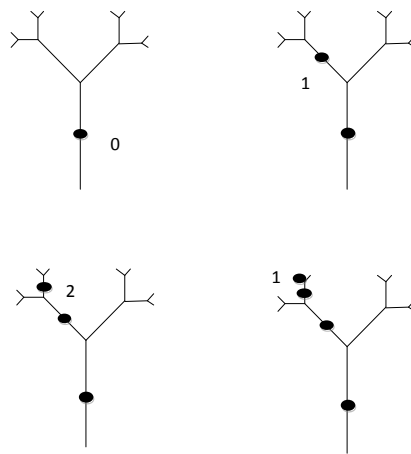


Figure 5: Illustration of a chaos game rendering of the L-system in Figure 1. We begin with a point on the trunk (assuming transformation  $T_0$  was chosen). Selecting transformation  $T_1$  maps this point to a new point on branch 1 of the trunk. Next,  $T_2$  is selected, mapping the most recent point to branch 2 of the most recent branch. Finally,  $T_1$  is selected, mapping the most recent point to branch 1 of the most recent branch. The chaos game continues indefinitely in this manner, plotting each point until the underlying L-system is rendered.

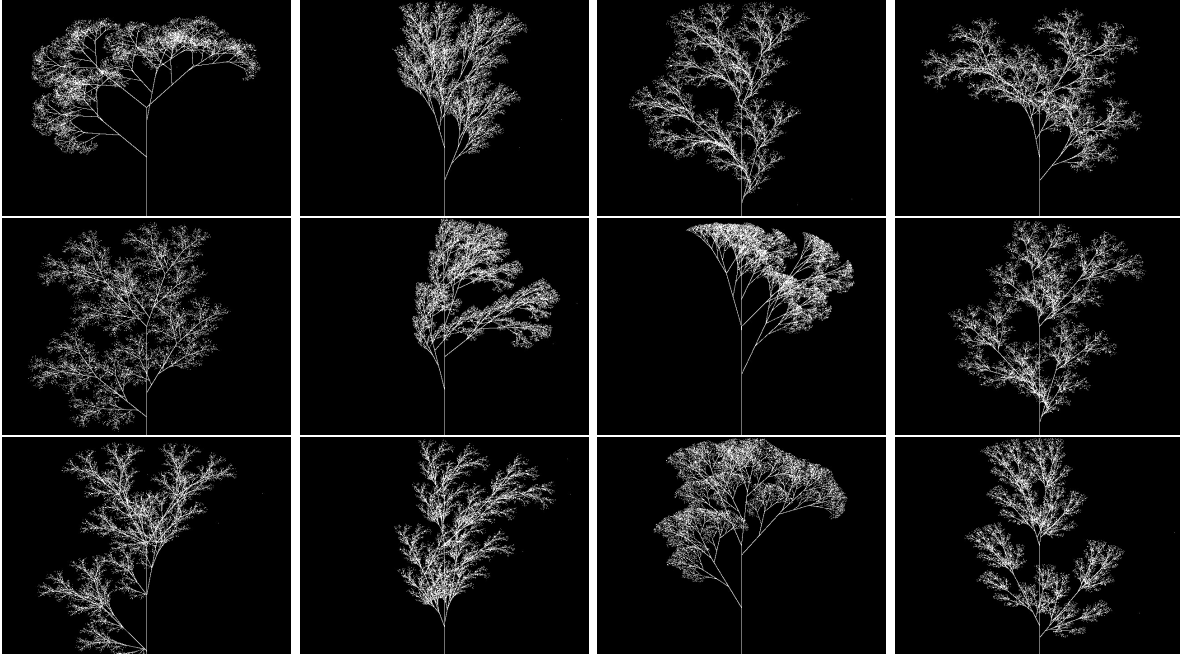


Figure 6: Sample trees with random parameters. All trees shown were generated in 3 seconds using a chaos game implemented in Python.

## 5 Conclusion

We have shown that a chaos game can be used to render L-systems, and we have presented the equations needed to implement such a rendering system. This method can produce realistic images of trees. It remains to be determined whether the chaos game method is faster than the turtle graphics method for rendering L-systems.

# Investigation of the Ikeda map

*Michael Fox*

**Abstract:** Through a numerical investigation of the Ikeda map

$$z_{n+1} = p_0 + Rz_n \exp \left( i \left( \phi - \frac{\alpha}{1 + |z_n|^2} \right) \right),$$

we discover that increasing  $R$  increases the number of points in the attractor set, ultimately leading to chaos as  $R$  approaches 1. In particular, the chaotic strange attractor which results when  $p_0 = 1.0$ ,  $R = 0.9$ ,  $\phi = 0.4$ , and  $\alpha = 6.0$  is found to have a correlation dimension of about  $D = 1.6815$ . In a physical sense, the chaotic behavior of the Ikeda map can be viewed as the output behavior of a system (of light traveling around a ring cavity) becoming more chaotic as the reflectivity (of the input and output mirrors) increases.

## 1 Introduction

In this paper we will examine the Ikeda map. This map was introduced by Japanese physicist Kensuke Ikeda in 1979 [1] as a model for light pulses traveling around a ring cavity with a nonlinear dispersive medium, as shown in Fig. 1 [2]. The Ikeda map can exhibit chaos, which corresponds to unstable and chaotic behavior of the light outputted by the physical system [1].

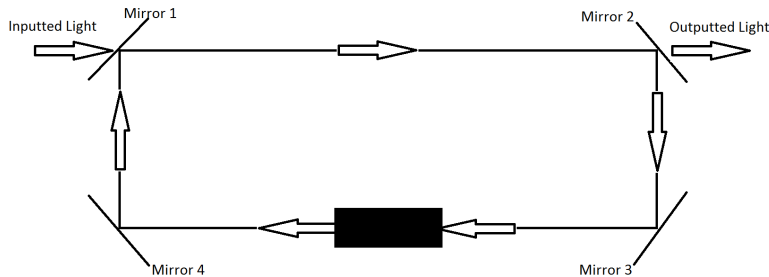


Figure 1: Light traveling around a nonlinear system of four mirrors. Mirror 1 and Mirror 2 are partially transmitting.

## 2 Definition of the map

The Ikeda map is a complex map given by

$$z_{n+1} = p_0 + Rz_n \exp \left( i \left( \phi - \frac{\alpha}{1 + |z_n|^2} \right) \right).$$

When viewed as a series of light pulses (as in Fig. 1) of intracavity amplitude  $E_n$ , dimensionless detuning  $\Delta$  of the laser two-level-atom, and linear absorption per pass  $\alpha_0 L$ , the parameters of the

Ikeda map are

$$\begin{aligned} p_0 &= \frac{E_{in}\sqrt{1-R}}{\Delta}, \\ \phi &= kL, \\ \alpha &= \frac{\alpha_0 L}{2\Delta}, \end{aligned}$$

where  $R$  is the reflective intensity of the input and output mirrors (Mirror 1 and Mirror 2). Thus  $R$  can take on values from 0 (fully transmissive input and output mirrors) to 1 (fully reflective input and output mirrors). This paper will focus on how different values of  $R$  affect the system. The variable  $z_n$  represents the dimensionless intracavity complex field amplitude. [2]

It is often helpful to transform complex maps into real maps. In the case of the Ikeda map, setting  $z_n = x_n + iy_n$  and applying Euler's formula, we end up with the following two-dimensional real map:

$$\begin{aligned} x_{n+1} &= p_0 + R(x_n \cos \theta - y_n \sin \theta), \\ y_{n+1} &= R(y_n \cos \theta + x_n \sin \theta), \end{aligned}$$

where

$$\theta = \phi - \frac{\alpha}{1 + x_n^2 + y_n^2}.$$

### 3 Results and Discussion

Throughout these computations, we will be using parameter values  $p_0 = 1.0$ ,  $\phi = 0.4$ , and  $\alpha = 6.0$ , as suggested in "Spring 2000 Control in Chaos: Semester End Report" [3].

#### 3.1 Bifurcations

In order to explore the effects that  $R$  has on this map, we plotted bifurcation diagrams for the real (top graph of Fig. 2) and imaginary (bottom graph of Fig. 2) components of  $z_n$  for varying values of  $R$ . In both cases, we used 1000 evenly spaced values of  $R$  from 0 to 0.9. For each value of  $R$ , we used an initial condition of  $z_0 = 0$  (so  $x_0 = y_0 = 0$ ) and then iterated the map 1300 times. The first 1000 points were thrown out, and only the last 300 points were plotted for each  $R$  value.

We see that both plots have a fixed point for  $R$  values up to approximately 0.4 before starting to exhibit period-doubling. As  $R$  increases to around 0.7, chaos begins to emerge. Remember that, in the physical model, this chaos represents unpredictability in the behavior of the light. Thus, as the input and output mirrors become more reflective, the system becomes more chaotic.

#### 3.2 Attractors

The attractors in Fig. 3 give us another way to look at the impact of changing  $R$ . In each plot, we again used an initial value of  $z_0 = 0$ . We then threw out the first 500 iterations of the map and plotted the imaginary component versus the real component for the next 1 million iterations.

We see that a fixed point occurs when  $R = 0.3$ , as the system eventually settles upon a value of  $z \approx 0.7715 + 0.0384i$ , which means this point is mapped to itself. When  $R = 0.5$ , the attractor is a set of two points,  $z_a \approx 0.6090 - 0.2002i$  and  $z_b \approx 0.8346 + 0.2745i$ , which means these points are mapped to each other. When  $R = 0.7$ , we begin to see chaos emerge, culminating in the chaotic strange attractor for  $R = 0.9$ .

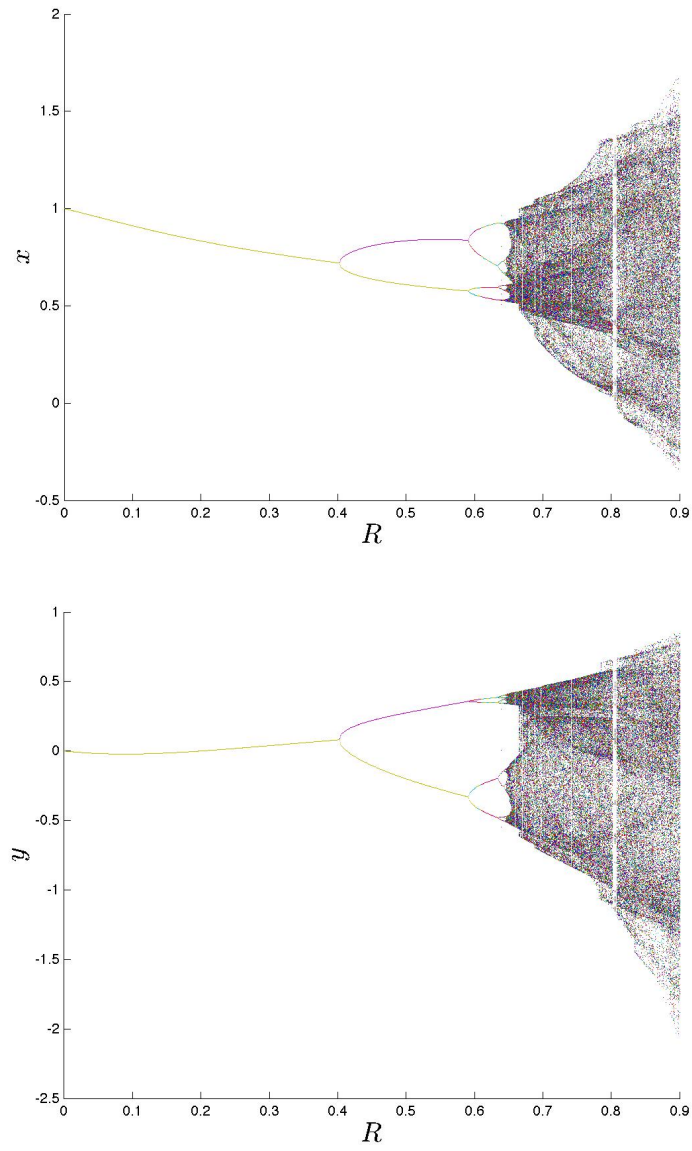


Figure 2: Bifurcation diagrams for period-doubling in the Ikeda map with parameter values  $p_0 = 1.0$ ,  $\phi = 0.4$ , and  $\alpha = 6.0$ .

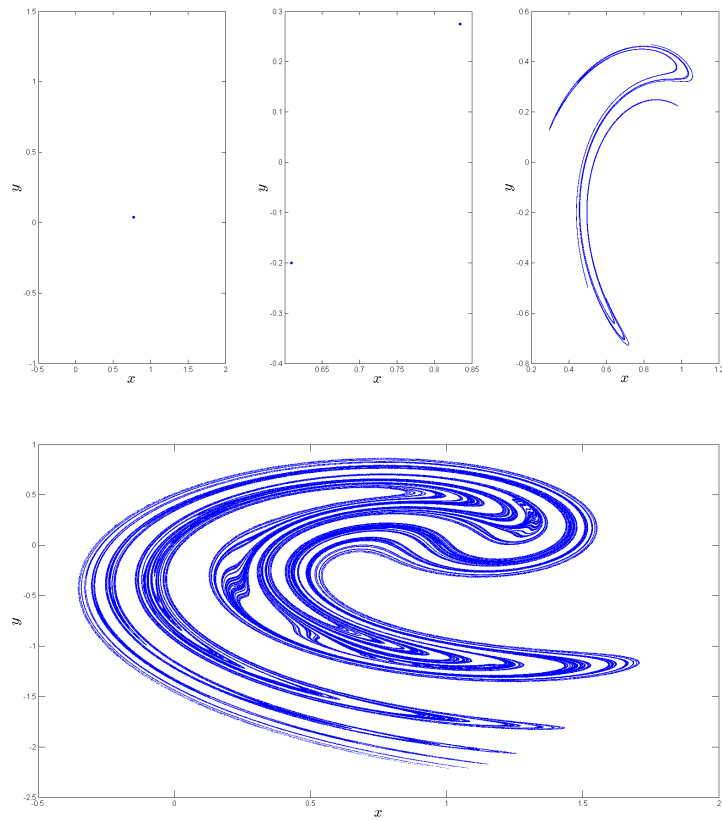


Figure 3: Attractors for the Ikeda map with parameter values  $p_0 = 1.0, \phi = 0.4, \alpha = 6.0,$  and  $R = 0.3, 0.5, 0.7,$  and  $0.9,$  respectively.

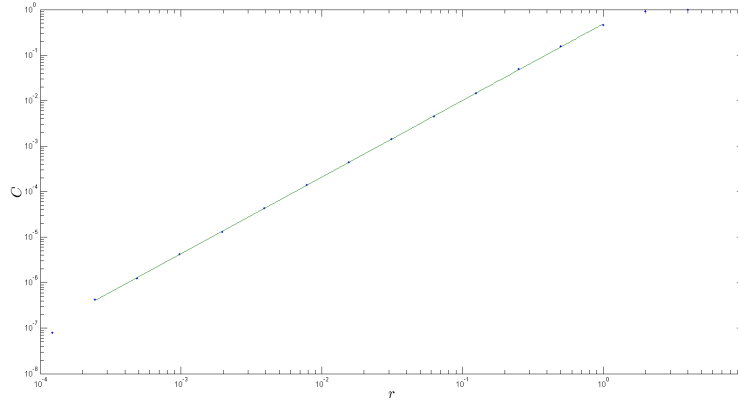


Figure 4: Log-log plot of the correlation integral  $C(r)$  versus  $r$  for the strange attractor for the Ikeda map with parameter values  $p_0 = 1.0$ ,  $R = 0.9$ ,  $\phi = 0.4$ , and  $\alpha = 6.0$  (as shown in the bottom of Fig. 3). The slope of the line corresponds to a correlation dimension of about  $D = 1.6815$ .

### 3.3 Correlation dimension

Finally, we computed the correlation (or fractal) dimension for the strange attractor shown in the bottom of Fig. 3. To do this, we again used an initial value of  $z_0 = 0$  and threw out the first 500 iterations of the map. We then calculated the next 10,000 points and used these points in our computation of the correlation dimension. Using MATLAB code provided by Jeffrey Chasnov, we computed and plotted (in Fig. 4) a log-log plot of  $C(r)$ , the correlation integral, for values of  $r$  spaced evenly logarithmically [4]. After looking at this graph, we were able to determine which points appeared to form a relatively straight line. We then used Chasnov's code to calculate the slope of this line using a least-squares fit. This slope gives us an estimate for the correlation dimension, which was calculated to be about  $D = 1.6815$ . In other words, this strange attractor has dimensionality somewhere between that of a line (dimension 1) and a plane (dimension 2).

#### Acknowledgments:

I would like to thank my professor Jeffrey Chasnov for his helpful teaching, lecture notes, and MATLAB code.

### References

- [1] Ikeda, Kensuke. "Multiple-valued stationary state and its instability of the transmitted light by a ring cavity system." *Optics Communications*. 30.2 (1979): 257-261.
- [2] Alsing, P.M., A. Gavrielides, and V. Kovanis. "Controlling Unstable Periodic Orbits in a Non-linear Optical System: the Ikeda Map." *Nonlinear Optics: Materials, Fundamentals and Applications*. (1994): 72-74.
- [3] Po-Jen, Huang. "Spring 2000 Control in Chaos: Semester End Report." N.p., 26 May 2000. Web. 16 Apr 2013. <<http://math.arizona.edu/~ura-reports/001/huang.pojen>>.
- [4] Chasnov, Jeffrey. *Scientific Computing: Lecture notes for MATH 164*. (2013). Web. 16 Apr 2013. <<http://www.math.hmc.edu/math164-01/scientific-computing.pdf>>.

# Chaotic Dynamics of the Standard Map

*Mitul Verma*

**Abstract:** Chaos theory is the fascinating study of unpredictability arising in well-defined mathematical systems that falls neatly between the study of deterministic, analytic systems and stochastic processes. The goal of this paper is to explore the features of Hamiltonian chaos in the standard map which, can be used to model physical systems like the *kicked rotor*. We will try and gain insight into the system dynamics by considering phase space plots at various parameter values and bifurcation diagrams of both variables  $\theta$  and  $p$  versus the parameter  $k$ .

## 1 Introduction

The standard map is an area-preserving map for two generalized variables - position,  $\theta$ , and momentum,  $p$ . The map is periodic with period  $2\pi$  in both variables, so it can be thought of as existing on a torus (by taking both  $\theta$  and  $p$  mod  $2\pi$ ). It was invented by Russian physicist Boris Chirikov in 1969 and has far reaching applications in physics and mathematics. This is because the map describes a universal characteristic of area-preserving maps; namely, a phase space divided into *sticky islands of stability* and a *sea of chaos*. (We will understand what these suggestive terms mean when we consider various phase space plots of the standard map.) Thus, numerous dynamical systems are reducible to the standard map, which is why it is called standard. A few examples of such systems are [1]

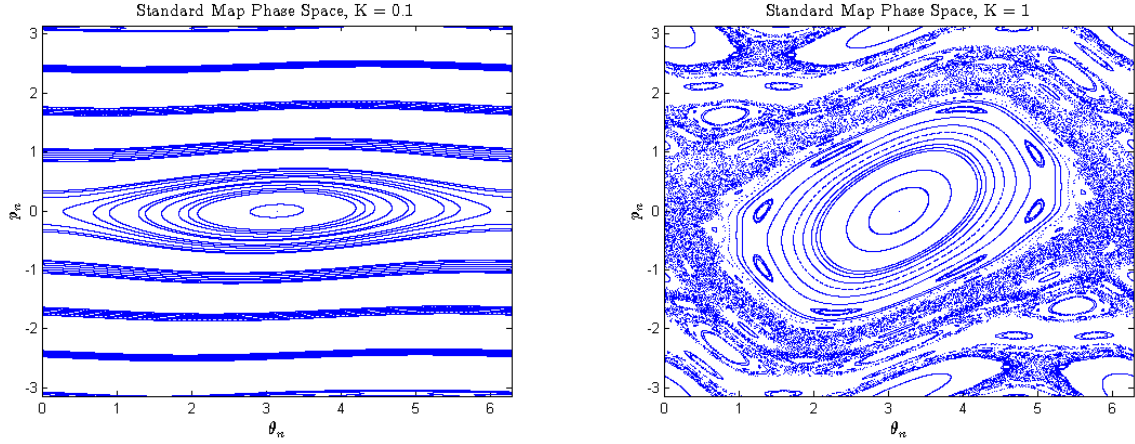
- charged particle confinement in mirror magnetic traps;
- particle dynamics in accelerators; and in particular, synchrotron dynamics approximated by the kicked rotor model;
- maps describing comet dynamics in the solar system;
- microwave ionization of Rydberg atoms and autoionization of the molecular Rydberg state.

The standard map, by varying a control parameter, goes from exhibiting regular, periodic behavior to exhibiting unpredictable, chaotic behavior. Although this descent into chaos is a common feature of chaotic systems, what is different about the standard map is that it is Hamiltonian, or conservative. That is, the standard map is area-preserving: if we consider a phase droplet in the 2-D phase space, its area remains constant even though it might get warped and distorted with time. This is in contrast to other systems studied in detail, like the forced, damped pendulum or the Lorenz attractor, which are dissipative in nature. We will compare Hamiltonian and dissipative systems in more detail when we consider phase plots of the standard map.

## 2 Governing equations

The standard map is defined by the following equations:

$$\begin{aligned} p_{n+1} &= p_n + k \sin \theta_n, \\ \theta_{n+1} &= \theta_n + p_{n+1}, \end{aligned} \tag{1}$$



(a) Phase space plot,  $k=0.1$

(b) Phase space plot,  $k=1$

Figure 1: Phase space plots. (a)  $k = 0.1$ ; (b)  $k = 1$ .

where both  $\theta$  and  $p$  are taken modulo  $2\pi$ . The control parameter  $k$  determines the degree of non-linearity in the system, and thus, the degree to which the system is chaotic.

To model the kicked rotor, we first need to define what a kicked rotor is. The kicked rotor can be thought of as a particle in a gravity-free environment confined to move on a circle. The particle has angular position  $\theta$  and angular momentum  $p$ . It is periodically "kicked" with amplitude  $k$ . By a "kick" we mean a periodic impulse as a forcing term. As we increase the strength of the kick  $k$ , the system becomes more chaotic.

Fixed points of (1) are found by setting

$$p_{n+1} = p_n, \quad (2)$$

$$\theta_{n+1} = \theta_n. \quad (3)$$

Equation (2) yields  $k \sin \theta_n = 0$ , or  $\theta_n = 0, \pi$ . Equation (3) yields  $p_n = 0$ . Therefore, the fixed points of (1) are  $(\theta, p) = (0, 0)$  and  $(\pi, 0)$ . [2]

### 3 Results

We shall now consider phase space plots of the standard map as  $k$  increases, bifurcation diagrams at the fixed point  $(\pi, 0)$ , and the fractal structure of the phase space at large values of  $k$ .

#### 3.1 The phase space

Notice that at small values of  $k$ , the standard map phase space resembles the phase space of a simple pendulum, as shown in Figure 1(a) for  $k = 0.1$ . As  $k$  increases, we start to notice chaotic regions forming in the phase space. In Figure 1(b), note the chaotic component at the separatrix between the limit cycles. Also note smaller, quasiperiodic orbits around the main limit cycle. These orbits surrounding orbits are a dominant feature of the standard map and we will encounter them again when we observe the phase space at larger  $k$  values.

Next, let us consider the fixed point at  $(\pi, 0)$  at  $k$ -values of 4 and 4.1. [3] Notice that in Figures 1(a), 1(b), and 2(a), the point  $(\pi, 0)$  remains just a point. However, in Figure 2(b), at  $k > 4$ , the point has changed to a limit cycle. This is an example of a pitchfork bifurcation - the fixed point

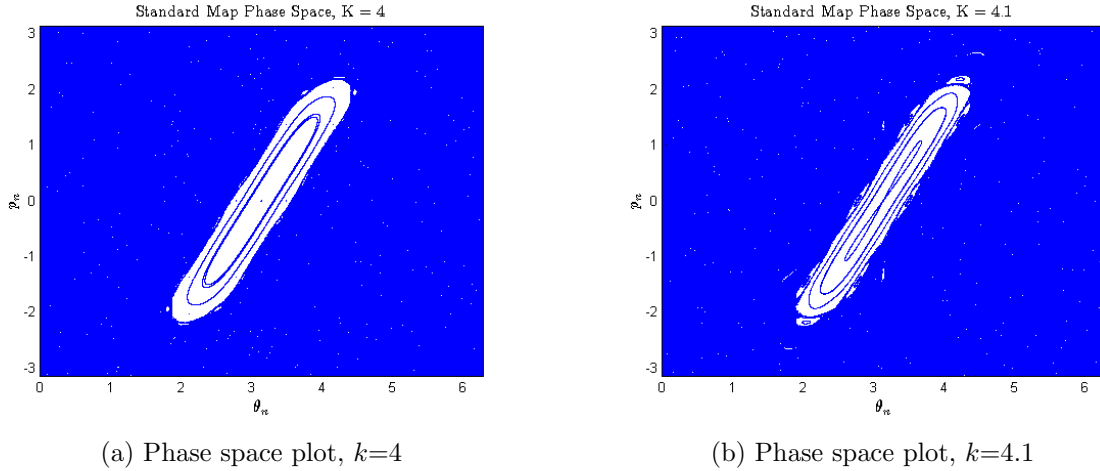


Figure 2: Phase plots showing pitchfork bifurcation at  $k = 4$ .

is no longer a stable point, but now is a stable orbit. With a further increase in  $k$ , the point  $(\pi, 0)$  will stop being fixed and become a part of the chaotic sea.

### 3.2 Bifurcations

In Figure 3, we consider the bifurcation diagram of the bifurcation we observed at  $(\pi, 0)$ .

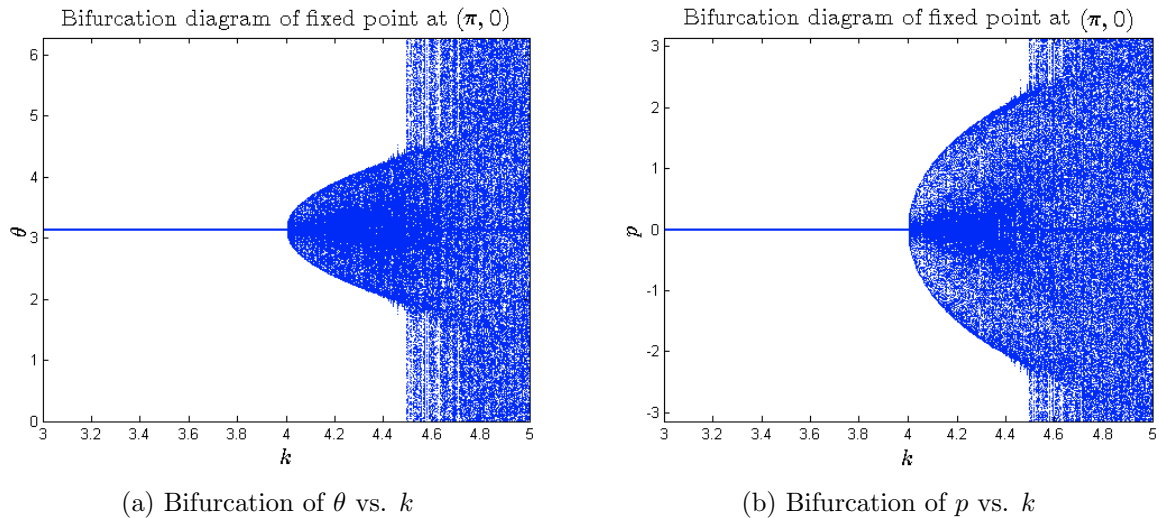
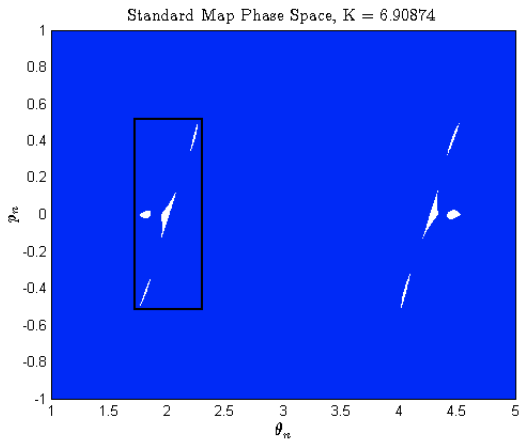
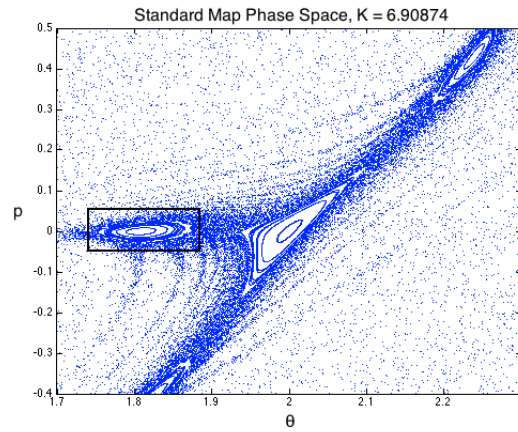


Figure 3: Diagrams showing bifurcation at  $k = 4$ .

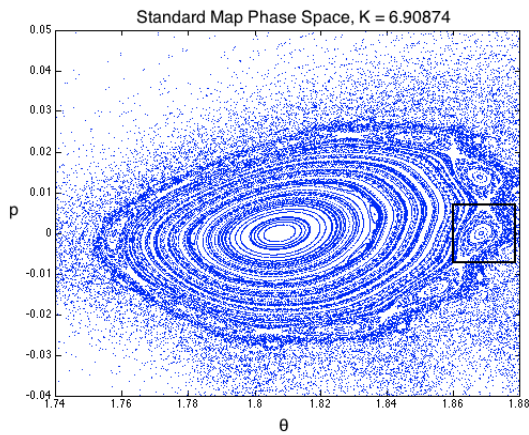
As we expected after observing Figure 2,  $(\theta, p) = (\pi, 0)$  bifurcates into a limit cycle, indicated by the shaded but bounded region in Figure 3. The entire section is plotted because as part of a limit cycle,  $\theta$  and  $p$  range between values at a particular  $k$ . Approximately around  $k = 4.45$ , the limit cycle breaks down and the point  $(\pi, 0)$  is engulfed by chaos. This will also be evident in the next few figures that highlight the fractal structure of stable islands.



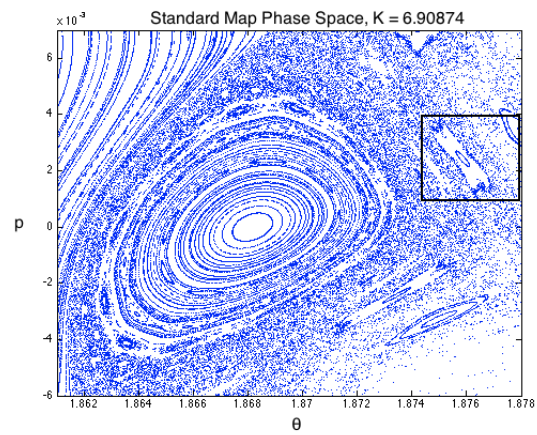
(a) Full phase space showing stable islands.



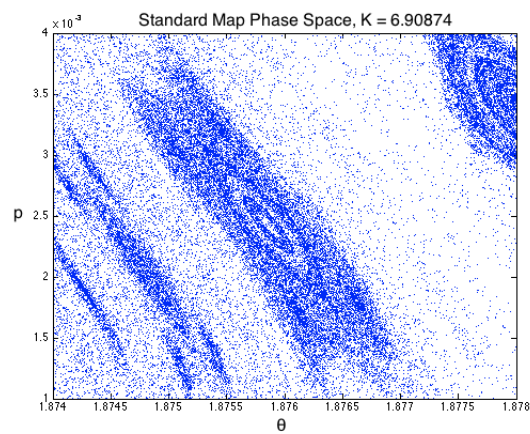
(b) Boxed section of (a) zoomed in.



(c) Boxed section of (b) zoomed in.

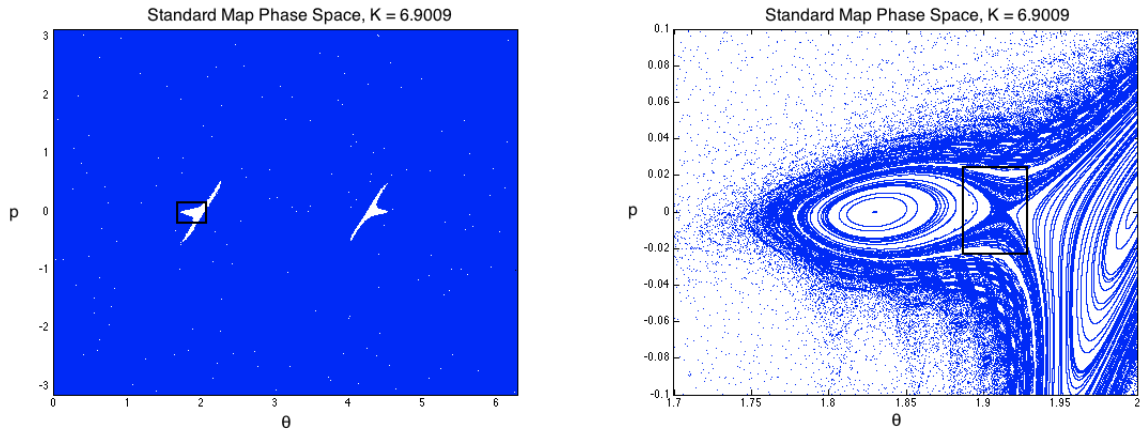


(d) Boxed section of (c) zoomed in.



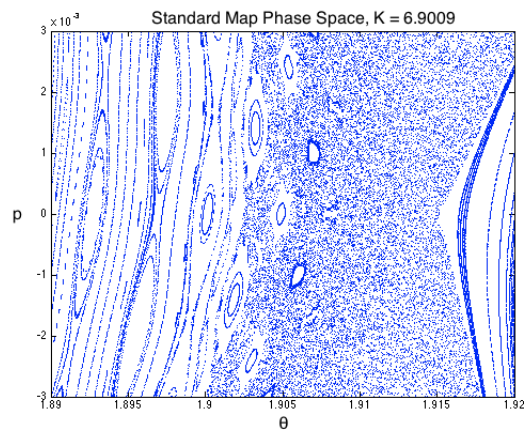
(e) Boxed section of (d) zoomed in.

Figure 4: Phase space diagrams showing fractal structure of islands, with  $k = 6.908745$ .



(a) Full phase space showing stable islands.

(b) Boxed section of (a) zoomed in.



(c) Boxed section of (b) zoomed in.

Figure 5: Phase space diagrams showing a *net trap*, with  $k = 6.9009$ .

### 3.3 Fractal structures in the phase space

Let us now consider the phase space with a critical value of parameter  $k = 6.908745$ . Figure 4(a) shows the entire phase space with this  $k$ . Notice that most of it is covered, indicating that the predominant behavior of the system is chaotic. Also notice that the point  $(\pi, 0)$  that was fixed earlier is now a part of the "sea of chaos." This confirms what we observed in the bifurcation diagram in Figure 3.

We still have two stable sections in the phase space. Figures 4(b)-(e) zoom in on parts of these sections to show more fixed points and limit cycles. Note that even though we continue to zoom in closer and closer to these islands of stability, we still have more structure to explore. More and more limit cycles and smaller islands of stability come into view as we go deeper into the phase space. This is very reminiscent of attractors and fractals. It is difficult, however, to attribute a phase space with a fractal dimension. There are simply too many points of chaos to extract a meaningful number about the fractional dimension.

Notice that the sections of the phase space closer to the island boundaries are more dense. This is what is meant by the *stickiness* of islands. Chaotic solutions seem to converge to the islands, while stable solutions exist inside the islands. The fractal nature of the islands is due to their sticky nature. Notice that the fractal structures arise at the boundaries of islands. Even as we zoom into islands, we notice more structure around the boundaries. This makes sense because the boundary of the island is between the stable solution and chaotic solution, acting as an intermediary and showing fractal structure.

This explains the challenge to computing the fractal dimension of the phase space. We have seen that the fractal structure is embedded in the "sticky" boundaries of the islands. Although we can qualitatively understand what stickiness means, to quantify it is difficult, and beyond the scope of this paper.

The last fractal structure we will consider is the *net trap*. Consider the phase space at  $k = 6.9009$  shown in Figure 5.

Figure 5(b) shows the stickiness of the island and the smaller islands embedded in the boundary, which form a net-like structure (hence the name "net trap"). Zooming in further, we see more limit cycles and fractal structure in Figure 5(c), which we have learned to expect from Figure 4.

## 4 Discussion

Armed with the knowledge of the above results, we can make some conclusions about the standard map and Hamiltonian systems in general.

We notice that there isn't a specific value of  $k$  which doubles the period, or sends the entire system to chaos, as is the case with most dissipative systems. As  $k$  is increased, the orbits get progressively warped and more quasiperiodic orbits start showing up. Sections of the phase space start degenerating to chaos, and after a point, the entire map is a sea of chaos, as we saw, with only a couple of small islands of stability.

These islands seem to have structure no matter how much we zoom into them, suggesting a fractal dimension. Solutions seem to converge to island boundaries, which we attribute to the stickiness of the islands. The fractal structure lives in the sticky boundaries, which makes it difficult to compute a fractal dimension using standard methods.

We also noted that the sticky islands are similar to attractors in dissipative systems. Hamiltonian systems do not have attractors, but dissipative systems do. Dissipative systems exhibit ergodic behavior on the strange attractors. This means that in the long run, the steady state solution approaches the attractor. Hamiltonian systems do not have attractors - rather, they have

sticky islands of stability floating in a sea of chaos.

**Acknowledgments:**

I would like to thank my professor Jeffrey Chasnov for his helpful comments and insight.

**References**

- [1] Boris Chirikov and Dima Shepelyansky (2008) Chirikov standard map. Scholarpedia, 3(3):3550.
- [2] <http://mathworld.wolfram.com/StandardMap.html>
- [3] The kicked rotor: Computer-based studies of chaotic dynamics H. J. Korsch, E. M. Graefe, and H.-J. Jodl FB Physik, TU Kaiserslautern, D-67653 Kaiserslautern, Germany

# Dimensions of Classical Fractals

*Neil Pearson*

**Abstract:** I calculate the fractal dimension of the Koch curve and the Sierpinski carpet both analytically and computationally. In order to do this I use the correlation integral to calculate the correlation dimension, and analytically calculate the similarity dimension. In addition to calculating the dimension of the classical fractals, I will compute the correlation dimension of one variant of a group of fractals called fern fractals.

## 1 Introduction

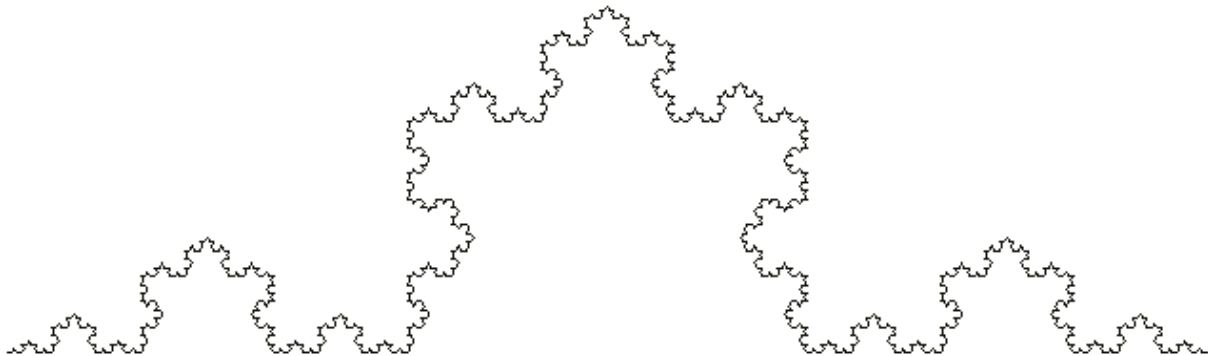
The Koch curve and Sierpinski carpet are classical fractals whose properties are well-studied. Because these fractals are self-similar, meaning that they are composed of smaller copies of themselves, we can analytically calculate their similarity dimensions. We can then compare the results of these calculations to the computed results of the correlation dimension to determine the accuracy of the computational result. For more interesting fractals, however, the simple analytical method of calculating the similarity dimension does not apply. The fern fractal is one such fractal, and I demonstrate the numerical calculation of its dimension.

## 2 Definitions

### 2.1 Koch Curve

The Koch curve can be constructed by starting with a horizontal line segment and creating an equilateral triangle, pointing upward, with the middle third of the line segment as the base. The base of the triangle is then removed, and the process is repeated for all line segments in the resulting shape. The Koch curve is the limiting curve obtained by repeating the above process an infinite number of times. Beginning with an equilateral triangle instead of a line segment results in the Koch snowflake. An image of a Koch curve is shown in Figure 1.

Figure 1: Koch Curve [2]

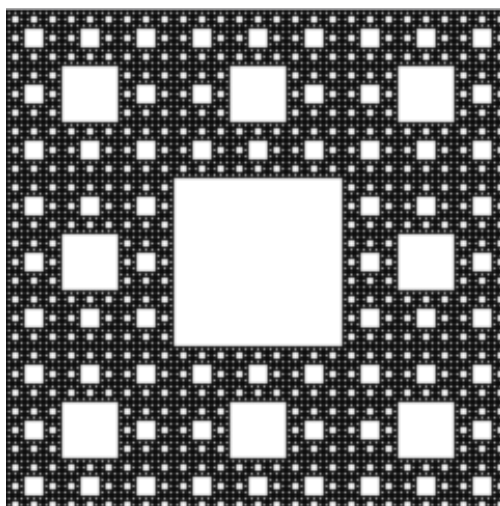


The Koch Curve has infinite length and is continuous everywhere on its length but differentiable nowhere. The Koch snowflake has these same properties, but encloses a finite area as well.

## 2.2 Sierpinski Carpet

The Sierpinski carpet can be constructed by starting with a square, cutting into nine equally-sized squares in a 3-by-3 grid, and then removing the center square. This same procedure is then applied to each of the eight remaining smaller squares. The Sierpinski carpet results when the above sequence is repeated an infinite number of times. An image of the Sierpinski carpet is shown in Figure 2.

Figure 2: Sierpinski carpet [5]



As the area of each iteration of the carpet is  $\frac{8}{9}$  of the previous one, the area of the Sierpinski carpet is zero.

## 2.3 Fern Fractal

Fern fractals can be starting with a slightly curved line, or stem, and adding scaled down versions of it up and down it's length, in the shape of a fern. Scaled down versions of those stems are then added up their lengths, such that each of these smaller ferns is similar to the larger one. This process is repeated *ad infinitum*, producing the fern. Depending on parameters such as the number of side "shoots" per stem, the length of these shoots, and curve of the stem, different fractals can be produced. An image of a fern fractal is shown in Figure 3. As with the other fractals, the fern fractal his a perimeter of infinite length. .

## 2.4 Similarity Dimension

Assume that a particular self-similar set  $S$  is composed of  $m$  copies of itself scaled down by a factor. We can then write

$$m = r^D \tag{1}$$

where  $m$  is the number of copies and  $r$  is the scaling factor. The calculated  $D$  is then called the similarity dimension of the set. [1]

Figure 3: Fern Fractal [4]



## 2.5 Correlation Dimension

Suppose we have a set  $S$  of  $N$  points. Denote the points in the set as  $x_i$ , with  $i = 1, 2, \dots, N$ . Denote the distances between two points  $x_i$  and  $x_j$  as  $r_{ij}$ . The correlation integral is then defined to be

$$C(r) = \lim_{N \rightarrow \infty} \frac{2}{N(N-1)} * (\text{number of distinct distances } r_{ij} \text{ less than } r).$$

If, for  $N$  sufficiently large,  $C(r)$  is proportional to  $r^D$  over a wide range of  $r$ , then  $D$  is called the correlation dimension of the set  $S$ . [1]

## 3 Results

### 3.1 Koch Curve

#### 3.1.1 Similarity Dimension

Each iteration of the Koch curve is formed by creating four copies of the previous iteration, each scaled down by a factor of three. This gives us

$$4 = 3^D \tag{2}$$

which results in a similarity dimension of  $D = \frac{\log 4}{\log 3} \approx 1.2618$ .

#### 3.1.2 Correlation Dimension

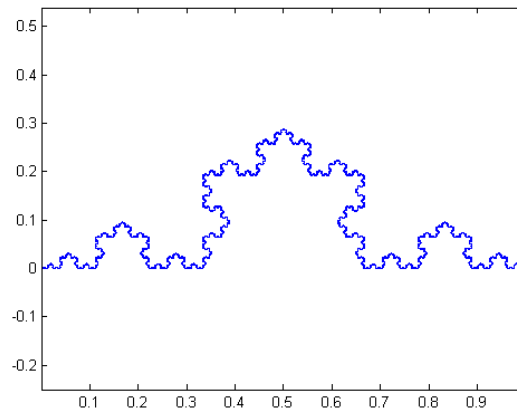
Using an iterated function system [3], we are able to produce a graph of a Koch curve in MATLAB. The graph shown in Figure 4 is a Koch Curve with 10,000 iterations, starting at  $(0,0)$ . Here, one iteration consists of copying the current point and applying one of four operations:

- scale by  $\frac{1}{3}$
- scale by  $\frac{1}{3}$ , rotate  $60^\circ$  and translate horizontally by  $\frac{1}{3}$

- scale by  $\frac{1}{3}$ , rotate  $-60^\circ$ , translate horizontally by  $\frac{1}{2}$  and vertically by  $\frac{\sqrt{3}}{6}$
- scale by  $\frac{1}{3}$  and translate horizontally by  $\frac{2}{3}$

The probability of choosing one of these operations is dependent on specified weights. For the Koch Curve, the probabilities are all equal. Although this method does not generate the same points as the method described in Section 2.1, all the points generated by this method will lie on the fractal curve. Starting at  $(0,0)$ , the four operations would generate the points  $(0,0)$ ,  $(\frac{1}{3}, 0)$ ,  $(\frac{1}{2}, \frac{\sqrt{3}}{6})$  and  $(\frac{2}{3}, 0)$ —four endpoints of the line segments generated by the method in Section 2.1, starting with a line segment from  $(0,0)$  to  $(0,1)$ . Since each of the four operations described above begins by scaling both dimensions of the most recently generated point by  $\frac{1}{3}$ , a new point is generated each time.

Figure 4: Koch curve produced in MATLAB



To calculate the correlation dimension of the fractal, we compute the correlation integral over all the points in the fractal set, and plot  $C(r)$  vs.  $r$  on a log plot, shown in Figure 5. Then, using MATLAB's polyfit function, we approximate the slope of these points to get our correlation dimension. Figure 5 shows the correlation dimension line for Koch curves composed of 1,000, 5,000, and 10,000 points (purple, red and blue respectively). By only calculating the fit line over the points that appear linear on a log-log plot, we satisfy the condition that  $C(r)$  be proportional to  $r^D$ . The calculated slopes for the purple, red and green points are 1.313, 1.245, and 1.261, respectively. As we increase the number of points, the correlation dimension converges to the calculated value of 1.2618.

## 3.2 Sierpinski Carpet

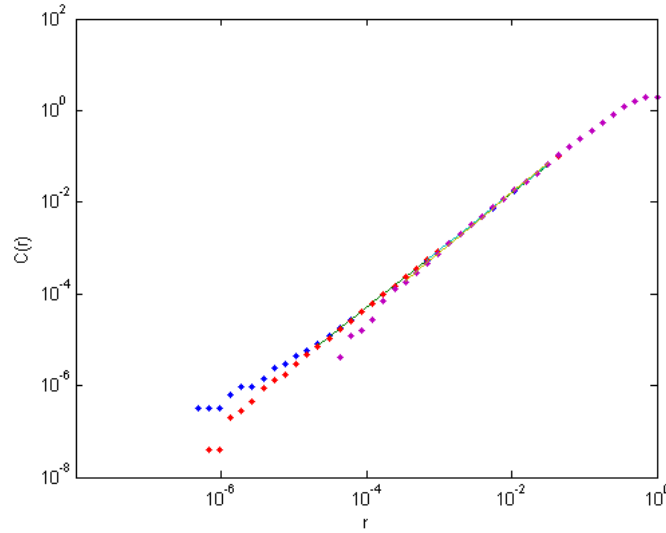
### 3.2.1 Similarity Dimension

Each iteration of the Sierpinski carpet is formed by creating 8 copies of the previous iteration, with each linear dimension scaled down by a factor of three. This gives us

$$8 = 3^D \quad (3)$$

which results in a similarity dimension of  $D = \frac{\log 8}{\log 3} \approx 1.8928$ .

Figure 5:  $C(r)$  vs  $r$  for the Koch Curve



### 3.2.2 Correlation Dimension

As with the Koch curve, an iterated function system allows us to produce a graph of the Sierpinski carpet in MATLAB. The graph shown in Figure 6 is a Sierpinski carpet with 10,000 iterations, where one iteration consists copying the current point and applying one of eight operations:

- scale both dimensions by  $\frac{1}{3}$
- scale both dimensions by  $\frac{1}{3}$ , translate horizontally by 1
- scale both dimensions by  $\frac{1}{3}$ , translate horizontally by 2
- scale both dimensions by  $\frac{1}{3}$ , translate vertically by 1
- scale both dimensions by  $\frac{1}{3}$ , translate vertically by 2
- scale both dimensions by  $\frac{1}{3}$ , translate horizontally by 1 and translate vertically by 2
- scale both dimensions by  $\frac{1}{3}$ , translate horizontally by 2 and translate vertically by 1
- scale both dimensions by  $\frac{1}{3}$ , translate horizontally by 2 and translate vertically by 2

Once again, the probabilities of choosing any of these operations is equal. Here, each point generated by the algorithm is a corner of one of the squares of the Sierpinski carpet. Again, not every corner is generated, as on the  $N$ th iteration only one of  $4 * 4^N$  possible new points will be created, but each point will be in the fractal set. To calculate the correlation dimension of the fractal, we compute the correlation integral over all the points in the fractal set, and plot  $C(r)$  vs.  $r$  on a log plot, shown in Figure 7. Then, using MATLAB's polyfit function, we approximate the slope of these points to get our correlation dimension.

Figure 6: Sierpinski carpet produced in MATLAB

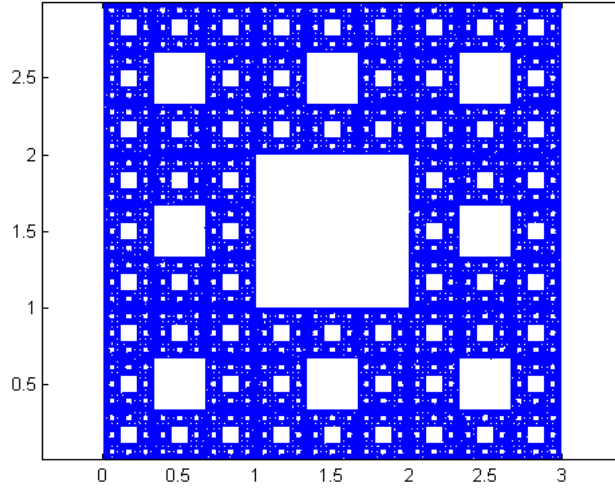


Figure 7:  $C(r)$  vs  $r$  for the Sierpinski carpet

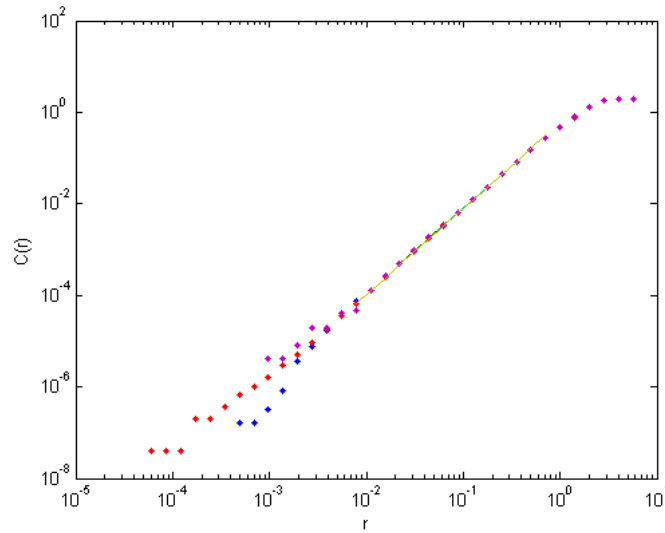


Figure 7 shows the correlation dimension line for Sierpinski carpet fractals composed of 1,000, 5,000, and 10,000 points (purple, red and blue respectively). By only calculating the fit line over the points that appear linear on a log-log plot, we satisfy the condition that  $C(r)$  be proportional to  $r^D$ . The calculated slopes for the purple, red and green points are 1.853, 1.863, and 1.881, respectively. As we increase the number of points, the correlation dimension converges to the calculated value of 1.8928.

### 3.3 Fern Fractal

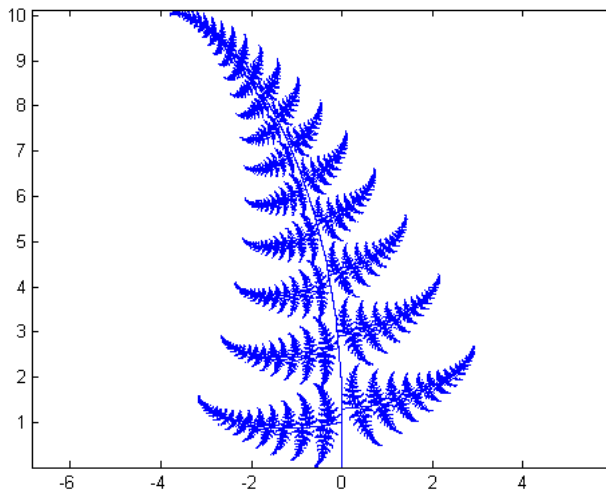
#### 3.3.1 Correlation Dimension

As each iteration of the fern fractal involves more than just one scaling factor, the similarity dimension cannot be calculated. However, it is still possible to compute the correlation dimension. Again, an iterated function system is used to produce a graph of a fern fractal in MATLAB. The graph shown in Figure 8 is a fern fractal after 50,000 iterations, where one iteration consists of copying the current point and applying one of four operations:

- scaling by 0.17 in the vertical dimension
- scaling by  $-0.3$  in the horizontal dimension,  $0.3$  in the vertical dimension, rotating by  $100^\circ$ , and translating by  $1$  in the vertical dimension
- scaling by  $0.3$  in the horizontal dimension,  $0.3$  in the vertical dimension, rotating by  $-85^\circ$ , and translating by  $1.3$  in the vertical dimension
- scaling by  $0.81$  in the horizontal dimension,  $0.85$  in the vertical dimension, rotating by  $5^\circ$ , and translating by  $1.8$  in the vertical dimension

In this case, the probabilities for choosing these operations are not equal, but at a ratio of approximately  $2 : 12 : 12 : 72$ .

Figure 8: Fern fractal produced in MATLAB



To calculate the correlation dimension of the fern fractal, we compute the correlation integral over all the points in the fractal set, and plot  $C(r)$  vs.  $r$  on a log plot, shown in Figure 9. Then, using MATLAB's polyfit function, we approximate the slope of these points to get our correlation dimension.

Figure 9:  $C(r)$  vs  $r$  for the fern fractal

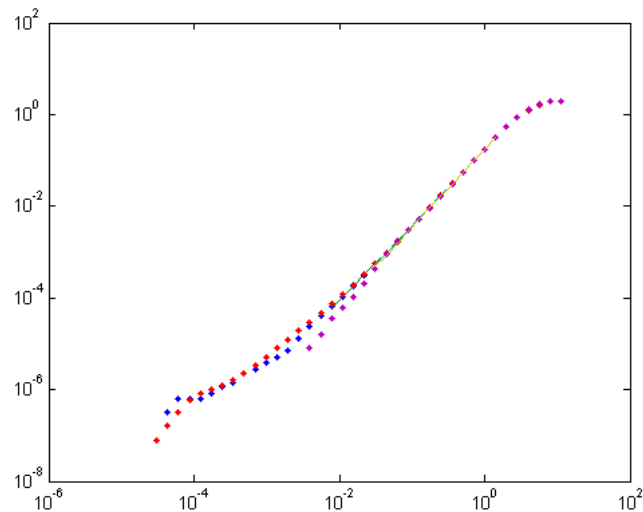


Figure 9 shows the correlation dimension line for fern fractals composed of 1,000, 5,000, and 10,000 points (purple, red and blue respectively). By only calculating the fit line over the points that appear linear on a log-log plot, we satisfy the condition that  $C(r)$  be proportional to  $r^D$ . The calculated slopes for the purple, red and green points are 1.703, 1.622, and 1.671, respectively. As we increase the number of points, the correlation dimension should converge to the true value, so we take 1.67 as the calculated dimension of the fern fractal.

## 4 Discussion

One major issue with the algorithm used to calculate correlation dimension is that it does not produce the same result every time. This is because the algorithm used to produce the fractals does so by randomly applying the operations on a starting point. The resulting fractals have the same general shape, but are not composed of the same specific points. Iterated an infinite (or very large) number of times, the correlation dimension should approach one value, but MATLAB reached its memory constraints before such a number of iterations took place. However, the larger numbers of points we can see a clear convergence towards the known value for classical fractals.

### Acknowledgments:

I would like to thank Prof. Jeffrey Chasnov for his input and valuable comments, and Carl Pearson for his assistance with L<sup>A</sup>T<sub>E</sub>X.

## References

- [1] Chasnov, Jeffrey. "Scientific Computing Lecture Notes for Math 164." *Math 164: Scientific Computing*. Harvey Mudd College, 2013. Accessed April 14, 2013. <http://www.math.hmc.edu/math164-01/scientific-computing.pdf>

- [2] Riddle, Larry. "Koch Curve." *Classic Iterated Function Systems*. Agnes Scott College, 2013. Accessed April 13, 2013. <http://ecademy.agnesscott.edu/~lriddle/ifs/kcurve/kcurve.htm>
- [3] Tuffley, Christopher. "Affine Iterated Function Systems." *Fractal*. Massey University, 2013. Accessed April 13, 2013. <http://www.massey.ac.nz/~ctuffley/fractals/>
- [4] "Barnsley Fern." *Wikipedia*. 2013. Accessed April 13, 2013. <http://en.wikipedia.org/wiki/Barnsleyfern>
- [5] "Sierpinski Carpet." *Wikipedia*. 2013. Accessed April 13, 2013. <http://en.wikipedia.org/wiki/SierpinskiCarpet>

# On the Stable Dynamics of the Free Brusselator Equations

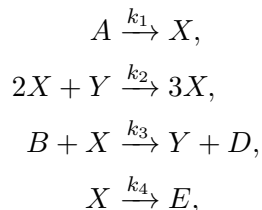
*Matt Hin*

## Abstract

The dynamics of the free Brusselator equations were investigated using both analytical and numerical methods. Linear stability analysis was used to determine and classify the sole equilibrium point of the free Brusselator system. A trapping region was constructed to prove the existence of a Hopf bifurcation and confirm the behavior of the system. The equilibrium point was determined to undergo a supercritical Hopf bifurcation, evolving from a single sink at the bifurcation point  $B = A^2 + 1$ . In addition, the period of the limit cycle increases exponentially with increasing parameter  $B$  and fixed  $A$ .

## 1 Introduction

The Brusselator equations were first proposed by Ilya Prigogine and his collaborators at the Free University of Brussels as a theoretical model of an autocatalytic reaction. The equations were derived from the following set of reactions:



where  $A$  and  $B$  are essential substrates,  $D$  and  $E$  are byproducts, and  $X$  and  $Y$  are the autocatalytic reactants of the set of reactions. Also,  $k_1, k_2, k_3$ , and  $k_4$  are the rate of reactions for each component reaction. An example of such an autocatalytic reaction are the clock reactions such as the Belousov-Zhabotinsky reaction as seen in Fig. 1.

## 2 Governing Equations

The governing equations of the Brusselator are obtained from the autocatalytic reaction using the law of mass action. As such we obtain the following set of equations for the change in concentrations of  $X$  and  $Y$ .

$$\begin{aligned}\frac{d[X]}{dt} &= k_1[A] + k_2[X]^2[Y] - k_3[B][X] - k_4[X], \\ \frac{d[Y]}{dt} &= -k_2[X]^2[Y] + k_3[B][X].\end{aligned}$$

Note that above we have used square brackets to denote concentrations of the reactants involved. We then nondimensionalize the equations and require the following stipulations:

$$k_1 = k_4 \quad \text{and} \quad \frac{k_1 k_3}{k_2} = \frac{(k_3)^3}{(k_2)^2} = 1.$$

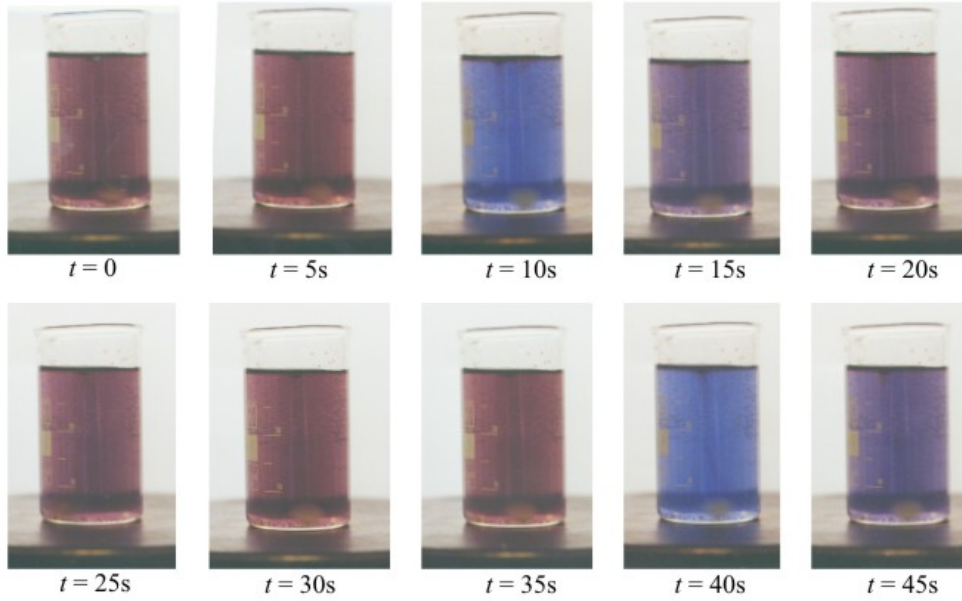


Figure 1: A Belousov-Zhabotinsky reaction over the course of its reaction.[2] Note that the color of the solution oscillates between red and blue.

Dropping the brackets for convenience, we then consider the free Brusselator equations given by

$$\begin{aligned}\dot{X} &= A - (B + 1)X + X^2Y, \\ \dot{Y} &= BX - X^2Y,\end{aligned}$$

with two free dimensionless parameters  $A, B \geq 0$ .

### 3 Analysis

We begin our analysis of the Brusselator equations by considering its nullclines. Setting each differential equation to zero, the nullclines for  $X$  and  $Y$  are given by

$$Y = \frac{(B + 1)X - A}{X^2}, \quad X = 0, \quad \text{and} \quad Y = \frac{B}{X}.$$

The intersection of the first and third nullcline yields a single fixed point for the Brusselator system located at  $(X_*, Y_*) = (A, B/A)$ . A linear stability analysis yields the following Jacobian evaluated at this fixed point:

$$J(X_*, Y_*) = \begin{bmatrix} B - 1 & A^2 \\ -B & -A^2 \end{bmatrix}.$$

Solving the eigenvalue problem for the Jacobian, we find that the characteristic polynomial for the Jacobian is

$$P(J) = \lambda^2 + \tau\lambda + \Delta,$$

where

$$\tau = A^2 - B + 1 \quad \text{and} \quad \Delta = A^2.$$

Setting this characteristic polynomial to 0, the quadratic formula yields the following eigenvalues of the fixed point  $(X_*, Y_*)$ ,

$$\lambda_{\pm} = \frac{-\tau \pm \sqrt{\tau^2 - 4\Delta}}{2}.$$

When  $B < A^2 + 1$ , the real component of the eigenvalues are negative and thus the fixed point is a stable sink. However as  $B$  increases past  $A^2 + 1$ , the fixed point becomes an unstable source. When  $B = A^2 + 1$ , the real part of the eigenvalues vanish and the eigenvalues become purely imaginary. Namely, at this bifurcation point, we have eigenvalues of

$$\lambda_{\pm} = \pm iA.$$

Hence, we find that locally, the fixed point  $(X_*, Y_*)$  is a stable sink for  $B < A^2 + 1$ , a center for  $B = A^2 + 1$ , and an unstable source for  $B > A^2 + 1$ . In addition, given that the eigenvalues have crossed the real axis as we increase  $B$ , we have strong evidence that a Hopf bifurcation occurs at  $B = A^2 + 1$ .

### 3.1 Trapping Regions and the Poincaré-Bendixson Theorem

In order to prove that a Hopf bifurcation occurs at  $B = A^2 + 1$ , we must prove that a limit cycle exists in this new unstable regime for the fixed point. We turn to the Poincaré-Bendixson theorem, which states that a trapping region for this dynamical system must contain either (1) a fixed point, (2) a limit cycle, or (3) a set of connected fixed points with orbits connecting them. A trapping region is a bounded set of points in phase space with the property that if an orbit begins at a point contained in the trapping region, the orbit stays in the region for all time. We will use this definition to prove that a limit cycle exists when  $B \geq A^2 + 1$ . We begin by arguing that since we have shown that there is only 1 fixed point for this system, the third outcome of the theorem is eliminated. Also, since  $\text{Re}\{\lambda_{\pm}\} > 0$  for the fixed point in this regime, the point is a source and thus must have orbits flow out of a ball centered about this point. If we omit this ball, we can continue to consider the nullclines of the system as depicted in Fig. 2.

Guided by the nullclines, it is apparent that in order to construct a trapping region, we must consider a truncated rectangle. Hence, we define the following boundaries:

- (1) The lower boundary of the region will be the  $X$ -axis.
- (2) The left boundary of the region will have to intersect the  $X$ -axis at the point where the  $\dot{X}$ -nullcline intercepts so as to direct the flow in the correct direction. Hence we have that our left wall will be defined by the vertical line  $X = A/(B + 1)$ . Note that  $\dot{X} > 0$  across this boundary.
- (3) The upper boundary of the region should meet the left boundary at its intersection with the  $\dot{Y}$ -nullcline. We find this point to be  $(X, Y) = (A/(B + 1), B(B + 1)/A)$ . Hence our upper wall will be defined by the horizontal line  $Y = B(B + 1)/A$ . Note that  $\dot{Y} < 0$  across this boundary.
- (4) We now need to construct a segment of the region whose flow will be directed towards the interior of the trapping region. Therefore for a normal vector  $\vec{n} = (n_1, n_2)$  to the segment, we require that

$$(n_1, n_2) \cdot (\dot{X}, \dot{Y}) < 0.$$

For our convenience, we let  $n_1 = n_2 = 1$  and discover that

$$\dot{X} + \dot{Y} = (A - (B + 1)X + X^2Y) + (BX - X^2Y) = A - X.$$

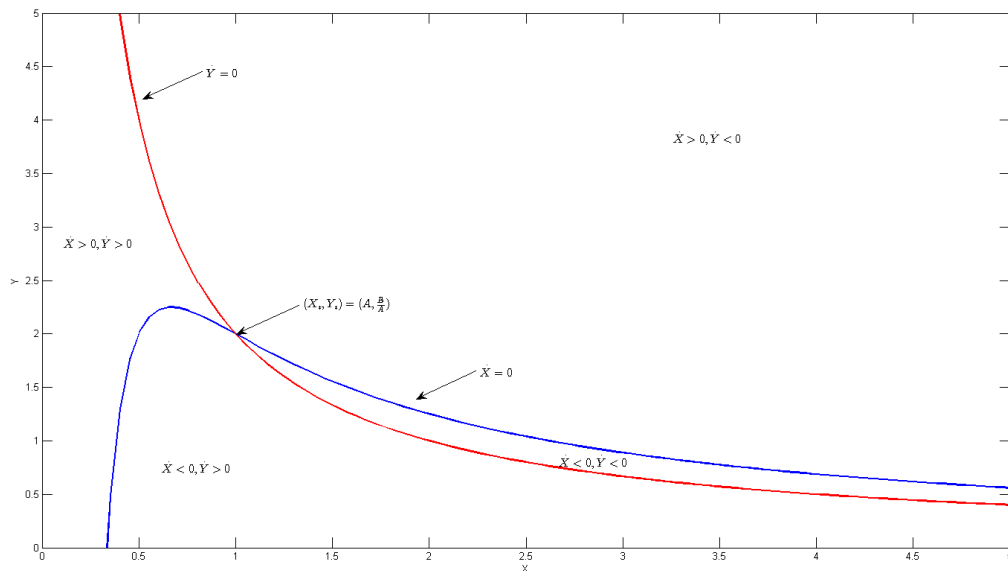


Figure 2: The nullclines of the Brusselator for  $A = 1$  and  $B = 2$ . Note that at their intersection, there is a fixed point  $(X_*, Y_*)$ .

Therefore in order for  $\dot{X} + \dot{Y} < 0$ , we have

$$X > A.$$

Thus, as long as  $X > A$ , our segment with normal vector  $(1,1)$  will have the desired property. Hence, our segment will be defined by the line:

$$Y - \frac{B(B+1)}{A} = A - X.$$

- (5) This leaves our right boundary of our region, which will have  $\dot{X} < 0$  for any point below the  $\dot{X}$ -nullcline. This can be easily constructed by using the  $X$ -coordinate of the intersection of the line segment and the  $\dot{X}$ -nullcline. Note that this value exists since the  $\dot{X}$ -nullcline approaches its zero asymptote while the line segment will cross the  $X$ -axis. Call this coordinate  $\bar{X}$ . Thus, our final wall of the region is the vertical line  $X = \bar{X}$ .

The fully formed trapping region can be seen in Fig. 3. Given our constructed trapping region, we can now appeal to the Poincaré-Bendixson Theorem. Since our trapping region does not contain a fixed point or a set of connected fixed points, it must therefore contain a limit cycle. Therefore we have shown that for  $B \geq A^2 + 1$ , a limit cycle exists, thus characterizing the bifurcation point  $B = A^2 + 1$  as a Hopf bifurcation.

## 4 Numerics

In order to investigate the dynamics of the Brusselator, we will turn to numerical methods to plot orbits in the  $X$ - $Y$  phase space. By using a Dormand-Prince[3] method with a square grid of  $N^2$  evenly spaced initial states in the phase portrait and extrapolating both forward and backward in time, we are able to characterize the dynamics at each regime numerically.

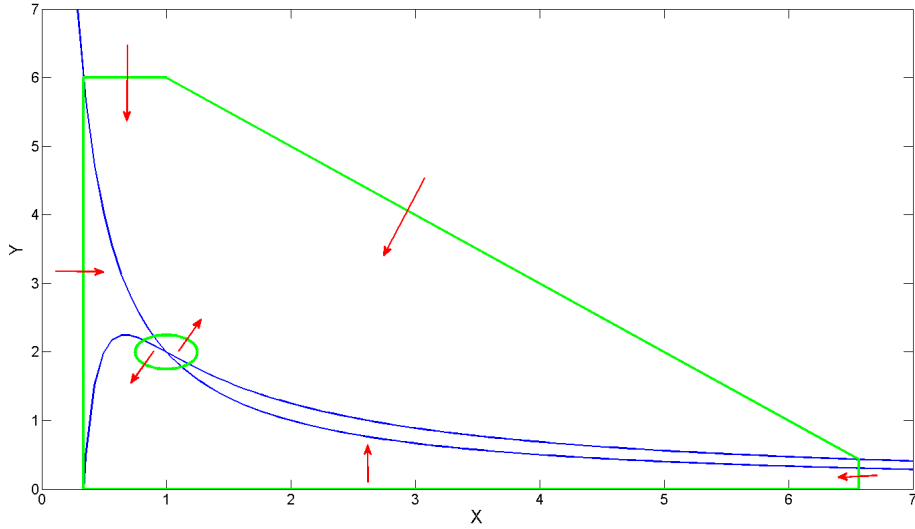


Figure 3: The trapping region is constructed in green above. Note that the boundaries of the trapping region are guided by the blue nullclines and guarantee that any flow crossing into the region will stay within that region for all time.

#### 4.1 Results

The phase portrait in the stable regime, for  $B < A^2 + 1$ , is depicted in Fig. 4a. We find that the fixed point in the stable regime is in fact a stable sink for all orbits in the phase plane. For  $B = A^2 + 1$ , we find that the fixed point has become a center, as illustrated in Fig. 4b. Once  $B > A^2 + 1$ , we find that the fixed point has transitioned into a spiral source and a stable limit cycle has evolved. Thus we find that indeed a Hopf bifurcation exists and that it is a supercritical one, as depicted in Fig. 4c.

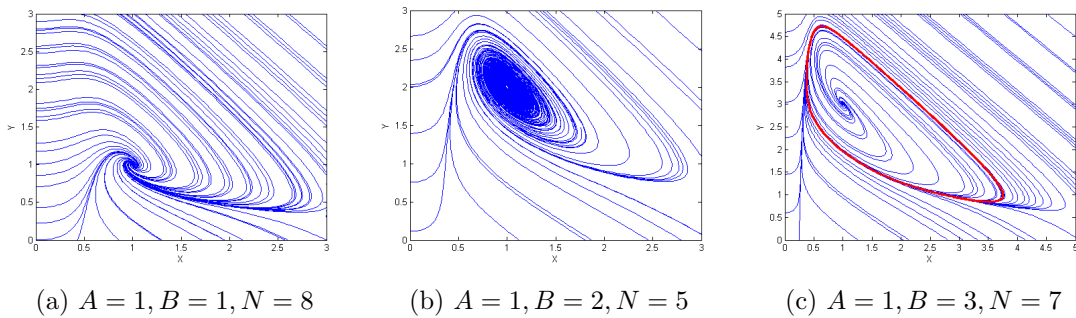


Figure 4: Phase portraits of orbits in the three different regimes of the Brusselator: stable, bifurcation, and unstable. Note that the red curve in Fig. 4c is a limit cycle.

#### 4.2 Relaxation-Oscillations

As we have numerically confirmed, for  $B > A^2 + 1$ , we find that the Brusselator contains a stable limit cycle. As shown in Fig. 5, the time series for  $X$  and  $Y$  along the limit cycle exhibit long periods of relaxation followed by sharp impulses. We identify this as relaxation-oscillations and we

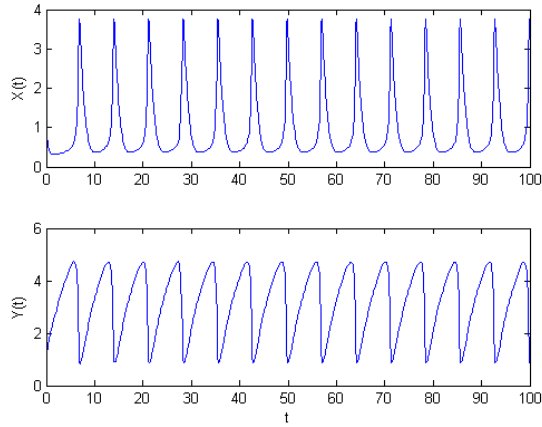
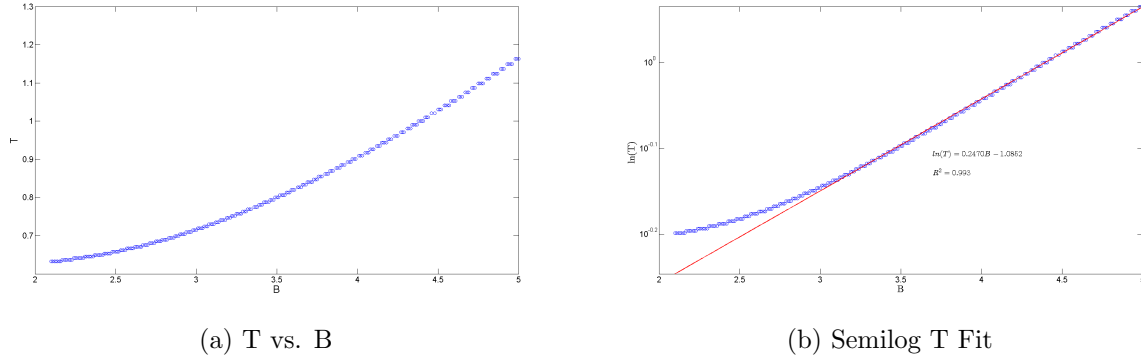


Figure 5: Time series for  $X$  and  $Y$  along the limit cycle. Note the long relaxation highlighted by sharp periodic impulses.



(a)  $T$  vs.  $B$

(b) Semilog  $T$  Fit

Figure 6: A plot of the period,  $T$  of the relaxation-oscillations versus the dimensionless parameter  $B$  on linear and semilog plots. Note that for  $B$  large enough, we have strong evidence for an exponential relationship.

will now attempt to characterize the period,  $T$ , of this limit cycle as a function of fixed  $A = 1$  and increasing  $B$  using numerical methods. By solving the governing equations for times  $t \in [0, 1000]$ , we can apply the Fast Fourier Transform (FFT) with a frequency of about 40 samples per unit of  $t$  to analyze the time series in the frequency domain. By isolating the frequency with the largest magnitude, we can capture the periodicity of the orbit. In addition, these sampling parameters reduce the discretization effects caused by the FFT. In Fig. 6a, we have plotted  $T$  as a function of  $B$ . We notice that  $T$  appears to exponentially increase as  $B$  linearly increases. We confirm this behavior for  $B > 3$  using a linear fit to a semilog plot, as depicted in Fig. 6b. We find that for  $B$  sufficiently larger than  $A^2 + 1$ , the period of the relaxation-oscillations follow the function

$$T \approx (0.3378)e^{0.2470B},$$

which has a goodness of fit value of  $R^2 = 0.993$ , indicating a strong approximation.

## 5 Discussion

We have discovered that the Brusselator undergoes a Hopf bifurcation at  $B = A^2 + 1$ , at which point a limit cycle evolves from a stable equilibrium point. We have verified our analysis that the dynamics evolve as such with phase diagrams numerically generated in both the stable and unstable regimes for the fixed point. We have also discovered that for large enough values of  $B$ , the period of the limit cycle appears to grow exponentially as  $B$  increases. Note that in our consideration of the Brusselator system, we have assumed that the parameters  $A$  and  $B$  are constants and thus do not depend on time. Physically this correlates to having a source of replenishment for the substrates in the set of autocatalytic reactions. Unfortunately this is not possible for most physical systems in which case, it is therefore feasible for a system to begin in the stable regime, traverse across the bifurcation point into the Hopf limit cycle regime, and traverse back towards the stable regime once more. In this way, an autocatalytic reaction can begin appearing dormant until the vivid clock reaction occurs in the relaxation-oscillation regime and depletes the necessary substrates to sustain a reaction at which point the reaction becomes dormant once more. While the dynamics of the 1-dimensional Brusselator has been thoroughly explored, future work could focus on higher-dimensional Brusselator systems such as the 2-dimensional model of reactants in a petri-dish. In addition, it would interesting to consider the dynamical interactions of two coupled Brusselators.

## References

- [1] Stephen Strogatz, *Nonlinear Dynamics and Chaos* . Addison-Wesley, Massachusetts, 1994.
- [2] [http://en.wikipedia.org/wiki/File:Bzr\\_fotos.jpg](http://en.wikipedia.org/wiki/File:Bzr_fotos.jpg)
- [3] Jeffrey Chasnov, *Scientific Computing*, class notes.